Journal of Catalysis 260 (2008) 37–64

Contents lists available at ScienceDirect

Journal of Catalysis

www.elsevier.com/locate/jcat

The chemistry of ethane dehydrogenation over a supported platinum catalyst

R.S. Vincent [a], R.P. Lindstedt [a,*], N.A. Malik [a], I.A.B. Reid [b], B.E. Messenger [b]

[a] Thermofluids Division, Department of Mechanical Engineering, Imperial College, Exhibition Road, London SW7 2AZ, UK
[b] Ineos Technologies Ltd, PO Box 21, Bo'ness Road, Grangemouth, Stirlingshire, FK3 9XH, UK

ARTICLE INFO

Article history:
Received 26 June 2008
Revised 27 August 2008
Accepted 28 August 2008
Available online 7 October 2008

Keywords:
Catalytic dehydrogenation
Ethylene
Platinum
SCTR

ABSTRACT

An investigation of the production of C_2H_4 through the selective dehydrogenation of C_2H_6 in short contact time reactors featuring a ceramic-foam catalyst coated with platinum is reported. The surface chemistry was derived on the basis of four reaction classes (direct adsorption, adsorption on an adsorbate, surface reactions with adsorbed reactants and unimolecular surface reactions including desorption) using collision theory with energy barriers obtained from DFT studies and the UBI–QEP method. The derived mechanism accounts for differences in site occupation and surface bonding types and includes 35 adsorbed chemical species and 283 reversible reactions. The study also features a comprehensively validated C_1–C_2 mechanism for the gas phase consisting of 44 chemical species and 271 reversible reactions. The complete chemistry was evaluated through extensive sensitivity analysis with reference to 16 sets of new experimental data. The reaction dynamics were studied using inlet velocities in the range 1.34 to 6.72 m/s and the impact on selectivities of variations in the oxygen to carbon weight ratio between 0.45 and 0.75 assessed. It is shown that the simulations capture all experimental trends with reasonable quantitative accuracy. The study suggests that the catalytic dehydrogenation of C_2H_6 initially contributes to the net production of C_2H_4 and that changing conditions in the gas phase adjacent to the catalyst can result in the consumption of ethylene principally leading to methane and carbon deposition. It is shown that the consumption of H_2 and O_2 proceeds predominantly through catalytic conversion under all conditions and that OH(s) provides a dominant channel for the removal of surface carbon. It is also shown that the consumption of oxygenated species features surface specific channels.

© 2008 Elsevier Inc. All rights reserved.

1. Introduction

Technologies based on the selective oxidation of ethane in short contact time reactors (SCTR) have the potential to substantially reduce the environmental impact, size and capital investment associated with the production of ethylene via steam cracking, e.g., [1–3]. Comprehensive laboratory experiments performed by Schmidt and co-workers [4–7] have shown that conversion of ethane in microchannel reactors coated with platinum can reach 70% with a selectivity to ethylene as high as 72% per pass at close to atmospheric pressure. The use of other catalysts (e.g., Pt/Sn) resulted in corresponding figures of 80% and 84%, respectively. The potential yields thus compare favorably with conventional steam crackers which commonly provide a selectivity of ≃75% at comparable per pass conversion levels at pressures around 1.8 atm. Huff and Schmidt [4] suggested that since the selectivity to ethylene was particularly high for this type of device, simple reaction pathways must dominate the mechanism. Hence, it was proposed that the process was initiated by oxidative dehydrogenation of adsorbed ethane followed by β-hydrogen elimination in order to yield ethylene from the surface. A difficulty with the proposed mechanism resided in the fact that most of the oxygen present in the system was consumed strongly from the very entrance of the reactor. A number of subsequent investigators [8–12] emphasized the role of ethylidyne. For example, Loaiza et al. [8] proposed that ethane is adsorbed dissociatively into ethyl, which dehydrogenates into di-σ ethylene followed by a transformation into ethylidyne and C–C bond scission, while De La Cruz and Sheppard [10] focused on ethane dehydrogenation into di-σ ethylene with the latter turning into ethylidyne. Other studies [13,14] proposed that the C–C bond scission takes place much earlier, either from the ethyl radical or from ethylene adsorbed on the surface [12,15], and uncertainties remain concerning the major channels. Pathways proceeding via a range of surface species including ethylene, adsorbed in the di-σ and π configurations, ethyl, ethylidene and vinyl groups have been recurrent species characterizing the mechanism. A range of alternative pathways have been suggested [9,16–18] and several investigators (e.g., Warnatz [19], Chatterjee et al. [20], Tischer et al. [21], Aghalayam et al. [22], Mahdeshwar and Vlachos [23,24] and Quiceno et al. [25]) have pursued detailed chemical kinetic modeling in order to elucidate reaction pathways for related systems. Zerkle et al. [26] integrated a range of different channels into a 82-step reac-

* Corresponding author. Fax: +44 207 589 3905.
E-mail address: p.lindstedt@imperial.ac.uk (R.P. Lindstedt).

0021-9517/$ – see front matter © 2008 Elsevier Inc. All rights reserved.
doi:10.1016/j.jcat.2008.08.014

Table 1
Experimental parameters: L_t (mm) total length before sampling point, oxygen to carbon (O/C) weight ratio, superficial inlet velocity U_{in} (m/s), inlet temperature T_{in} (K), wall temperature at the entrance of catalyst T_{in}^{w} (K) and the maximum adiabatic temperature T_{max} (K) used in heat loss calculations.

#	L_t	O/C	U_{in}	T_{in}	T_{in}^{w}	T_{max}	#	L_t	O/C	U_{in}	T_{in}	T_{in}^{w}	T_{max}
1	220	0.50	1.34	327	772	1289	7	310	0.45	2.10	420	844	1318
2	220	0.55	1.34	327	777	1295	8	310	0.50	2.10	418	867	1340
3	220	0.60	1.34	327	784	1301	9	310	0.55	2.10	421	890	1353
4	220	0.65	1.34	327	792	1307	10	310	0.60	2.10	423	909	1369
5	220	0.70	1.34	327	800	1314	11	310	0.65	2.10	423	936	1386
6	220	0.75	1.34	327	807	1319	12	310	0.70	2.10	424	981	1408
13	310	0.65	3.35	418	850	1338	14	310	0.65	4.18	408	806	1307
15	310	0.65	5.86	392	740	1263	16	310	0.65	6.72	383	681	1234

tion mechanism, specifically aimed at studying the reactions paths of C_2H_6 over platinum, and proposed that catalytic reactions were the main driver for triggering subsequent reactions by providing the necessary heat and that C_2H_4 formation proceeds on the surface as well as in the gas phase. Huff et al. [27] similarly suggested that the catalyst initiates the gas phase processes by heat release. Donsí et al. [28] used a simplified surface mechanism based on published kinetic data for H_2 and CO oxidation on platinum combined with lumped steps for ethane decomposition and reached a similar conclusion. By contrast, Beretta et al. [29] found no evidence of the catalytic production of ethylene.

In the present work, the multiple pathways discussed above have been included in a comprehensive reaction mechanism based on the mean-field approximation in order to assess their potential contributions to the dehydrogenation of ethane over a platinum catalyst. The gas phase chemistry was represented by a comprehensively validated detailed reaction mechanism featuring 44 chemical species and 271 reversible chemical reactions. The Unity Bond Index–Quadratic Exponential Potential (UBI–QEP) method [30–37] was combined with results from Density Functional Theory (DFT) studies (e.g., [24,38,39]) and kinetic collision theory (e.g., [19–21,26,40]) to provide the basis for the semi-automatic generation of two consistent heterogeneous reaction mechanisms, based on alternative sets of heats of adsorption, featuring 35 adsorbates and their interaction with the gas phase. The derived heterogeneous mechanisms were subsequently simplified through the application of sensitivity and path analysis. The current work does not seek to optimize individual reactions, but to assess the ability of a reaction class based method to reproduce experimental data. The final mechanisms feature 283 reversible reactions and contain significant extensions compared to previous work. These include more complete reaction paths for the dehydrogenation of ethane into ethylene and for the C–C bond scission of adsorbed vinyl groups. Further pathways, describing the dehydrogenation of ethylene, leading to the release of methane into the gas phase and carbon deposition on the surface, were also included. The mechanisms distinguish between π and di-σ bonded ethylene, can be extended to include additional multiple site configurations, and provide a wider range of H(s) and OH(s) assisted dehydrogenation reactions. There is significant depletion of oxygen close to the catalyst and the mechanisms also feature oxidation of deposited carbon by OH(s), produced from the oxidation of hydrogen on the surface and from steam that is present in high concentrations close to the catalytic surface. Pathways proceeding via oxygenates, such as COOH(s) and CHOH(s_2), are also shown to contribute. The present work extends past studies by (i) presenting a new data base featuring 16 experimental data sets obtained using a 30 mm long ceramic-foam catalyst coated with platinum, the inclusion of more comprehensive (ii) gas phase and (iii) catalytic chemistry, (iv) covering a wider dynamic range in terms of residence times, (v) accounting for multi-site occupation by species and (vi) the interaction of gas phase radicals with the surface and adsorbates over (vii) a comparatively wide range of oxygen to carbon (O/C) weight ratios. Finally, the work permits a more comprehensive assessment of the relative contributions of homogeneous and heterogeneous chemical processes.

2. Experimental methods

The conversion of C_2H_6 in mixtures with N_2, H_2 and O_2 was investigated at atmospheric pressure in a microscale cylindrical reactor chamber using a Pt catalyst supported on Al_2O_3. The catalyst was prepared from lithium aluminum silicate foam washcoated with α-alumina, impregnated with a tetrammine platinum(II) chloride solution and calcined in air at a temperature of 1473 K for 6 h. The platinum loading corresponds to 3 wt%.

The catalyst bed consisted of a 30 mm long catalytic section followed by an inert extension. The total length of the bed (L_t) up to the sampling point was either 220 or 310 mm depending on the configuration used. The catalytic section was insulated upstream and downstream by placing 30 mm long inert alumina foam heat shields ahead and after the catalyst. The overall rig was placed in a 16 mm internal diameter tubular quartz reactor located in an electrically heated furnace. In all experiments the foam contained 30 pores per linear inch (ppi) with a porosity (ϕ) of about 82%. The individual single-pore channels therefore featured an average diameter $\simeq$ 0.75 mm and a wall thickness of about 80 μm.

All the reactant streams were mass flow controlled with an accuracy of 2%. The hydrogen to oxygen volume ratio (H_2/O_2) was set to 2 and the oxygen to carbon weight ratio (O/C) of the feed was varied between 0.45 and 0.75. The premixed gas streams were first passed over the catalyst at a general flow rate of 14.2 standard liters per minute (slpm). The flow rate was later gradually increased up to 71 slpm. The corresponding superficial axial gas velocities were therefore in the range 1.35 to 6.72 m/s at 273 K. Due to the pre-heating process, the operating inlet temperature (T_{in}) of the gas at the entrance of the catalyst varied between 327 and 424 K. However, the temperature of the catalyst at the entrance (T_{in}^{w}) was generally above 800 K due to heat transfer in the catalyst support. The gas and catalyst temperatures were measured using type K thermocouples with a nominal accuracy of ±9 K. The accuracy achievable in practice was influenced by factors such as heat losses and spatial resolution and, accordingly, a computational sensitivity analysis of the impact of heat losses was also performed. The experimental conditions are further outlined in Table 1.

The exit gases were analyzed off-line by gas chromatography. The light ends (permanent gases, C_2 hydrocarbons and carbon dioxide) were analyzed with a Unicam 6110 chromatograph using a combination of packed Haysep N and 5A molecular sieve columns in a backflush, analysis and by-pass arrangement with a Thermal Conductivity Analyzer (TCD) for detection and helium carrier. The samples were also analyzed on a HP5890 chromatograph with a 50 m × 0.32 mm × 5 μm Al_2O_3/KCl column using a Flame Ionization Detector (FID) with helium as carrier gas. The TCD response was calibrated using an external gas mixture whereas the FID used relative response factors. The cross correlation between the two

instruments was performed through the methane peak. All experiments were performed using an internal standard of ≃10% N_2 by volume. In order to close the carbon balances to 99.5% (the remainder assumed to be undetected oxygenates) the analyses were scaled according to the N_2 concentration detected. Heat balances were checked for self consistency with overall heat losses estimated to be in the range 10 to 20% based on the assumption of chemical equilibrium for a selected set of product species.

Temperature controlled program desorption experiments (temperature 298–1273 K; accuracy ±3 K; ramp rate 0.33 K/s) were also performed by Ineos Technologies Ltd on fresh catalyst sintered at the lower temperature of 873 K. The obtained maximum molar uptake (M_p) of the catalyst was 480×10^{-9} mol/g of carbon monoxide, 280×10^{-9} mol/g of ethane and 210×10^{-9} mol/g of C_2H_4. The corresponding site density Γ was estimated using these values via

$$\Gamma = \frac{\rho_s M_p}{S_v}, \tag{1}$$

where ρ_s is the average density of the catalyst (3.2×10^6 g/m^3) and S_v is the external surface area per unit volume of solid. The external surface area of the foam was estimated by several methods. If the surface of the idealized pore is treated as a cylindrical channel then the geometric ratio is simply

$$S_v = \frac{2\phi}{r_1(1-\phi)}, \tag{2}$$

where r_1 is the internal radius of the pore and ϕ the porosity of the catalyst support. Alternatively, the cubic cell model developed by Giani et al. [41] suggests

$$S_v = \frac{\sqrt{3\pi\phi}}{r_1\sqrt{1-\phi}}. \tag{3}$$

Finally, the geometrical tetrakaidecahedra array model of a foam proposed by Fourie and Du Plessis [42] yields

$$S_v = \frac{3\sqrt{\phi}}{2r_1(1-\phi)}(3-b)(b-1), \tag{4}$$

where

$$b = 2 - 2\sin\left(\frac{\sin^{-1}(2\phi-1)}{3}\right).$$

The above approximations give $15{,}500 \leqslant S_v\ (\mathrm{m}^{-1}) \leqslant 24{,}300$ and, combined with Eq. (1), an average density of active platinum sites in a range $5 \times 10^{-5} \leqslant \Gamma\ (\mathrm{mol/m^2}) \leqslant 10 \times 10^{-5}$. The values do not account for the additional fraction of the catalytic surface lost due to sintering (η_D) at the higher temperature used in the current work. Monzón et al. [43] studied the sintering and re-dispersion kinetics of Pt/alumina catalysts and estimated $\eta_D \geqslant 0.85$ at high ($T \geqslant 900$ K) temperatures. Analysis of used catalysts suggests a significant variability and a potentially greater loss of activity. Computations were accordingly performed using $\eta_D = 0.88$ combined with the above limiting values for the site density as well as a mid-range value of 7.5×10^{-5} mol/m^2 in order to establish the sensitivity of predictions.

3. Computational methods

A main objective of the current work was to explore the gas phase and catalytic pathways responsible for the dehydrogenation of ethane and simplifying assumptions were introduced for the pore structure. The flow was hence modeled using an axisymmetric assumption for a virtual pore running through the reactor. Consistent with the above discussion, the pore featured a nominal 30 mm catalytic section followed by an inert extension with a length of either 190 or 280 mm to represent the distance to the experimental sampling point. The length of the catalytically active pore was increased by 25% from the nominal value to account for macro-tortuosity. The value chosen is located between the suggestions of 1.07 by Bhattacharya et al. [44] and 1.5 by Fourie and Du Plessis [42]. The effective axial inlet velocity entering the pore was treated as inversely proportional to the porosity.

The single channel was modeled by two-dimensional boundary layer equations with initial and boundary conditions obtained from experimental data. The following equations for the conservation of mass, momentum, species and energy were solved in a similarity transformed coordinate system [45]:

$$\frac{\partial(\rho u)}{\partial x} + \frac{1}{r}\frac{\partial(r\rho v)}{\partial r} = 0, \tag{5}$$

$$\rho u\frac{\partial Y_i}{\partial x} + \rho v\frac{\partial Y_i}{\partial r} = -\frac{1}{r}\frac{\partial(rJ_i)}{\partial r} + M_i R_i, \tag{6}$$

$$\rho u\frac{\partial u}{\partial x} + \rho v\frac{\partial u}{\partial r} = -\frac{\partial P}{\partial x} + \frac{1}{r}\frac{\partial}{\partial r}\left(r\mu\frac{\partial u}{\partial r}\right), \tag{7}$$

$$\rho u\frac{\partial h}{\partial x} + \rho v\frac{\partial h}{\partial r} = \frac{1}{r}\frac{\partial}{\partial r}\left(\frac{\lambda_g}{C_p}r\frac{\partial h}{\partial r}\right) + \frac{1}{r}\frac{\partial}{\partial r}\left[\sum_{i=1}^{N_g} h_i r\left(-J_i - \frac{\lambda_g}{C_p}\frac{\partial(Y_i)}{\partial r}\right)\right], \tag{8}$$

$$-J_i = \rho D_i\left(\frac{\partial Y_i}{\partial r} - Y_i\frac{1}{n}\frac{\partial n}{\partial r}\right) - \rho v_c Y_i. \tag{9}$$

The components of the velocity are denoted by u and v in the x axial and r radial directions, ρ is the density of the fluid, h is the enthalpy of the mixture, C_p is the specific heat capacity at constant pressure, μ is the viscosity, λ_g is the thermal conductivity, n is the inverse of the mean molecular weight and P is the pressure. The gas phase mass fractions are denoted by Y_i. The species are characterized by their respective enthalpy h_i, molar mass M_i, diffusion coefficients D_i, diffusive flux J_i and net rate of formation R_i. The term v_c is a correction velocity chosen so that the sum of all fluxes is zero at the cell interfaces [45]. The mass fluxes resulting from the surface activity were integrated via Eq. (10) valid at the surface boundary,

$$J_i + \rho Y_i v_s = \eta_e R_i M_i, \tag{10}$$

where v_s is the Stephan flow velocity and η_e is the effectiveness factor which accounts for micro-pore diffusion limitations. The temperature of the catalyst is typically above 1100 K and the current study used the value $\eta_e = 0.1$ suggested by Wanker et al. [46]. The average furnace temperature T_0 was measured at the entrance of the reactor. Taking into account both N_g gas-phase species and N_s surface species, the corresponding energy balance at the wall can be expressed as

$$\lambda_g \Delta T|_g - \sum_{i=1}^{N_g}(J_i + \rho Y_i v_s)h_i = \lambda_w \kappa_1 \Delta T|_w + \sum_{i=N_g+1}^{N_g+N_s} R_i M_i h_i, \tag{11}$$

with $\kappa_1 = 1$ if $\Delta T|_w \leqslant 0$ (e.g., $T_{\mathrm{in}}^w \geqslant T_{\mathrm{in}}$) and 0 otherwise and λ_w is the thermal conductivity of the wall which is assumed constant. Radiative heat losses were imposed according to

$$T = T_{\mathrm{ad}}\left(1 - \kappa_2\left(\frac{T_{\mathrm{ad}}}{T_{\max}}\right)^4\right), \tag{12}$$

where κ_2 is a heat loss parameter, $T_{\max}$ is the maximum adiabatic temperature, computed using the assumption of chemical equilibrium [47], and T_{ad} is the adiabatic temperature. The sensitivity of computed results to κ_2 was explored using values in the range 0 to 0.15 and with reference to measured temperatures. In Eq. (11),

the heat conducted from the external wall into the gas-phase inside the pore was modeled to account for the electrically heated furnace and the upstream conduction of heat generated by catalytic reactions. The experimentally measured temperature of the wall at the entrance of the catalytic section was always well above the inlet temperature of the gas. As discussed below, the overall thermal balancing of the reactor was further assessed with reference to temperature measurements at the entrance and exit of the catalytic bed as well as at the product sampling point.

The implementation of the surface chemistry is based on the methodology described by Coltrin et al. [48]. The catalytic metal-surface is an interface for molecular exchanges with the complete set of gas and surface phase species in the system is ordered as $\chi_1, \chi_2, \ldots, \chi_{N_g}, \xi_{N_g+1}, \xi_{N_g+2}, \ldots, \xi_{N_g+N_s}$. The complete mechanism is described by a collection of M_g elementary reversible gas-phase reactions and M_s elementary reversible heterogeneous reactions so that regardless of the phase, the molar production rate R_i for each of the $N_g + N_s$ species is written as

$$R_i = \sum_{m=1}^{M_g+M_s} \Xi_{mi} \left(k_m^f \prod_{n=1}^{N_g+N_s} [X_n]^{\nu_{nm}^f} - k_m^r \prod_{n=1}^{N_g+N_s} [X_n]^{\nu_{nm}^r} \right). \tag{13}$$

In the above equation, X_n stands for the adsorbate ξ_n or gas phase molecule χ_n. Equation (13) emphasizes explicitly the coupling between gas phase and surface phase since $[X_n]$ stands for both the gas phase volumetric molar concentrations of species χ_n expressed in moles per unit volume and for the surface molar concentrations of adsorbate ξ_n expressed in moles per unit area. The thermodynamic data for gas phase and surface species was evaluated using standard polynomials [48],

$$\frac{C_{p,i}}{R} = a_1 + a_2 T + a_3 T2 + a_4 T3 + a_5 T4, \tag{14}$$

$$\frac{H_i}{RT} = a_1 + \frac{a_2}{2} T + \frac{a_3}{3} T2 + \frac{a_4}{4} T3 + \frac{a_5}{5} T4 + \frac{a_6}{T}, \tag{15}$$

$$\frac{S_i}{RT} = a_1 \ln T + a_2 T + \frac{a_3}{2} T2 + \frac{a_4}{3} T3 + \frac{a_5}{4} T4 + a_7, \tag{16}$$

where $C_{p,i}$ is the specific heat for species i at constant pressure, H_i the enthalpy and S_i the corresponding entropy. For surface species the first five polynomial coefficients a_i remain unchanged and the sixth term $a_6(\xi_s)$ is adjusted as $a_6(\xi_s) = a_6(\chi_g) - \mathcal{Q}/R$, where $a_6(\chi_g)$ is the sixth coefficient for the standard heat of formation of the matching gas phase molecule χ_g.

4. The gas phase chemistry

A detailed mechanism that includes low-temperature chemistry was adopted to model chemical reactions in the gas phase. The mechanism stems from the work of Leung and Lindstedt [45], Juchmann et al. [49], Lindstedt and Skevis [50], Lindstedt and Meyer [51], Rizos [52] and Sun et al. [53] and consists of 271 reversible chemical reactions and 44 species: H, O, OH, HO_2, H_2O_2, H_2, O_2, H_2O, CO, CO_2, CH_4, CH_3, CH_3OO, CH_3OOH, CH_3OH, CH_3O, CH_2OH, CH_2O, CHO, $^1CH_2$, $^3CH_2$, CH, C_1, C_2H_6, C_2H_5, C_2H_5OO, C_2H_5OOH, CH_3CHO, CH_2CHO, CH_3CO, C_2H_4, C_2H_4OOH, C_2H_5O, CH_2CHO, C_2H_4O, C_2H_3, C_2H_2, H_2C_2, CH_2CO, HCCO, C_2O, C_2H, C_2 and N_2. The mechanism is included as supplementary material in a fully referenced form along with thermodynamic data, third-body collision efficiencies and pressure fall-off dependencies. The mechanism has been validated against experimental results covering a broad range of conditions such as CH_4 spontaneous ignition by Naylor and Wheeler [54] and Reid et al. [55], CH_4 and C_2H_6 ignition delay times by Burcat et al. [56], C_2H_6 and C_2H_4 oxidation in a jet-stirred reactor by Dagaut et al. [57,58], Marinov and Malte [59] and Homer and Kistiakowsky [60].

5. The surface chemistry

The complete set of N_s adsorbates and corresponding surface coverages Z_i, defined as the fraction of Pt sites occupied by the species ξ_i, takes into account the number of equivalent Pt atoms (σ_i) occupied by ξ_i.

5.1. Reaction class based estimation of rate constants

There is general agreement that systems of the current kind can essentially be described by (i) gas phase, (ii) adsorption–desorption and (iii) surface reactions. Rate parameters based on Langmuir–Hinshelwood reactions with frequency factors of $\sim 10^{11}$ for mobile surface species without rotation and/or $\sim 10^{13}$ s^{-1} for immobile surface species without rotation [40], have been used as starting points for mechanism construction prior to optimization of selected rate constants to provide a better fit with data derived from other sources (e.g., experiments or quantum mechanical methods). This strategy has been adopted by Zerkle et al. [26], Fridell et al. [61] and Aghalayam et al. [22,62]. For example, the latter studies used the assumption of Langmuir–Hinshelwood reactions with mobile surface species as a starting point and some of the pre-exponential factors were subsequently modified via an optimization process in order to reproduce experimental data. Zerkle et al. [26] adopted a similar approach, but assumed as a starting point frequency factors $\sim 10^{13}$ consistent with Langmuir–Hinshelwood reactions with immobile surface species and surface diffusion approximations. Nilekar et al. [63] performed periodic self-consistent DFT calculations for a limited set of species and found values for the pre-exponential term for diffusion on Pt(111) in a narrow range 3.9×10^{12} to 5.2×10^{12}. It was further suggested that practically no compensation effect exists between the pre-exponential factor and the activation energy barrier for diffusion of adsorbed species on transition metals.

The current work does not seek to optimize individual reactions in order to improve agreement with experimental data, but rather provides an assessment of the ability of a reaction class based method, outlined below, to represent heterogeneous processes. The approach has the merit that disagreement with experimental data can be explored in the context of alternative sets of basic parameters (e.g., heats of adsorption, see Table 2), missing reaction pathways and associated groups of reactions. The method of Warnatz and co-workers [19–21,26] has been used to provide an estimate of the scaling of pre-exponential factors. The approach is based on determining the relative velocity of mobile species on the surface, collision frequencies of molecules with the surface [40,64] along with the assignment of sticking and trapping probabilities.

5.1.1. Reaction class I: Direct adsorption

The direct adsorption of a gas phase molecule A_g onto the catalyst is written as $A_g + x\mathrm{Pt}(s) \rightarrow P_s$, where x is the number of platinum atoms required for the adsorption. The reaction may be dissociative or non-dissociative. Assuming a uniform distribution of platinum and taking into account the total catalytic area, the reaction rate can be expressed as

$$\mathcal{R}_m^a = k_m^a [A_g] Z_S^x, \tag{17}$$

where

$$k_m^a = \frac{\alpha}{x^x} A(\mathrm{Pt}) \mathcal{N}_A \Gamma \sqrt{\frac{RT}{2\pi M_{A_g}}} \exp\left(-\frac{\Delta E_{a,m}}{RT} \right) \tag{18}$$

and $A(\mathrm{Pt})$ is the projected platinum area while α represents the probability of a molecule being trapped and adsorbed on the surface. The temperature dependency of the rate constant is thus

Table 2
Heat of adsorption ($\mathcal{Q}$) of species on a platinum surface.

Adsorbate	Mode	Current values	[32]	[34]	Computations	Experiments	E_{ξ_s}
H(s)[c]	H	**255**	255	255	267 [131], 281 [39]	255 [71]	–
O(s)[c]	O	**356**	356	356	311 [39], 316 [123]	356 [71]	–
H_2(s)[a]	H–H	**26.8**	26.8	26.8	–	41–75 [40]	431.24
$O_2(s_2)$[b]	O–O	**44.3**	44.3	–	–	37.7 [78]	498.23
OH(s)[a]	O	**247**[f]	247	–	171 [39], 250 [125]	251 [79,80]	427.05
OOH(s)[a]	O	**204**	203	–	–	–	706.75
H_2O(s)[a]	O	**40.2**	40.2	–	32.7 [125], 66.9 [39]	40.2 [84]	921.09
$H_2O_2(s_2)$[b]	O–O	**27.1**	56.5	–	–	–	1070.56
$C(s_3)$[c]	C	**628**	627	627	659 [126], 636 [73]	627 [71]	–
$CH(s_3)$[c]	C	**407**	407	407	657 [126], 697 [73]	–	339.13
$CH_2(s_2)$[b]	C	**283**	283	283	384 [126], 436 [73]	–	761.99
CH_3(s)[a]	C	**159**	159	159	186 [127], 225 [73]	–	1226.73
CH_4	C	**25.1**[h]	–	25.5	–	–	1666.34
CCH(s)[c]	C	**287**	–	153	395 [73]	–	1084.38
$CCH_2(s_2)$[b]	C	**299**	–	–	160 [38]	–	1457.01
$CCH_2(s_3)$[d]	C–C	110[d] or **149**[e,d]	–	154	232 [38]	–	1457.01
$CCH_3(s_3)$[c]	C	**405**	–	356	653 [73]	–	1569.29
$CHCH_2$(s)	C	**184**	–	–	–	–	1786.86
$CHCH_2(s_3)$[b]	C–C	89.1 or **129**[e,d]	–	139	395.7 [73]	–	1786.86
$CHCH_3(s_2)$[b]	C	**294**	–	292	410 [73]	–	1934.46
CH_2CH_3(s)[a]	C	**163**	42.6	163	189 [73]	–	2411.60
$C_2H_2(s_3)$[d]	C–C	95 or **134**[e]	–	65.7	219 [38], 309 [73]	–	1641.23
C_2H_4(s)[a]	C–C	29.3 or **68**[e]	–		35.5 [73], 68 [38]	29.3, 92 [70,86,87]	2252.50
$C_2H_4(s_2)$[b]	C–C	46.1[b] or **99**[e]	48.9	46	99 [38], 151 [73]	41.8, 171 [85,86]	2252.50
$C_2H_6(s_2)$[b]	C–C	**36.1**	17.2	31.8	–	–	2821.90
$CO(s_2)$[b]	C	**134**[g]	134	–	171 [128], 174 [73]	145 [83]	1076.0
$CO_2(s_2)$[a]	O–O	**15.1**	15.1	–	0 [39], 19.2 [129]	–	1607.73
CHO(s)[a]	C	**167**	167	–	227 [127], 262 [39]	–	1147.18
$COH(s_3)$[c]	C	**337**	–	–	293 [39], 429 [127]	–	965.54
$CHOH(s_2)$[b]	C	**200**	–	–	312 [127], 365 [39]	–	1300.41
COOH(s)[a]	C	**213**	–	–	226 [130], 265.5 [39]	–	1646.03
$CH_2O(s)$[b]	O	**46.7**	47.7	–	40.2 [39], 48.2 [127]	–	1511.43
CH_2OH(s)[a]	C	**160**	159	–	209 [131], 274 [39]	–	1637.0
CH_3OH(s)[a]	O	**44.1**	43.9	–	43 [131], 62.5 [39]	47.7 [84]	2038.97
CH_3O(s)[a]	O	**173**	173	–	105 [39], 148 [127]	–	1603.54

Note. Energies are in kJ/mol. E_{ξ_s} is the total gas-phase bond energy [91]. The indices s_{σ_i} indicate the number of platinum atoms involved in the adsorption of the compounds. The values retained in the surface mechanism shown in Appendix A are displayed in bold font. The alternative values also listed were used in the generation of the UBI–QEP based mechanism.

[a] Adsorbed in on-top site.
[b] Adsorbed in a bridged site.
[c] Adsorbed on hollow fcc site.
[d] Adsorbed via a bridge + π-bond.
[e] Alternative value used in sensitivity analysis.
[f] Adjusted from 162 with experimental values [79–81].
[g] Adjusted from experimental between 113 and 145 [83].
[h] Adjusted from 69 with experimental values [81,82].

described using a standard modified Arrhenius expression. Sticking and trapping probabilities are often conjectural. A straightforward approach is to use the sticking probability s_0 on a clean surface fully covered with polycrystalline Pt(111) in the zero coverage limit. Introduction of $x = 1$ and $s_0 = \alpha \Gamma_{\mathrm{Pt}} A(\mathrm{Pt}) \mathcal{N}_A$ ($\simeq \alpha$) leads to the formula proposed by Zerkle et al. [26] and Chatterjee et al. [20],

$$k^a_{m,0} = s_0 \sqrt{\frac{RT}{2\pi M_{A_g}}} \exp\left(-\frac{\Delta E_{a,m}}{RT}\right). \tag{19}$$

The above expression is valid for a characteristic Γ_{Pt} ($\simeq 2.72 \times 10^{-5}$ mol/m^2) and a 1:1 ratio between geometrical and physical area. In general, the actual value of Γ will depend on the preparation of the catalyst (e.g., loading and micro-porosity) and accordingly,

$$k^a_m = \frac{s_0}{x^x} \frac{\Gamma}{\Gamma_{\mathrm{Pt}}} \sqrt{\frac{RT}{2\pi M_{A_g}}} \exp\left(-\frac{\Delta E_{a,m}}{RT}\right). \tag{20}$$

The sticking coefficients s_0 used in Eq. (20) were assumed to be unity for radical species with values for stable molecules based on the studies by Aghalayam et al. [22], Mahdeshwar and Vlachos [24], Zerkle et al. [26] and Panja et al. [65] as listed in Table 3.

5.1.2. Reaction class II: Adsorption on an adsorbate

A reaction class that is not commonly considered features the reaction of a gas phase atom or molecule with an adsorbate $A_g + B_s + x\mathrm{Pt}(s) \rightarrow P_s$. The van der Waals radius (see Table 3) defines a volume-sphere for the adsorbate B_s. The projected area $A(B_s)$ accounts for collisions and $A(B_s)\mathcal{N}_A[B_s]$ is the total projected area occupied by B_s per unit of surface. The reaction probability is here considered equal to s_0, which represents an upper limit, and the following form is obtained,

$$\mathcal{R}^b_m = k^b_m [A_g] Z_{B_s} Z^x_S, \tag{21}$$

where

$$k^b_m = \frac{s_0}{x^x \sigma_{B_s}} A(B_s) \mathcal{N}_A \Gamma \sqrt{\frac{RT}{2\pi M_{A_g}}} \exp\left(-\frac{E_{a,m}}{RT}\right). \tag{22}$$

Quiceno et al. [25] explored a similar scaling for a few related steps and the reaction class has been included in order to assess the potential importance under the current conditions.

5.1.3. Reaction class III: Surface reactions with adsorbed reactants

Surface reactions involving only adsorbed reactants are expressed as $A_s + B_s + x\mathrm{Pt}(s) \rightarrow P_s + P_g$, where the two adsorbates react and produce new species that remain on the surface or are released into the gas phase. The qualitative scaling of the pre-exponential factor was derived using the two-dimensional average relative velocity of mobile species on the surface[1] (e.g., Warnatz [19], Ljungström et al. [66] and Dumesic et al. [40]) which leads to

$$\mathcal{R}_m^s = k_m^s Z_{A_s} Z_{B_s} Z_S^x, \tag{23}$$

where

$$k_m^s = \frac{D_{AB}^d \mathcal{N}_A \Gamma^2}{x^x \sigma_{A_s} \sigma_{B_s}} \sqrt{\frac{\pi RT}{2M_R}} \exp\left(-\frac{\Delta E_{a,m}}{RT}\right) \quad \text{and}$$

$$M_R = \frac{M_{A_s} M_{B_s}}{M_{A_s} + M_{B_s}}. \tag{24}$$

In the above expression, D_{AB}^d is the sum of the molecular diameters of surface species A_s and B_s—here estimated using their respective van der Waals radii—and M_{A_s} and M_{B_s} their respective molecular weights (see Table 3). The above expression arguably provides upper limit pre-exponential factors for the probability of reaction. For the current set of reactions values in the range 3×10^{12} to 3×10^{13} were obtained at 1050 K and a uniform scaling factor of 0.3 was used to provide improved consistency with the range 3.9×10^{12} to 5.2×10^{12} proposed by Nilekar et al. [63] for a smaller set of species.

5.1.4. Reaction class IV: Unimolecular surface reactions

The final case of unimolecular reactions $A_s + x\mathrm{Pt}(s) \rightarrow P_s + P_g$ cannot be handled directly using collision theory. However, two sub-cases can readily be identified. If $x \geqslant 1$, the reaction can be written as $A_s + \mathrm{Pt}(s) + (x-1)\mathrm{Pt}(s) \rightarrow P_s + P_g$. By analogy with Eq. (23), the rate may be expressed as

$$\mathcal{R}_m^u = k_m^u Z_{A_s} Z_S^x, \tag{25}$$

where

$$k_m^u = \frac{D_{APt}^d \mathcal{N}_A \Gamma^2}{x^x \sigma_{A_s}} \sqrt{\frac{\pi RT}{2M_{A_s}}} \exp\left(-\frac{\Delta E_{a,m}}{RT}\right). \tag{26}$$

In order to be consistent, the rate constants resulting from Eq. (25) have been scaled in the same manner as discussed for Eq. (23). If $x = 0$, then the assumption of the same degree of mobility and freedom between the reactant and the product in its transition state [67–69] gives as a first approximation

$$\mathcal{R}_m^d = k_m^d Z_{A_s}, \tag{27}$$

where

$$k_m^d = \frac{\Gamma}{\sigma_{A_s}} \frac{RT}{\mathcal{N}_A h_p} \exp\left(-\frac{\Delta E_{a,m}}{RT}\right) \tag{28}$$

and h_p is Planck's constant. Unimolecular reactions generally concern desorption reactions, molecular dissociation and isomerization. The resulting pre-exponential terms are of order 10^{13} s^{-1} at 1050 K. However, if the activated complex is adsorbed more weakly than the reactant species, it has been suggested that the pre-exponential term can reach values of 2.5×10^{17} s^{-1} [40]. Consequently, in some cases there are significant uncertainties in estimating the pre-exponential term for the desorption rate.

[1] Energy barriers for diffusion of species on the surface are treated as part of the UBI–QEP formalism outlined below.

5.2. Energetics of surface reactions

The energy barriers for the surface reactions were determined using data from experimental (e.g., [70]) and DFT studies (e.g., [38]) as well as through the UBI–QEP method (e.g., [30–37]). The latter method provides the current base case. The structural configuration of the adsorbate, the number of metal-atoms (coordination) and the atoms within the molecule involved in the process of adsorption (mode) are required and input parameters are shown in Table 2.

5.2.1. Enthalpies of adsorption and heats of reactions

A variational method was combined with the UBI–QEP formalism in order to calculate the corresponding heats of adsorption ($\mathcal{Q}$) with each adsorbate further characterized via the number of platinum atoms (n) involved in the calculation of the heats of adsorption. The configurations selected for the different adsorbates follow suggestions from computational [14,73–75] and experimental [12,76] studies. The heats of adsorption of H(s) and O(s) were both estimated in the hollow cap configuration ($n = 3$).[2] However, given their respective atomic size and free electron valence only one equivalent platinum atom was assumed to be necessary to compute surface coverages. The UBI–QEP method has been used extensively to estimate heats of adsorption for a range of related systems and the treatment of the 35 current adsorbates is reported below for reasons of completeness. Weakly bonded (e.g., closed electronic shells) molecules $H_2O(s)$, $CH_2O(s)$ and $CH_3OH(s)$ are treated according to

$$\mathcal{Q}_{AB} = \frac{Q_{A0}^2}{Q_{A0}/n + E_{AB}}, \tag{29}$$

where Q_{A0} is the atomic heat of adsorption and E_{AB} is the bond energy required to dissociate the functional groups A and B using the corresponding energies of the gas phase species given in Table 2 (e.g., [71]). Radicals such as OH(s), OOH(s), $C(s_3)$, $CH(s_3)$, $CH_2(s_2)$, CCH(s), $CCH_2(s_2)$, $CCH_3(s_3)$, $CHCH_3(s_2)$, $CH_3O(s)$, $COH(s_3)$, $CHOH(s_2)$ and COOH(s) will attach strongly to the surface and are treated according to

$$\mathcal{Q}_{AB} = \frac{\mathcal{Q}_A^2}{\mathcal{Q}_A + E_{AB}}, \tag{30}$$

where $\mathcal{Q}_A$ the heat of adsorption of the adsorbates (atoms or molecules). The medium bond strength (e.g., monovalent radicals having tetravalent contact atoms) $CH_3(s)$, $CHCH_2(s)$, $CH_2CH_3(s)$, CHO(s) and $CH_2OH(s)$ are treated via interpolation:

$$\mathcal{Q}_{AB} = \frac{1}{2}\left(\frac{Q_{A0}^2}{Q_{A0}/n + E_{AB}} + \frac{\mathcal{Q}_A^2}{\mathcal{Q}_A + E_{AB}}\right). \tag{31}$$

The contributions made by π-bonds (e.g., $C_2H_4(s)$) have been estimated from experimental and DFT studies. For di-coordinated diatomic molecules (e.g., $H_2(s)$ and $O_2(s_2)$) that attach to the surface across a bridge site via both atoms A and B the heat of adsorption is evaluated from

$$\mathcal{Q}_{AB} = \frac{ab(a+b) + E_{AB}(a-b)^2}{ab + E_{AB}(a+b)},$$
$$a = Q_{A0}^2 \frac{Q_{A0} + 2Q_{B0}}{(Q_{A0} + Q_{B0})^2}, \quad b = Q_{B0}^2 \frac{Q_{B0} + 2Q_{A0}}{(Q_{B0} + Q_{A0})^2}. \tag{32}$$

Due to the proximity of the carbon atom to the surface, carbon dioxide is treated as a linear molecule in a bridge configuration

[2] The $\mathrm{Pt}_n - |A$ bond energy $\mathcal{Q}_n$ of atomic species increases with the value of n, $\mathcal{Q}_A(n) = Q_0(2 - 1/n)$, where Q_0 is the atomic heat of adsorption of the atom located on top of a Pt atom ($Q_{0H} = 153$ kJ/mol, $Q_{0O} = 213$ kJ/mol and $Q_{0C} = 376$ kJ/mol).

[71]. Polyatomic molecules with a structure X_m–A–B–$Y_{m'}$ (e.g., $H_2O_2(s_2)$, $C_2H_6(s_2)$, $C_2H_4(s_2)$, $C_2H_2(s_3)$) are treated assuming that the molecule is attached to the surface via A and B. The latter may also feature m and m' atoms or groups X and Y. The heat of adsorption is written using the same form as in Eq. (32) with

$$a = Q_{A0}\left(1 - \left(\frac{mQ_{X0}}{mQ_{A0} + Q_{X0}}\right)^2\right),$$

$$b = Q_{B0}\left(1 - \left(\frac{m'Q_{Y0}}{m'Q_{B0} + Q_{Y0}}\right)^2\right),$$

and with E_{AB} replaced by the total gas phase bond energy E given directly in Table 2. The heat of adsorption of $CO(s_2)$ was adjusted using the experimental values suggested by Campbell et al. [83]. Differences with other studies using a similar approach arise, for example, due to bond partitioning.

5.2.2. Comments on heats of adsorption

The current estimations are calculated in the low coverage limit, but provide relatively good agreement with directly related theoretical studies [32,34,72,77] and available experimental data [78–80,83–86]. However, estimated values for the enthalpy of adsorption of ethylene vary considerably between different studies. Experimental values for π-bonded ethylene range between 29.3 ± 8.4 kJ/mol [87] and 92 kJ/mol [70], whereas estimates for the di-σ form vary between 41.8 kJ/mol [86], 54.4 ± 16.7 kJ/mol [87] up to a calculated value of 171 kJ/mol [75]. The results are dependent upon surface coverages and, in the case of theoretical studies, also influenced by factors such as the prescribed surface model. Thus, while it is difficult to directly compare results from different investigations, theoretical studies do provide additional information. Kua and Goddard [73], using an interstitial electron surface model and nonlocal density functional methods, proposed a strong di-σ bond (150 kJ/mol) and a π configuration adsorbed much more weakly (35.5 kJ/mol). Sautet and Paul [88] used extended Hückel calculations to show that the computed energy of adsorption of di-σ bonded ethylene would start converging only with a 49-atom platinum cluster. The binding energy would decrease from a value of 83 kJ/mol with a 15-atom cluster down to 63 kJ/mol with a 49-atom cluster and to 61.1 kJ/mol with a 114-atom cluster. The energy for π bonded ethylene was estimated at 33 kJ/mol. However, Podkolzin et al. [38] suggested, on the basis of DFT calculations, that the energy of the π-bond is significantly larger (68 kJ/mol), with the di-σ bonded form requiring 99 kJ/mol to adsorb on a bridge site. Collision-Induced Desorption (CID) on a platinum surface [89] and calorimetric measurements for Pt powder [76] under conditions where predominantly di-σ bonded species are formed, have yielded values of 124 and 120 kJ/mol, respectively. The adsorption enthalpy of π-bonded species was reported to be 40 ± 10 kJ/mol based on Reflection Adsorption Infrared Spectroscopy (RAIS) [86] and 92 kJ/mol based on CID with oxygen precovered Pt(111) [70]. Watwe and co-workers [75] performed a cluster study using the B3LYP exchange correlation functional with a 10-atoms cluster and estimated energies of 171 and 103 kJ/mol for the di-σ and π modes at 298 K. Subsequent calculations [90] using a 19-atom cluster provided adsorption energies of 116 and 71 kJ/mol for the same species. Despite the uncertainties, there is consistent evidence of significant differences in enthalpy of adsorption of the π and di-σ bonded configurations. Accordingly, reaction pathways on the surface can be expected to be strongly influenced by isomeric effects and the current study includes both configurations. Given the wide range of determinations, two complete reaction mechanisms were generated in order to explore the sensitivity of predictions to alternative sets of heats of adsorption shown in Table 2. The first mechanism was based on the lower limit UBI–QEP value of 46 kJ/mol for di-σ C_2H_4 combined with the experimental value of 29.3 kJ/mol [87] for the π bonded form. The latter value was chosen to maintain a significant difference in the heats of adsorption between the two structures. The values chosen as the basis for the generation of an alternative hybrid mechanism, using a combination of UBI–QEP and DFT data, correspond to 68 and 99 kJ/mol suggested by Podkolzin et al. [38].

5.2.3. Energy barriers for forward and reverse reactions

The enthalpies ΔH_s and energy barriers $\Delta E_{a,m}$ used in the generation of the heterogeneous reaction mechanisms are outlined below. The direct adsorption (or non-dissociative adsorption) of a gas phase species A_g onto the surface does not have an energy barrier.

$$\Delta H_s = \mathcal{Q}_A \quad \text{and} \quad \Delta E_{a,m} = 0. \tag{33}$$

The direct desorption (or non-recombinative desorption) of a gas phase species from the surface is the reverse of a direct adsorption,

$$\Delta H_s = -\mathcal{Q}_A \quad \text{and} \quad \Delta E_{a,m} = \mathcal{Q}_A. \tag{34}$$

Homogeneous surface phase reactions where all reactants and products are located on the surface can be written as $\xi_{1s} + \xi_{2s} \rightarrow \xi_{3s} + \xi_{4s}$ with ΔH_s^f and ΔH_s^r the corresponding forward and reverse enthalpies of reaction, ΔE_s^f and ΔE_s^r the activation energies and $E_{\xi_{is}}$ the total bond energy of the surface species ξ_{is}. The latter was directly estimated from the bond dissociation energies and heats of formation of their respective gas phase counterparts [91]. Two cases are considered. If $E_{\xi_{1s}} + E_{\xi_{2s}} \geqslant E_{\xi_{3s}} + E_{\xi_{4s}}$ then

$$\Delta H_s^f = E_{\xi_{1s}} + E_{\xi_{2s}} - E_{\xi_{3s}} - E_{\xi_{4s}} + Q_{\xi_{1s}} + Q_{\xi_{2s}} - Q_{\xi_{3s}} - Q_{\xi_{4s}}, \tag{35}$$

$$\Delta E_s^f = \frac{1}{2}\left(\Delta H_{fs} + \frac{Q_{\xi_{3s}} Q_{\xi_{4s}}}{Q_{\xi_{3s}} + Q_{\xi_{4s}}}\right), \tag{36}$$

$$\Delta E_s^r = \Delta E_s^f - \Delta H_s^f. \tag{37}$$

If $E_{\xi_{1s}} + E_{\xi_{2s}} < E_{\xi_{3s}} + E_{\xi_{4s}}$ then the reverse reaction $\xi_{3s} + \xi_{4s} \rightarrow \xi_{1s} + \xi_{2s}$ is considered and the above equations are modified accordingly. The multiplier in Eq. (36) accounts for the fact that the energy barriers provided by the UBI–QEP method tend to overestimate the true activation energies and hence an interpolation is made (e.g., [71]). However, for a few triatomic linear molecules, such as O–C–O, a strongly distorted intermediate state has been predicted and observed [81]. Such distortion would imply strong expansion and weak attachment of the C–O bonds. Recent DFT simulations by Michaelides et al. [92] suggest that the activation energies for dissociation are typically linearly proportional to the heat of reaction with a slope of 0.86 which indicates a transition state closer to the products. Mhadeshwar and Vlachos [24,93] accordingly changed the bond indices to 0.8 and 0.7 for the CO–O and the C–O reactions. A value of 1.0 has been used here for the oxidation of $CO(s_2)$ to $CO_2(s_2)$ by O(s) and OH(s). The experimental activation energy for the reaction of CO and O has been reported to be around 100–109 kJ/mol in the low coverage regime on Pt [94] and on polycrystalline Pt [95], which compares reasonably well with the current value of 97 kJ/mol.

Heterogeneous surface-phase reactions correspond to cases where there is at least one gas phase product or reactant $X_{1\alpha} + X_{2\beta} \rightarrow X_{3\gamma} + X_{4\iota}$ where the subscripts $\alpha, \beta, \gamma, \iota$ are replaced by s or g depending on the phase of each compound X_i. In order to calculate ΔE_g^f, ΔE_g^r, ΔH_g^f and ΔH_g^r, the energetics of the corresponding forward and reverse reactions are considered. If $E_{X_{1\alpha}} + E_{X_{2\beta}} \geqslant E_{X_{3\gamma}} + E_{X_{4\iota}}$ then

$$\Delta H_g^f = \Delta H_s^f - \delta_{\alpha g} Q_{X_{1\alpha}} - \delta_{\beta g} Q_{X_{2\beta}} + \delta_{\gamma g} Q_{X_{3\gamma}} + \delta_{\iota g} Q_{X_{4\iota}}, \tag{38}$$

$$\Delta E_g^f = \Delta E_s^f - \delta_{\alpha g} Q_{X_{1\alpha}} - \delta_{\beta g} Q_{X_{2\beta}},$$

$$\Delta E_g^r = \Delta E_g^f - \Delta H_g^f. \tag{39}$$

Table 3
Sticking coefficients and molecular properties.

Adsorbate	S_0	VDW	M	Adsorbate	S_0	VDW	M
H(s)	1	1.17	1.008	O(s)	1	1.40	15.999
H_2(s)	0.046 [26]	1.32	2.016	O_2(s_2)	$0.05 \times (300/T)$ [26,122]	1.65	31.998
OH(s)	1	1.52	17.007	OOH(s)	1	1.80	33.077
H_2O(s)	0.75 [26]	1.64	18.015	H_2O_2(s_2)	0.75	1.88	34.156
C(s_3)	1	1.75	12.01	CH(s_3)	1	1.79	13.089
CH_2(s_2)	1	1.85	14.168	CH_3(s)	1	1.88	15.247
CH_4	0.2 [22,24]	1.94	16.32	CCH(s)	1	2.06	25.099
CCH_2(s_2)	1	2.13	26.178	CCH_2(s_3)	1	2.13	26.178
CCH_3(s_3)	1	2.19	27.257	$CHCH_2$(s)	1	2.16	27.257
$CHCH_2$(s_3)	1	2.23	27.257	$CHCH_3$(s_2)	1	2.23	28.336
CH_2CH_3(s)	1	2.25	29.415	C_2H_2(s_3)	0.05 [26]	2.09	26.178
C_2H_4(s)	0.015 [26]	2.19	28.336	C_2H_4(s_2)	0.015 [26]	2.18	28.336
C_2H_6(s_2)	0.015 [26]	2.32	30.49	CO(s_2)	0.84 [26]	1.88	28.009
CO_2(s_2)	0.005 [26]	1.95	44.008	CHO(s)	1	1.92	29.088
COH(s_3)	1	1.92	29.088	CHOH(s_2)	1	1.95	30.187
COOH(s)	1	2.02	45.01	CH_2O(s)	0.1 [24]	1.99	30.167
CH_2OH(s)	1	2.06	31.246	CH_3OH(s)	0.3 [24]	2.12	32.325
CH_3O(s)	1	2.04	31.246				

Note. VDW is the radius of the projected van der Waals surface for the compound A in Ångström, M is its molecular weight in g/mol. The indices in the symbols s_x characterize the coordination number (number of platinum atoms) involved in the adsorption of the compounds.

If $E_{X_{1\alpha}} + E_{X_{2\beta}} < E_{X_{3\gamma}} + E_{X_{4\iota}}$ then the reverse reaction is considered and Eqs. (38) and (39) are modified accordingly. In the above expressions, δ is the Kronecker symbol such that $\delta_{ab} = 1$ if $a = b$ and 0 otherwise. Dissociative adsorption of a species AB into two adsorbates A and B on the surface is treated with $X_{2\beta} = 0$, $\alpha = g$ and $\gamma = \iota = s$. Recombinative desorption of two adsorbates into one gas-phase species are treated as $X_{4\iota} = 0$, $\alpha = \beta = s$ and $\gamma = g$.

5.2.4. Isomerization reactions

The UBI–QEP method does not determine activation barriers for isomerization reactions and there are few quantitative studies featuring platinum surfaces. Zaera et al. [9,96] suggested that the shift from the π-bonded configuration to the di-σ adsorbate on Pt(111) has no barrier and that the reverse reaction has to overcome a 20 kJ/mol activation energy. The corresponding value using the current heats of adsorption is 31 kJ/mol and other isomerization reactions featuring a platinum bond rearrangement were also treated based on differences in the heat of adsorption. The same applies to adsorption reactions where the heat of adsorption is greater than the energy barrier required for a hydrogen shift. Zaera et al. [9,96] also proposed forward and reverse barriers of 60 and 30 kJ/mol for the hydrogen shift leading from di-σ ethylene to ethylidene. Zerkle et al. [26] and Wolf et al. [97] proposed forward barriers of 83 and 87 kJ/mol for the hydrogen shift from π and di-σ ethylene leading to ethylidene, with reverse activation barriers of 75 and 50 kJ/mol, respectively. Barriers of 129 and 176 kJ/mol for the forward and reverse reactions associated with the hydrogen-shift from the vinyl radical to ethylidyne were also suggested. Anghel et al. [98] proposed that isomerization reactions are not surface mediated and suggested a forward barrier for the transformation of ethylene to ethylidene of 222.5 kJ/mol with a reverse barrier of 196.5 kJ/mol. The sensitivity to energy barriers was tentatively assessed as part of the current work using data derived from the corresponding gas phase reactions. The required hydrogen transfer reactions were calculated using Gaussian 03 [99] at the G3B3 [100] level. Stationary points, characterized as either minima or first order saddle points, were located on each potential energy surface using B3LYP [101] density functional theory and the 6-31g(d) basis set. Intrinsic reaction coordinate (IRC) calculations were performed in order to follow the reaction path in both directions from the transition states to confirm linkage to the relevant minima. Further G3B3 composite calculations were then preformed on each stationary point to provide more accurate energies shown in Table 4. The barriers were then translated based either on the heat of reaction on the surface or via an alternative method based on the assumption that the transition state is related to the more stable compound and that the heat of adsorption varies monotonically between the reactant and the product. For a surface reaction $\xi_{1s} \rightarrow \xi_{2s}$ where $Q_{X_1} < Q_{X_2}$ the heat of adsorption of the transition state was estimated from

$$Q_{\mathrm{TST}} = Q_{X_1} + \frac{Q_{X_2}(Q_{X_2} - Q_{X_1})}{Q_{X_2} + Q_{X_1}}, \tag{40}$$

resulting in the following forward and reverse energy barriers for the corresponding surface reaction,

$$\Delta E^f_{si} = \Delta E^f_{gi} - Q_{\mathrm{TST}} + Q_{X_1}, \tag{41}$$

$$\Delta E^r_{si} = \Delta E^r_{gi} - Q_{\mathrm{TST}} + Q_{X_2}, \tag{42}$$

where ΔE^f_{gi} and ΔE^r_{gi} are the forward and reverse activation energies for the corresponding gas phase reactions. The resulting barriers for the surface isomerization reactions derived using the above methodology are shown in Table 5.

Table 4
Energy barriers for gas phase isomerization reactions in kJ/mol.

Isomerization	ΔE^f_{gi}	ΔE^r_{gi}
$C_2H_4 \Leftrightarrow CHCH_3$	322.4	4.0
$CHCH_2 \Leftrightarrow CCH_3$	229.9	11.5
$CHCH \Leftrightarrow CCH_2$	187.9	4.5

Note. Computations performed using Gaussian 03 at the G3B3 level [99].

Table 5
Energy barriers used to assess the sensitivity to surface isomerization reactions in kJ/mol.

Isomerization reactions	Method 1		Method 2		[26,97]	
	ΔE_f	ΔE_r	ΔE_f	ΔE_r	ΔE_f	ΔE_r
$C_2H_4(s_2) \Leftrightarrow CHCH_3(s_2)$	123	0	176	53	87	50
C_2H_4(s) + Pt(s) $\Leftrightarrow$ $CHCH_3(s_2)$	92	0	145	53	83	75
$CHCH_2(s_3) \Leftrightarrow CCH_3(s_3)$	0	57	21	78	–	–
$CHCH_2$(s) + 2Pt(s) $\Leftrightarrow$ $CCH_3(s_3)$	0	3	117	119	129	176
$C_2H_2(s_3) \Leftrightarrow CCH_2(s_3)$	169	0	248	80	–	–
$C_2H_2(s_3) \Leftrightarrow CCH_2(s_2)$ + Pt(s)	19	0	95	77	61.5	4.2

Note. The activation energies were estimated form the gas phase reactions given in Table 4 with barriers corrected using the enthalpy of reaction (Method 1) and a transition state (TST) approach (Method 2) according to Eq. (40). The heats of adsorption used are consistent with the reaction mechanism given in Appendix A.

5.2.5. Surface diffusion barriers

Shustorovich and Sellers [71] suggested that the apparent activation barrier of a reaction may strongly depend on the diffusive characteristics of surface species involved in the reaction, especially when the intrinsic activation barrier is competitive or smaller than the diffusion barrier of the most strongly bonded reactant. For such cases the apparent or total energy barrier $\Delta E_{a,m}$ is estimated as

$$\Delta E_{a,m} = \psi \Delta E_{\text{int}} + (1-\psi)\Delta E_{\text{dif.}A_s+B_s}, \tag{43}$$

$$\Delta E_{\text{dif.}A_s+B_s} = \frac{2\Delta E_{\text{dif.}A_s}\Delta E_{\text{dif.}B_s}}{\Delta E_{\text{dif.}A_s} + \Delta E_{\text{dif.}B_s}}, \tag{44}$$

where ΔE_{int} denotes the intrinsic barriers (ΔE_s^f, ΔE_s^r, ΔE_g^f and ΔE_g^r) estimated using Eqs. (36)–(39) as appropriate. Experimental studies [102] of the diffusion barrier $\Delta E_{\text{dif.}}$ have resulted in estimated values between 10% and 20% of the adsorbate binding energy. Nilekar et al. [63] have suggested, based on periodic self-consistent DFT calculations for different transition metals, that 12% of the heat of adsorption provides a fairly accurate estimate. In the present work the latter value has been used,

$$\Delta E_{\text{dif.}A_s} = 0.12\mathcal{Q}_A(n). \tag{45}$$

The parameter (ψ) is unity when the intrinsic reaction rate constant is dominant and zero for diffusion limited reactions. Consequently, in the present work ($0 \leqslant \psi \leqslant 1$) is estimated as

$$\psi = \frac{\Delta E_{\text{int}}}{\Delta E_{\text{int}} + \Delta E_{\text{dif.}A_s+B_s}}. \tag{46}$$

6. Semi-automatic generation of surface mechanisms

The initial surface mechanism was automatically generated by implementing the above reaction classes and surface energetics for the 35 adsorbates into a JAVA based tool (Surface Reaction Manager). The applied generation method was based on atom conservation and the subsequent screening featured the use of the Reaction Model Generator (RMG) algorithm derived by Green and co-workers for gas phase reactions [103]. The RMG algorithm is based on a functional group approach and features a recursive iterative method for the generation of comprehensive reaction mechanisms. The current screening process resulted in an exhaustive set of elementary reactions involving all the different adsorbates and originally featured about 12,500 reversible heterogeneous reactions. Such mechanisms are too large to handle comfortably and basic selection criteria included the elimination of reaction steps featuring multiple H transfers and, subsequently, a combination of path, flux and sensitivity analyses was used to derive a shorter model comprising the major reaction pathways. A principal advantage of the approach is that it guarantees a consistent application of the rules associated with each reaction class. The final mechanism listed in Table 7 (see Appendix A) contains 283 reversible elementary reactions and corresponds to the hybrid case with some of the heats of adsorption determined from DFT studies. The alternative mechanism (based exclusively on UBI-QEP data) is included as supplementary material. The reaction rate constants k are presented in the following form,

$$\mathcal{R} = \frac{k}{\Gamma^{m-1}}\prod[X_i], \tag{47}$$

where m indicates the sum of the total number of reactants on the surface and additional Pt(s) sites involved in the reaction. In the present work, only the pre-exponential term for the desorption of CO(s_2) was adjusted in light of previous studies. The frequency factor has been assigned values from 10^{13} to 10^{18} s^{-1} [26,93,107,108]. Zerkle et al. [26] enhanced the desorption rate of CO(s_2) by one order of magnitude above the experimental value proposed by Campbell et al. [83] on the basis of a study of the interactions of CO with a Pt(111) surface over the temperature range 500 to 700 K. The adjusted rate used in the current work is around a factor of two slower than that proposed by Zerkle et al. [26] and was selected on the basis of an extensive sensitivity analysis.

7. Results and discussion

The conversions and selectivities reported here are mass based and all quantities correspond to values integrated radially across the virtual pore. The selectivities are by default estimated with respect to the relative mass of carbon atoms contained in the products examined. The oxygen selectivities to H_2O, CO and CO_2 are also reported. Unless otherwise stated, the discussion in the following sections is based on the hybrid mechanism shown in Table 7. Initially the level of agreement obtained between the computational and experimental studies is outlined and, subsequently, the reaction pathways are discussed with reference to previous studies. The computational simulations were performed using a radial grid of 80 cells and a maximum axial step of 5 μm. The grid was refined close to the surface to provide a radial spatial resolution ≃2 μm.

7.1. The impact of different O/C ratios

The impact of changes in the O/C ratio from 0.45 to 0.75 on the conversion of ethane, oxygen and on selectivities to major products was investigated for inlet velocities of 1.35 and 2.10 m/s. The experimental conditions correspond to Cases 1–12 described in Table 1. The downstream evolution of the radially integrated conversion of ethane and the temperature at the center of the pore are shown in Fig. 1 for Cases 7, 9, 11 and 12 along with experimental data reported at the entrance and exit of the catalyst and at the end of the reactor. It is readily apparent that as the O/C ratios reduce, it becomes progressively more difficult to represent the experimental temperature evolution. However, the temperature profiles are computed with reasonable accuracy for most O/C ratios using a heat loss parameter $\kappa_2 = 0.07$. Hence, the latter value has been used as the current base case and the impact of variations in the value of κ_2 are discussed further below. It is also evident that the consumption of ethane starts within the first 15 mm of the catalytic section and that it follows a sharp rise of the temperature inside the pore. It is also clear that the higher the oxygen content, the higher the temperature in the reactor. For all four cases, a gradual drop in the temperature by about 30 to 50 K is recorded as the flow exits the catalytic section of the pore. The profiles emphasize the key role of the catalyst in releasing heat from the surface into the gas phase. The corresponding axial profiles of the carbon selectivities to C_2H_4, CH_4, CO and CO_2 are shown in Fig. 2. The consumption of oxygen leads almost exclusively to the formation of water at the entrance of the pore with a selectivity of almost 99%. The high initial selectivity to CH_4 at very low C_2H_6 conversion levels is discussed further below. The pattern changes when the consumption of ethane increases and leads to the formation of carbon monoxide and carbon dioxide. Ethylene is produced from the entrance of the pore and for all cases the selectivity initially rises to ∼60% as shown in Fig. 2. As the conversion of ethane increases, the selectivity reaches a plateau around 70% further downstream. For cases with high oxygen content (O/C ratio ⩾0.6), the selectivity decreases to values between 72% and 68% in the second half of the pore as the conversion of fuel becomes significant. This is partly due to the catalytic consumption of C_2H_4 leading to the formation of CO and CH_4. The formation of methane also takes place from the very entrance of the catalyst and rises sharply at low conversions before reducing to a maximum value ∼17% (O/C ratio ⩾0.65) as

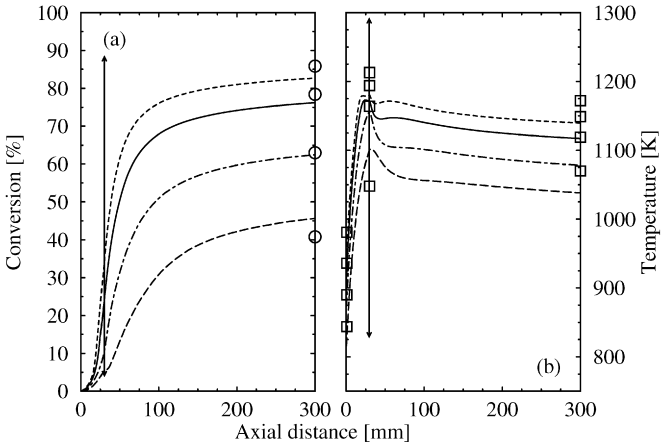

Fig. 1. Calculated axial profiles of (a) ethane conversion and (b) temperatures at the center of the pore for different O/C ratios: 0.45 (dashed lines), 0.55 (dot-dashed lines), 0.65 (solid lines) and 0.70 (short dashed lines) (Cases 7, 9, 11 and 12). The vertical double arrow demarcates the exit of the catalyst. Experimental data available at sampling points for the corresponding cases are shown with symbols. Simulations are presented with $\kappa_2 = 0.07$ and with the mid-point value of the site density.

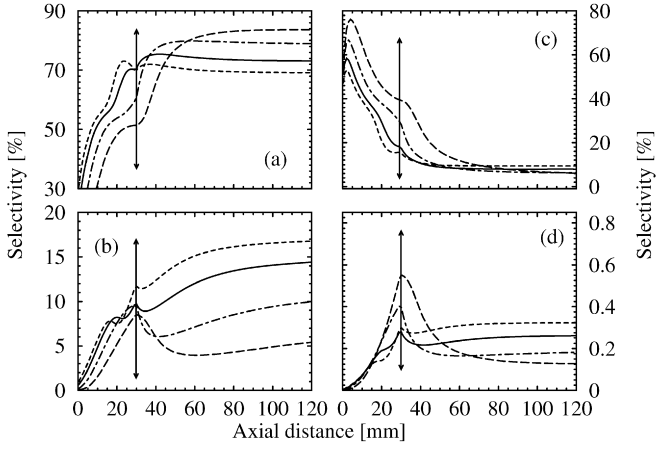

Fig. 2. Calculated axial profiles of selectivity to (a) C_2H_4, (b) CO, (c) CH_4 and (d) CO_2 at different O/C ratios as defined in Fig. 1 (Cases 7, 9, 11 and 12). The vertical double arrow demarcates the exit of the catalyst.

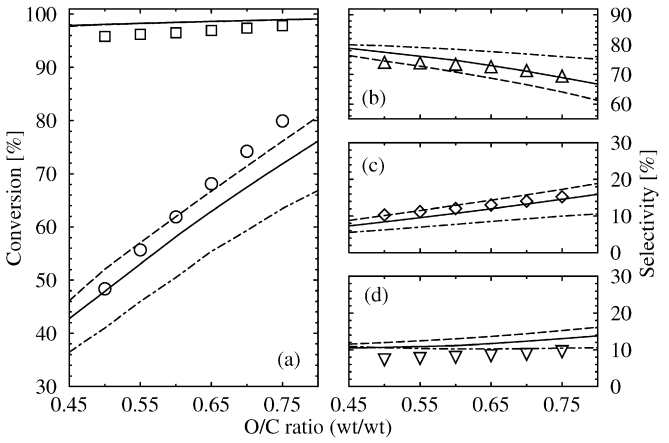

Fig. 3. Simulation results (lines) compared to experimental data (symbols). (a) Ethane (circle) and oxygen (square) conversion, (b) selectivity to ethylene (triangle up), (c) CO (diamond), (d) methane (triangle down) for different O/C ratios with an inlet velocity of 1.34 m/s (Cases 1–6). Simulations were performed using the mid-point value for the site density and with $\kappa_2 = 0$ (dashed lines), $\kappa_2 = 0.07$ (solid lines) and $\kappa_2 = 0.15$ (dot-dashed lines).

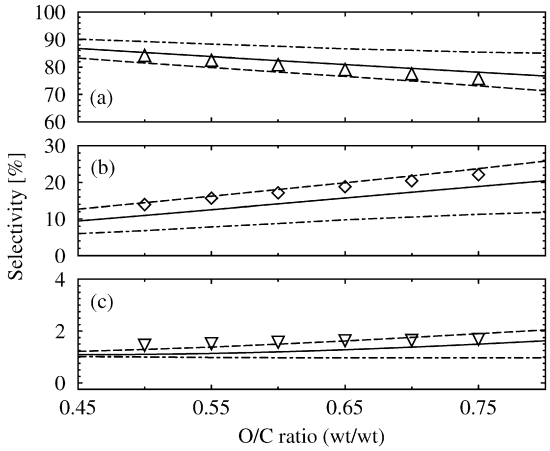

Fig. 4. Simulation results (lines) compared to experimental data (symbols). O-selectivity to (a) H_2O (triangle up), (b) CO (diamond) and (c) CO_2 (triangle down) for different O/C ratios with an inlet velocity of 1.34 m/s (Cases 1–6). Simulations were performed using the mid-point value for the site density and with $\kappa_2 = 0$ (dashed lines), $\kappa_2 = 0.07$ (solid lines) and $\kappa_2 = 0.15$ (dot-dashed lines).

the process favors ethylene formation. A high oxygen content (O/C ratio $\geqslant$0.65) and high Pt site densities also promote methane formation on the catalyst. The reaction pathways responsible for the rather complex behavior are discussed further in the path analysis section below.

The high initial selectivity to methane originates from the C–C bond cleavage of ethane via direct dissociative adsorption or following molecular adsorption. The $CH_3(s) + H(s)$ associative desorption follows as one of the reaction channels. Sensitivity analyses indicate that under the current conditions the methane yield is relatively insensitive to the adsorption of methane. Furthermore, due to the rapid heterogeneous oxidation of hydrogen, the oxidation of $CH_3(s)$ does not play a major role. The magnitude of the dissociative adsorption of ethane affects the methane yield. However, the key controlling parameter is the ratio between the hydrogenolysis and pyrolitic sequences. Several studies have been performed where the UBI–QEP method appears as the recurrent technique used to estimate the energetics of the reactions involved. Deutschmann et al. [104,105] suggested that the non-activated dissociative adsorption of methane was followed directly by the rapid breaking of the three methyl C–H bonds with forward energy barriers estimated at 20 kJ/mol. However, these barriers contrast with the molecular beam experiments by Sun and Weinberg [106] who reported an apparent barrier of 60 kJ/mol. Wolf et al. [97] derived the energetics of the sequential reactions using the UBI–QEP method but altered the barriers for the sequential thermal decomposition channels to emphasize the dehydrogenation sequence. Zerkle et al. [26] retained these rates. By contrast, Aghalayam et al. [22] studied a range of systems without any amendments to the energetics. In the current work the enthalpies derived using the UBI–QEP method have been retained and the reasonably good predictions obtained for the methane selectivity suggest a contribution of the hydrogenolysis mechanism. More extended comparisons between experimental data and computations are shown in Figs. 3 to 7 for the lower inlet velocity case and in Figs. 8 and 9 for the higher velocity case. The results from parametric variations aimed at further assessing the impact of heat losses (Figs. 3 and 4), different sets of heats of adsorption (Figs. 5 to 7) and catalyst site densities (Figs. 8 and 9) are also shown.

To assess the influence of heat losses, different values of κ_2 were used and simulations performed for the range $0 \leqslant \kappa_2 \leqslant 0.15$, with $\kappa_2 = 0.07$ leading to a maximum reduction in temperature of about 60 K. The results shown in Figs. 3 and 4 indicate that

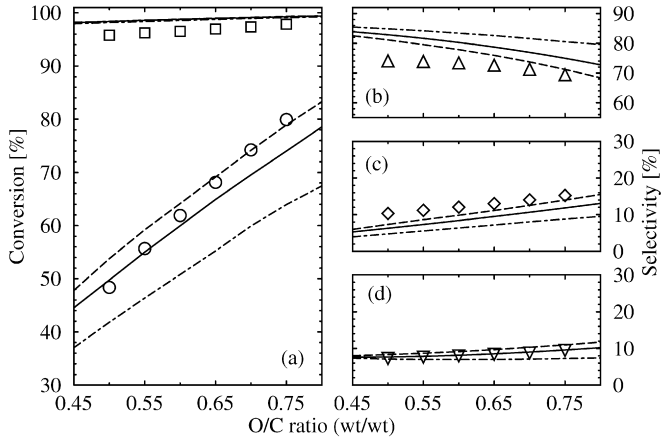

Fig. 5. Simulation results (lines) compared to experimental data (symbols) and with the alternative (lower) heats of adsorption of ethylene, corresponding to 29.3 kJ/mol for $C_2H_4(s)$ and 46.1 kJ/mol for $C_2H_4(s_2)$, and other species as listed in Table 2. (a) Ethane (circle) and oxygen (square) conversion, (b) selectivity to ethylene (triangle up), (c) CO (diamond), (d) methane (triangle down) for different O/C ratios with an inlet velocity of 1.34 m/s (Cases 1–6). Simulations were performed using the mid-point value for the site density and with $\kappa_2 = 0$ (dashed lines), $\kappa_2 = 0.07$ (solid lines) and $\kappa_2 = 0.15$ (dot-dashed lines).

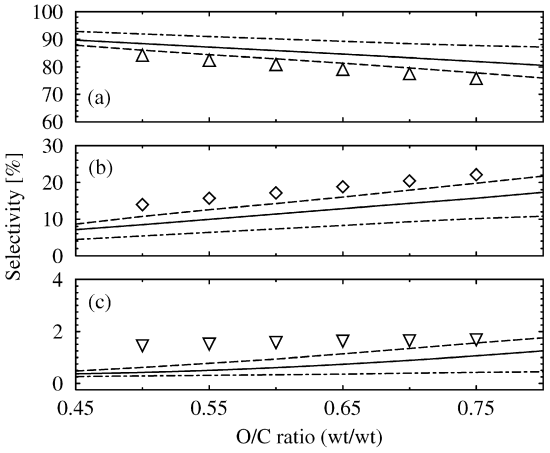

Fig. 6. Simulation results (lines) compared to experimental data (symbols) with the alternative (lower) heats of adsorption as listed in Table 2. O-selectivity to (a) H_2O (triangle up), (b) CO (diamond) and (c) CO_2 (triangle down) for different O/C ratios with an inlet velocity of 1.34 m/s (Cases 1–6). Simulations were performed using the mid-point value for the site density and with $\kappa_2 = 0$ (dashed lines), $\kappa_2 = 0.07$ (solid lines) and $\kappa_2 = 0.15$ (dot-dashed lines).

heat losses have a relatively strong impact on the conversion rate of ethane. However, the selectivities to ethylene and minor products are somewhat less affected. It is also shown that $\kappa_2 = 0.07$, consistent with the temperature profiles discussed above, arguably provides the best overall agreement with experimental data. Calculations using an inlet temperature increased by 50 K were also performed to assess the impact of uncertainties in initial conditions. The results show that an increased preheat will moderately increase the conversion of reactants with only a minor impact upon the carbon distribution. The O-selectivities to H_2O, CO and CO_2 are only marginally affected.

Results obtained with the UBI–QEP based mechanism, resulting from the alternative set of heats of adsorption given in Table 2, are shown in Figs. 5 to 7. The qualitative trends are identical as compared to the hybrid mechanism, but with the UBI–QEP variant predicting higher ethylene and lower methane selectivities. A direct comparison of the two mechanisms is shown in Fig. 7, where selectivities have been plotted against fuel conversion. Overall, it is arguable that the hybrid model provides better agreement with

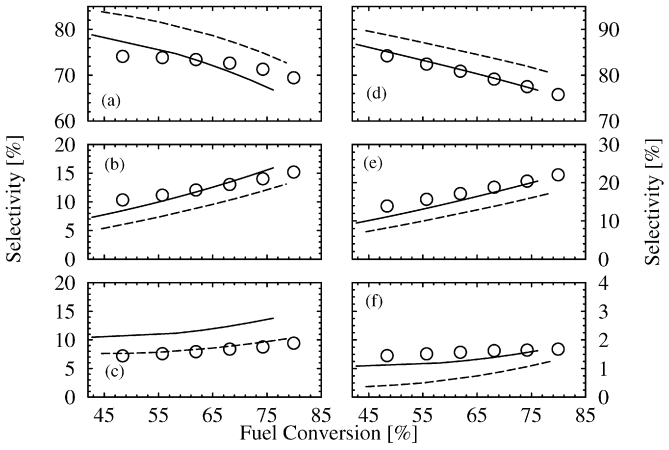

Fig. 7. Simulation results (lines) compared to experimental data (symbols). Conversion of fuel against C-selectivity to (a) C_2H_4, (b) CO, (c) CH_4 and O-selectivity to (d) H_2O, (e) CO and (f) CO_2. Simulations were performed with the two mechanisms corresponding to the heats of adsorption of selected species set to the (lower) alternative (dashed lines) and standard (solid lines) values listed in Table 2 (also see text). Simulations were performed using the mid-point value for the site density and with $\kappa_2 = 0.07$.

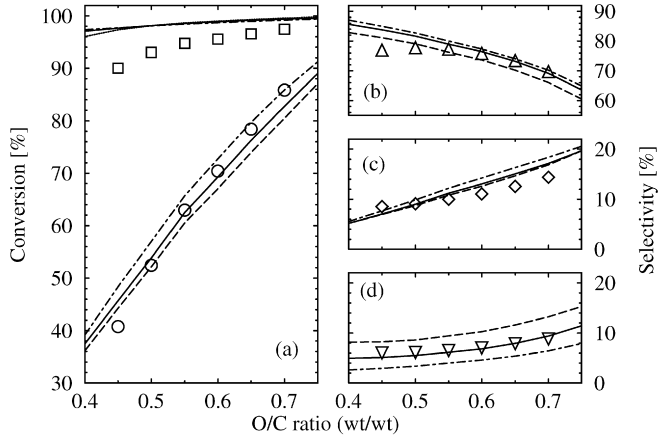

Fig. 8. Simulation results (lines) compared with experimental data (symbols). (a) C_2H_6 (circle) and O_2 (square) conversion, (b) selectivity to C_2H_4 (triangle up), (c) CO (diamond), (d) CH_4 (triangle down) for different O/C ratios with an inlet velocity of 2.10 m/s (Cases 7–12). Simulations are presented for $\kappa_2 = 0.07$ and with Γ (solid lines), Γ_{max} (dashed lines) and Γ_{min} (dot-dashed lines).

the experimental data. However, the discrepancies for the selectivity to ethylene can also partly be attributed to the formation of higher hydrocarbons, which are not considered in the present study, and the yield of such species may approach several percent at lower O/C ratios. It is nonetheless evident that the UBI–QEP based approach has the ability to reproduce measured trends with reasonable accuracy. The increased tendency of the hybrid mechanism to promote the formation of methane is discussed in the path analysis section and it is important to note that changes in the platinum site density influence results.

The impact of uncertainties in the active platinum sites density (Γ) was assessed by first considering Γ equal to the mid-point value of 7.5×10^{-5} mol/m^2 and, subsequently, computations were also performed with the limiting values $\Gamma_{min} = 5 \times 10^{-5}$ mol/m^2 and $\Gamma_{max} = 10 \times 10^{-5}$ mol/m^2. Computed results are shown in Figs. 8 and 9 for Cases 7–12. Comparisons of predictions with experimental data suggest, as shown in Fig. 8, that a higher platinum loading increases the consumption of oxygen, has a detrimental impact on the selectivity to C_2H_4 and results in increased yields of secondary products (e.g., CH_4). The results presented in Fig. 8 also show that the conversion of ethane increases from 41% to 85%

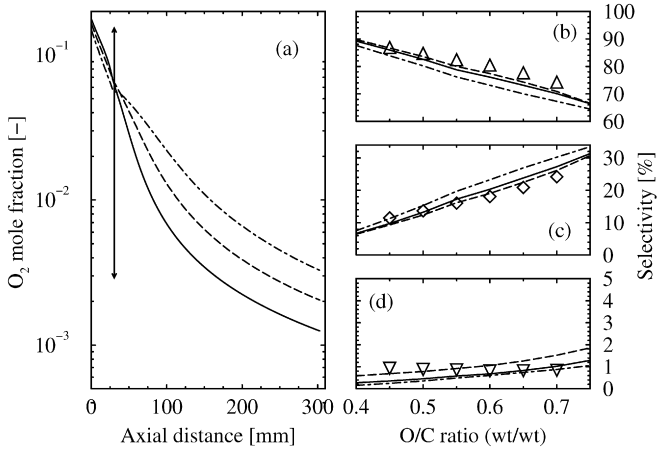

Fig. 9. Simulation results (lines) compared with experimental data (symbols). (a) O_2 molar fraction along the center line of the pore for O/C ratio equal to 0.45 (dashed lines), 0.55 (dot-dashed line) and 0.65 (solid line). O-selectivity to (b) H_2O (triangle up), (c) CO (diamond) and (d) CO_2 (triangle down) for different O/C ratios with an inlet velocity of 2.10 m/s (Cases 7–12). Simulations are presented for $\kappa_2 = 0.07$ and with Γ (solid lines), Γ_{max} (dashed lines) and Γ_{min} (dot-dashed lines). The vertical double arrow demarcates the exit of the catalyst.

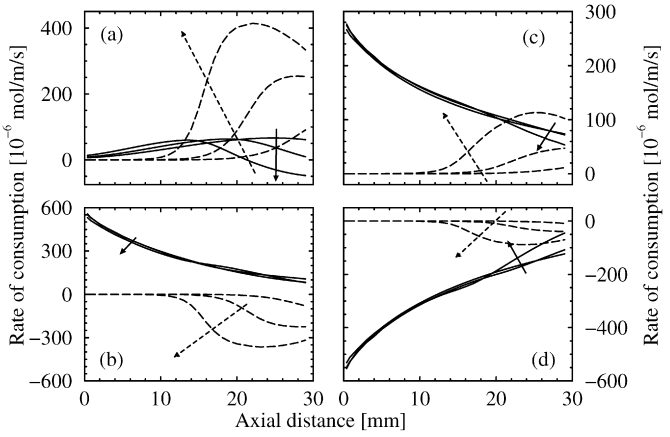

Fig. 10. Calculated rates of consumption of (a) C_2H_6, (b) H_2, (c) O_2 and (d) H_2O from heterogeneous reactions (solid lines) and gas-phase processes (dashed lines) above the catalytic section of the pore for Cases 7, 9 and 11 with $\kappa_2 = 0.07$. Negative values indicate the compound is being produced. The arrows indicate the profile shift when the O/C ratio is progressively increased as 0.55, 0.65 and 0.75.

as the feed becomes more oxygen rich. The measured conversion of oxygen also increases from around 90% to 98%. The experimental selectivity to ethylene falls gradually from 76% to 69% as the ethane content in the system decreases. By contrast, the selectivity to CO rises from 7% to 14% and that of CH_4 from 6% to 9%. The distribution of oxygen, shown in Fig. 9, suggests that for all conditions less H_2O and more CO is produced as the oxygen content is increased. The selectivity to CO_2 remains around 1% for all cases. Application of the mid-point value for the site density generally leads to good agreement with experimental data for the calculated selectivities. The uncertainties in the applied chemistry are naturally likely to contribute to the observed discrepancies. However, the over-prediction of the conversion of oxygen, particularly at low O/C ratios, shown in Figs. 3 and 8, are influenced by overall heat losses. The calculated axial mole fraction profiles of oxygen, shown in Fig. 9, indicate that the consumption rates of oxygen remain relatively unchanged over the catalytic region as the O/C ratio of the feed is varied between 0.45 and 0.65. The mole fraction profiles of oxygen differ only when the streams flow deeper in the reactor where the gas phase reactions become predominant.

The pattern shown in Fig. 2 is further exemplified in Fig. 10, where the calculated consumption and production rates of C_2H_6, O_2, H_2 and H_2O are given for catalytic reactions under different conditions. Ethane is mainly consumed via catalytic reactions up to a distance of ~14 mm downstream. Subsequently, the gas phase reactions are initiated by the sharp temperature rise shown in Fig. 1. The ignition point will move upstream as the oxygen content or the site density is increased. With an O/C ratio of 0.65, the radially integrated rate of gas phase consumption peaks at $\simeq 250 \times 10^{-6}$ mol m^{-1} s^{-1} (see Fig. 10) in the second half of the pore and subsequently declines. The oxygen consumption presents a very different pattern. Throughout the catalytic section, O_2 is consumed predominantly at the wall and the surface reactions rapidly reach values $\sim 300 \times 10^{-6}$ mol m^{-1} s^{-1} and account for close to 100% of the consumption. Similarly to ethane, the oxygen consumption in the gas phase initiates only downstream at a distance of around 16 mm and reaches a smaller peak value $\sim 50 \times 10^{-6}$ mol m^{-1} s^{-1} as the stream exits the catalyst. At this point, the gas phase contributes around 40% of the total consumption. The predominant role of the surface mechanisms indicates that the radial flux bringing O_2 toward the wall is a major factor in the depletion of oxygen. Hence, oxygen residuals may depend strongly on the presence of radial stratification.

For Case 11, the switch from catalytic to gas phase production of C_2H_4 occurs in the second third of the catalytic section. It is, however, important to note that for the upper limit value (Γ_{max}) the catalyst effectively consumes ethylene produced in the gas phase at distances beyond 16 mm downstream. While the normalized gas phase contribution is close to 1 toward the end of the catalytic section, the contribution of the catalytic processes decreases from 0 to −0.20 indicating significant surface consumption of ethylene. This explains the rising catalytic contribution to the production of CO following gas phase ignition and the dominant surface production of CH_4 throughout the catalyst. The dynamic balance between the gas and surface chemistry contributions provides an explanation for the effect of site density on the selectivities to CO, CO_2, CH_4 and H_2O shown in Figs. 8 and 9. An increase of the catalytic activity will effectively enhance the downstream consumption of ethylene and oxygen leading to increases in the selectivities to methane and water. The modest reduction in the overall selectivity to CO, as Γ is shifted from the lower to the upper limit, can be related to preferential production of water on the surface and the related reduction of O_2 in the gas phase. The complete oxidation of carbonaceous species is, however, linearly related to the increase in the formation of CO_2.

7.2. Impact of reactor residence time

The rate of flow through the catalyst has a major influence on reactant conversion and reaction stability. In the present work, the superficial inlet velocity (at 273 K) was varied from about 2 to 7 m/s to explore the ability of the model to reproduce the reaction dynamics and the blow-off point. This is a challenging task with results directly dependent upon the rate of heat release induced by the catalyst and the resulting balance of heterogeneous and homogeneous reactions. The experimental conditions are described in Table 1 and correspond to Cases 11, 13–16. Model predictions can be seen in Fig. 11 for the case $H_2/O_2 = 2$ and O/C = 0.65. The sensitivity to the site density of platinum was again explored using the limiting values and the impact was noticeable at the highest inlet velocities as discussed below. The results obtained with the mid-point value of Γ show that the conversion of C_2H_6 drops from about 79% at 2.18 m/s to 44% when the gas flow inlet velocity is increased to 6.72 m/s. The conversion of oxygen drops from 98% to 83%. The behavior is reflected in the

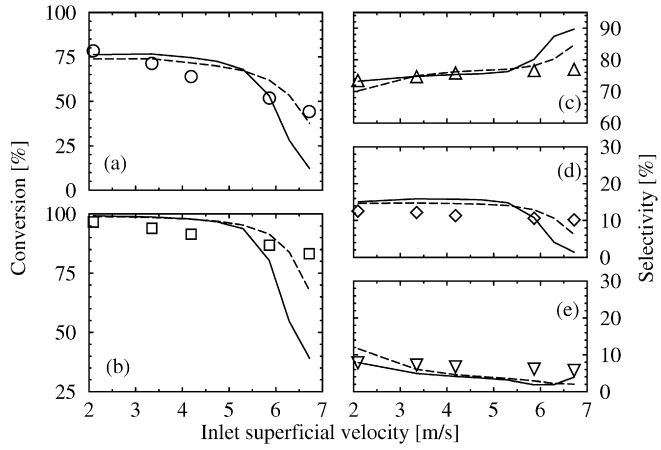

Fig. 11. Simulation results (lines) compared with experimental data (symbols). (a) C_2H_6 (circle) and (b) O_2 (square) conversions. Selectivity to main products: (c) C_2H_4 (triangle up), (d) CO (diamond), (e) CH_4 (triangle down) at different inlet velocities (Cases 11, 13–16). Simulations with $\kappa_2 = 0.07$, the mid-point value of Γ (solid lines) and Γ_{max} (dashed line).

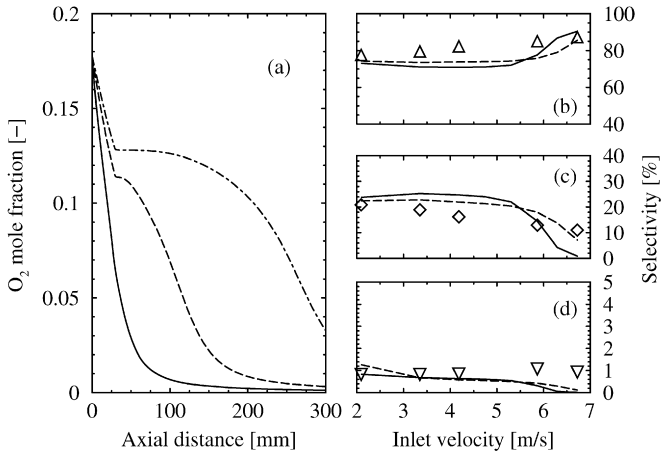

Fig. 12. Simulation results (lines) compared to experimental data (symbols). (a) O_2 molar fraction along the pore for 2.10 m/s (solid line), 4.18 m/s (dashed line), 5.86 m/s (dot-dashed line) inlet velocities. O-selectivity to (b) H_2O (triangle up), (c) CO (diamond), (d) CO_2 (triangle down) at different inlet velocities and with O/C equal to 0.65 (Cases 11, 13–16). Simulations with $\kappa_2 = 0.07$ and the mid-point value of Γ (solid lines) and Γ_{max} (dashed line).

predicted oxygen profiles shown in Figs. 11 and 12. The computations suggest that as the flow rate increases, the oxygen residual at the exit of the reactor rises from about 1200 ppm at 2.18 m/s to about 32,000 ppm at 5.86 m/s. The distribution of carbon to major products is not strongly affected by the change in the inlet velocity until close to blow-off. For example, the selectivity to ethylene increases marginally from 74% to 76% as the velocity is increased. The selectivity to H_2O rises from 78% to 87% while that of CO is reduced from 22% to 11%. The simulations have a tendency to over-predict the conversion of the reactants, but the blow-off point is reproduced with reasonable accuracy. The computational value of $\simeq$6.5 m/s, obtained with the mid-point site density Γ, is reasonably close to the experimental value $\simeq$7 m/s and computations provide encouraging agreement with experimental data up to a velocity of 6 m/s. The computed blow-off velocity obtained with Γ_{min} (not shown) was around 5.5 m/s and the corresponding value for Γ_{max} was around 7 m/s. The computed selectivities to C_2H_4, CO and CO_2 are fairly accurate, while the production of CH_4 tends to be under-predicted—in contrast to the results discussed above.

The behavior of the system becomes of greater interest as the flow velocity is increased. Besides the drop in ethane conversion, the computations provide insight into the incipient failure of the catalyst to initiate chemical reaction in the gas phase. The latter is particularly noticeable when the inlet velocity exceeds 5 m/s. A change in the catalyst site density leads to a similar qualitative behavior but a change in the onset of failure. The results emphasize the increasing sensitivity to the platinum loading as the critical regime of around 5 m/s is approached. This is confirmed by the radially integrated conversion of ethane and oxygen in the first 200 mm of the pore. As the flow rate is raised, the initiation of ethane consumption is delayed and the reactant gas streams penetrate deeper in the pore. At a velocity of 2.18 m/s, the homogeneous conversion of fuel starts within the first 15 mm of the entrance of the pore, whereas at velocities higher than 5 m/s the consumption of fuel becomes significant only after 50 to 80 mm after the exit of the catalytic section, indicating complete blow-off of the gas phase reactions. The situation is qualitatively similar when the highest site density is used. However, homogeneous reactions are initiated much closer to the exit of the catalyst.

The pattern for oxygen consumption is very different. Although the conversion of oxygen declines at higher velocities, consumption begins at the entrance of the pore, but at a rate that decreases as the flow rate increases. At velocities of 4.18 and 5.86 m/s, the conversion of oxygen stabilizes momentarily at $\simeq$40% and $\simeq$32% at the exit of the catalyst and then increases again 50 and 100 mm downstream. With the upper limit of the site density, the corresponding conversion at 5.86 m/s is $\simeq$42%. It is again evident that the catalytic oxidation of H_2, is the key contributor to the thermal balance of the reactor. However, if the flow rate in the pore is too high, then most of the thermal energy released into the gas phase will simply be convected away without triggering the gas phase reactions. Increasing the flow rate reduces the residence time and at higher velocities the catalyst remains a net producer of ethylene. Accordingly, the overall C_2H_4 selectivity will tend to increase marginally.

8. Chemical mechanisms and path analysis

The dominant heterogeneous reactions of ethane over a supported platinum catalyst and the associated pathways are discussed in more detail in the following sections.

8.1. Heterogeneous oxidation of hydrogen

The rapid catalytic consumption of oxygen at the entrance of the pore and the high selectivity to water constitutes the principal initial mechanism under the current conditions. The associated rapid preferential oxidation of hydrogen, leading to early heat release, is consistent with a range of experimental studies, including the early work by Huff and Schmidt [4]. The adsorption of oxygen is typically treated [19,22,24,26,61,109,110] as a direct dissociative process forming two oxygen atoms on the surface. However, Campbell et al. [122] suggested, on the basis of molecular beam/surface scattering techniques, that the dissociation of adsorbed O_2(s) is the rate limiting process. The suggestion is consistent with the theoretical study of water formation on platinum by Jacob et al. [123]. Luntz et al. [124] used X-ray photoelectron spectroscopy to study the kinetics of oxygen adsorption and suggested a sequential process with a physisorbed state preceding a molecularly chemisorbed state followed by dissociation. The current sticking coefficient for the dissociative adsorption of oxygen (R527) features the functional form used by Zerkle et al. [26] with the value reduced by 30% to conform with Campbell et al. [122]. The resulting sticking coefficient at 1050 K is close to 0.015 as compared to 0.02 [26]. Raimondeau et al. [107] preferred a temperature independent

Table 6
Path analysis for the consumption of O_2 and production of H_2O at a distance 5 mm inside the pore for Case 11 (the overall percentage contribution of the matching reaction is denoted Abs. %).

No.	Consumption of O_2	Abs. %
489	$O_2 + 2Pt(s) \rightleftarrows O_2(s_2)$	43
491	$O_2 + H(s) + Pt(s) \rightleftarrows O(s) + OH(s)$	7
493	$O_2 + 2Pt(s) \rightleftarrows O(s) + O(s)$	43
495	$O_2 + H(s) \rightleftarrows OOH(s)$	7
	Consumption of H_2	Abs. %
483	$H_2 + Pt(s) \rightleftarrows H_2(s)$	99
	Consumption of $H_2(s)$	Abs. %
521	$H_2(s) + O(s) \rightleftarrows H(s) + OH(s)$	1
523	$H_2(s) + Pt(s) \rightleftarrows H(s) + H(s)$	99
	Consumption of $O_2(s_2)$	Abs. %
525	$O_2(s_2) + H(s) \rightleftarrows O(s) + OH(s) + Pt(s)$	4
527	$O_2(s_2) \rightleftarrows O(s) + O(s)$	92
529	$O_2(s_2) + H(s) \rightleftarrows OOH(s) + 2Pt(s)$	4
	Consumption of OOH(s)	Abs. %
553	$OOH(s) + H(s) \rightleftarrows O(s) + H_2O(s)$	9
557	$OOH(s) + H(s) \rightleftarrows OH(s) + OH(s)$	9
563	$OOH(s) + Pt(s) \rightleftarrows O(s) + OH(s)$	80
	Consumption of O(s)	Abs. %
521	$H_2(s) + O(s) \rightleftarrows H(s) + OH(s)$	1
535	$H(s) + O(s) \rightleftarrows OH(s) + Pt(s)$	98
	Consumption of H(s)	Abs. %
535	$H(s) + O(s) \rightleftarrows OH(s) + Pt(s)$	9
537	$H(s) + OH(s) \rightleftarrows H_2O(s) + Pt(s)$	9
539	$H(s) + OH(s) \rightleftarrows H_2O + 2Pt(s)$	1
541	$H(s) + H(s) \rightleftarrows H_2 + 2Pt(s)$	60
	Consumption of OH(s)	Abs. %
537	$Hs) + OH(s) \rightleftarrows H_2O(s) + Pt(s)$	87
539	$H(s) + OH(s) \rightleftarrows H_2O + 2Pt(s)$	12
	Consumption of $H_2O(s)$	Abs. %
551	$H(s) + H_2O(s) \rightleftarrows H_2(s) + OH(s)$	8
561	$H_2O(s) \rightleftarrows H_2O + Pt(s)$	93

value of 0.1, while Mhadeshwar and Vlachos [23] preferred a functional form resulting in a value of 0.14 at the same temperature. The latter value is too high to be consistent with the current work. However, the potential role of molecular oxygen on the surface was explored by introducing an additional channel (R489) resulting in a maximum total sticking probability of 0.03 at 1050 K.

$$O_2 + 2Pt(s) \rightleftarrows O(s) + O(s), \quad \text{(R493)}$$

$$O_2 + 2Pt(s) \rightleftarrows O_2(s_2), \quad \text{(R489)}$$

$$O_2(s_2) \rightleftarrows O(s) + O(s), \quad \text{(R527)}$$

$$H_2 + Pt(s) \rightleftarrows H_2(s), \quad \text{(R483)}$$

$$H_2(s) + Pt(s) \rightleftarrows H(s) + H(s). \quad \text{(R523)}$$

The major catalytic pathways are shown in Table 6, where each reaction is presented along with its percentage contribution to the overall net consumption for both gas and surface phases. As may be expected, due to the high temperatures and low dissociation barrier for $O_2(s_2)$, reactions (R489) and (R527) can essentially be combined. It is also clear that $H_2(s)$ does not prevail on the surface and that the dominant path leads to H(s), suggesting that (R483) and (R523) can also be combined. However, as also shown, a small fraction of the adsorbed hydrogen ($\simeq$1%) and oxygen (8%) is attacked by O(s) and H(s) via (R521), (R525), (R529). Molecular oxygen also reacts (14%) directly with hydrogen atoms already on the surface (R491, R495) leading to O(s) and OH(s) either directly or via OOH(s). The major subsequent catalytic reaction paths proceed via (R535), (R537), (R561).

$$H(s) + O(s) \rightleftarrows OH(s) + Pt(s), \quad \text{(R535)}$$

$$H(s) + OH(s) \rightleftarrows H_2O(s) + Pt(s), \quad \text{(R537)}$$

$$H_2O(s) \rightleftarrows H_2O + Pt(s). \quad \text{(R561)}$$

The heterogeneous depletion of oxygen is maintained along the catalytic section as long as oxygen is present in the gas phase adjacent to the wall. Consequently, at 29 mm inside the pore, catalytic reactions still account for more than 60% and 99% of the total consumption of O_2 and H_2. Accordingly, the above reaction channels are the key providers of heat in the proximity of the wall.

8.2. Ethane oxidative dehydrogenation

The consumption of C_2H_6 is predominantly through catalytic reactions at the entrance of the pore. The major pathways involved in the transformation of C_2H_6 into ethylene at a distance of 5 mm from the entrance of the pore are shown in Fig. 13 along with their total respective contributions. The molecular adsorption leading to $C_2H_6(s_2)$ (R1) contributes about 88% of the overall consumption of ethane at this point. The dissociative channel (R7) contributes 3%, while the dissociative adsorption (R9) leading to $CH_2CH_3(s)$ accounts for 8%.

$$C_2H_6 + 2Pt(s) \rightleftarrows C_2H_6(s_2), \quad \text{(R1)}$$

$$C_2H_6 + 2Pt(s) \rightleftarrows CH_3(s) + CH_3(s), \quad \text{(R7)}$$

$$C_2H_6 + 2Pt(s) \rightleftarrows H(s) + CH_2CH_3(s). \quad \text{(R9)}$$

Surface methyl predominantly desorbs associatively with hydrogen atoms leading to methane via (R303).

$$CH_3(s) + H(s) \rightleftarrows CH_4 + 2Pt(s). \quad \text{(R303)}$$

The dissociative adsorption channel leading to $CH_3(s)$ is further augmented by a fraction (34%) of $C_2H_6(s_2)$ decomposing to $CH_3(s)$ via reaction (R111) and a smaller amount (5%) via reaction (R115) with H(s). However, the major channels lead to $CH_2CH_3(s)$ and proceed through reaction (R113) with H(s) (5%) or via direct decomposition (55%) through reaction (R125). The above pathways support the possibility of early C–C bond scission [12,15] as a secondary channel and indicate that the branching ratio between C–C and C–H cleavage for $C_2H_6(s_2)$ is a key parameter at this stage in the process.

$$C_2H_6(s_2) \rightleftarrows CH_3(s) + CH_3(s), \quad \text{(R111)}$$

$$C_2H_6(s_2) + H(s) \rightleftarrows H_2(s) + CH_2CH_3(s) + Pt(s), \quad \text{(R113)}$$

$$C_2H_6(s_2) + H(s) \rightleftarrows CH_4 + CH_3(s) + 2Pt(s), \quad \text{(R115)}$$

$$C_2H_6(s_2) \rightleftarrows H(s) + CH_2CH_3(s). \quad \text{(R125)}$$

In qualitative agreement with other studies (e.g., [10]), the decomposition of $CH_2CH_3(s)$ provides a direct channel for the catalytic production of ethylene with $\geqslant$99% decomposing directly to $C_2H_4(s_2)$ via (R145) and less than 1% dehydrogenating via hydrogen radical attack (R147).

$$CH_2CH_3(s) + 2Pt(s) \rightleftarrows H(s) + C_2H_4(s_2), \quad \text{(R145)}$$

$$CH_2CH_3(s) + H(s) + Pt(s) \rightleftarrows H_2(s) + C_2H_4(s_2). \quad \text{(R147)}$$

The current mechanism also suggests a potentially important role of π-bonded $C_2H_4(s)$. At the entrance, the net flux between the two C_2H_4 isomers on the surface indicates that more than 99% of di-σ bonded ethylene turns into π-bonded $C_2H_4(s)$ via (R167)

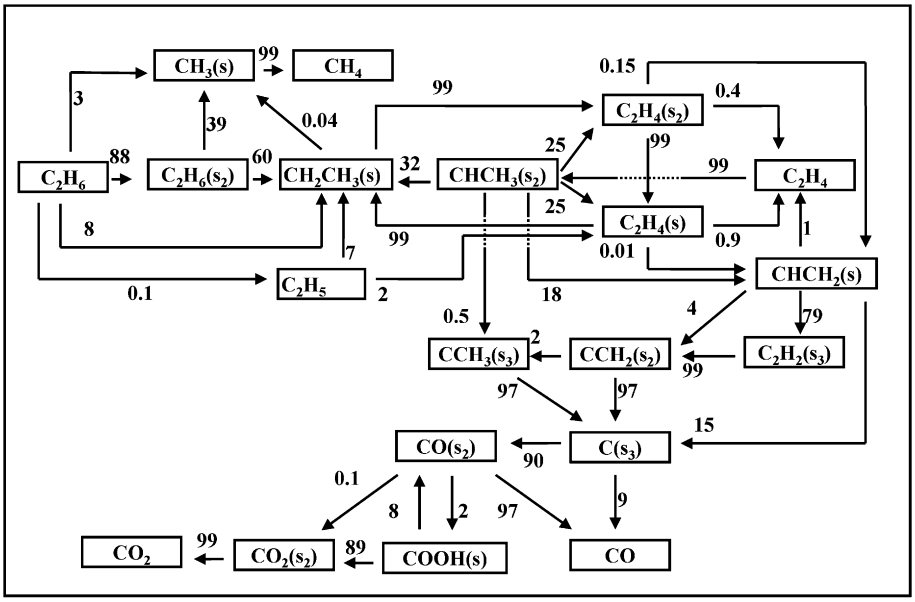

Fig. 13. Major channels in the heterogeneous reaction mechanism of ethane and ethylene on the surface at a distance of 5 mm from the entrance of the pore. Figures correspond to the cumulative contribution (in percentage) of all reactions involved in the path consuming the involved species and producing the target compound.

and a smaller fraction $\leqslant 1\%$ desorbs directly into the gas phase via (R165).

$$C_2H_4(s_2) \rightleftarrows C_2H_4 + 2Pt(s), \quad \text{(R165)}$$

$$C_2H_4(s_2) \rightleftarrows C_2H_4(s) + Pt(s). \quad \text{(R167)}$$

A combination of the former reactions (R1), (R9), (R113), (R125), (R145) tends to support the adsorption of ethane to ethyl and hydrogen and the direct transformation to di-σ ethylene on the surface as favored by Loaiza et al. [8], Zerkle et al. [26] and Zaera [111]. Nonetheless, reaction (R167) introduces $C_2H_4(s)$ as a key intermediate in the branching ratio between ethylene desorption and rehydrogenation. The π-bonded $C_2H_4(s)$ mainly recombines (99%) with H(s) via (R149) to form $CH_2CH_3(s)$, establishing a recycling mechanism between ethyl, di-σ and π-bonded ethylene. A small fraction also desorbs into the gas-phase (1%) via (R151). Accordingly, not only has the di-σ configuration an important role as suggested by other investigators (e.g., [8,26,111]), but the π-bonded structure also makes a key contribution as proposed in other studies (e.g., Cremer et al. [16]).

$$C_2H_4(s) + H(s) \rightleftarrows CH_2CH_3(s) + Pt(s), \quad \text{(R149)}$$

$$C_2H_4(s) \rightleftarrows C_2H_4 + Pt(s). \quad \text{(R151)}$$

The uncertainties regarding the enthalpies of adsorption of ethylene have been outlined above. However, it may be noted that an increase in the heats of adsorption of both π and di-σ bonded ethylene from the lower limit values of 29.3 and 46.1 kJ/mol to the hybrid mechanism values of 68 and 99 kJ/mol [38] does not alter the qualitative picture. The mechanism thus remains consistent with a fast rehydrogenating pathway [16]. However, the calculations also suggest that higher binding energies for ethylene will decrease the desorption rates and shifts the balance toward the rehydrogenation process leading to ethyl radicals and ethane on the surface. It is also evident that dehydrogenation channels become more active leading to an overall reduction in the selectivity to ethylene.

The rate of desorption of ethylene has an influence on the process and has proved problematic in past work. For example, Wolf et al. [97] reported a frequency factor as high as 10^{16} s^{-1} as part of an investigation of the kinetics of oxygen-free methane conversion on a platinum catalyst. The three order of magnitude difference, compared to the nominal value of $\simeq 10^{13}$ s^{-1}, was attributed to the influence of the reaction entropy on the pre-exponential term. By contrast, the study of the desorption, decomposition and deuterium exchange reactions of unsaturated hydrocarbons on Pt(111) crystal faces by Salmerón and Somorjai [112], indicated an upper limit frequency factor of 10^{12} s^{-1} at 285 K. The reaction was accordingly subjected to a sensitivity analysis using all data sets considered in the present study and the frequency factors derived using the current methodology ($\simeq 2 \times 10^{13}$ s^{-1} at 1050 K) appear satisfactory for the current purposes.

The gas phase mechanisms evolve more gradually and, although their absolute contributions are negligible at the entrance of the pore, at a distance of 5 mm the homogeneous chemistry is initiated via C_2H_5 and CH_3 radical formation. Thermal decomposition (R74) contributes 24% and molecular oxygen (R195) attack 5% with hydrogen abstraction reactions (R191), (R197) contributing predominantly via H (40%) and CH_3 (18%) radical attack.

$$C_2H_6 \rightleftarrows CH_3 + CH_3, \quad \text{(R74)}$$

$$C_2H_6 + H \rightleftarrows C_2H_5 + H_2, \quad \text{(R191)}$$

$$C_2H_6 + O_2 \rightleftarrows C_2H_5 + HO_2, \quad \text{(R195)}$$

$$C_2H_6 + CH_3 \rightleftarrows C_2H_5 + CH_4. \quad \text{(R197)}$$

Subsequently, thermal decomposition and $C_2H_5 + O_2$ reactions (R184, R185), (R188), (R259), leading predominantly to HO_2, are the major C_2H_4 production channels.

$$C_2H_4 + H \rightleftarrows C_2H_5, \quad \text{(R169)}$$

$$C_2H_5 + O_2 \rightleftarrows C_2H_4 + HO_2, \quad \text{(R184, R185)}$$

$$C_2H_5 + O_2 \rightleftarrows C_2H_5OO, \quad \text{(R188)}$$

$$C_2H_5OO \rightleftarrows C_2H_4 + HO_2. \quad \text{(R259)}$$

At a distance of 5 mm downstream, C_2H_5 produced in the gas phase is chemisorbed leading to $CH_2CH_3(s)$ ($\sim$7%) via reaction (R11) and $C_2H_4(s)$ ($\sim$2%) via reaction (R13). Smaller quantities of other hydrocarbons are also formed through complementary channels. The latter reactions are only of importance in the sense that the formation of carbonaceous species on the surface may proceed

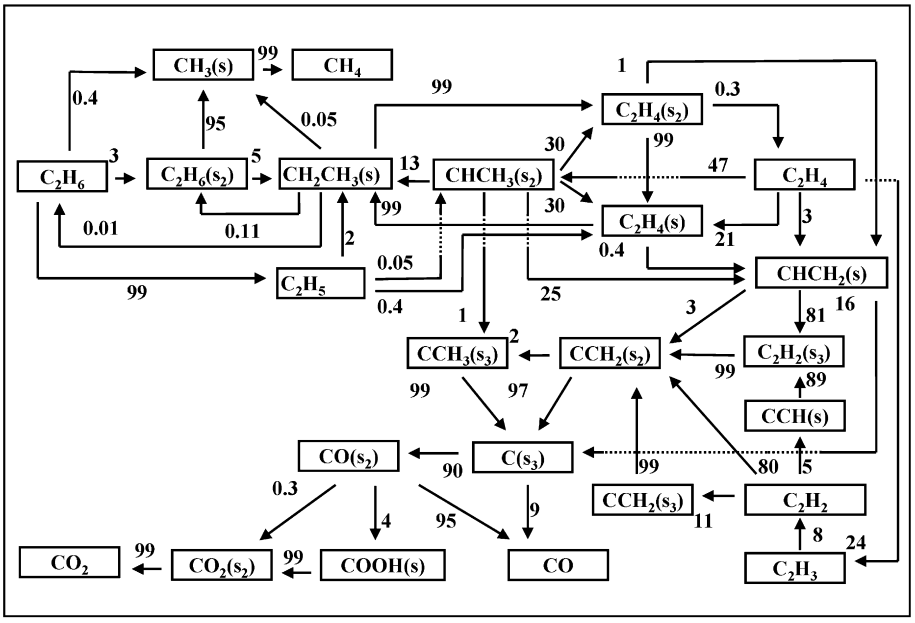

Fig. 14. Major channels in the heterogeneous reaction mechanism of ethane and ethylene on the surface at a distance of 29 mm from the entrance of the pore. Figures correspond to the cumulative absolute contribution (in percentage) of all reactions involved in the path consuming the involved species and producing the target compound.

partly via the dissociative adsorption of ethyl radicals present in the gas phase adjacent to the wall.

$$C_2H_5 + Pt(s) \rightleftarrows CH_2CH_3(s), \quad \text{(R11)}$$

$$C_2H_5 + 2Pt(s) \rightleftarrows H(s) + C_2H_4(s). \quad \text{(R13)}$$

The ethane consumption process shifts to the gas phase about 15 mm from the entrance of the pore and the catalytic consumption of C_2H_5 becomes less significant ($\leqslant$2.5%) due to the onset of gas phase reactions. The process will not be sustained by oxygen-assisted mechanisms due to the strong depletion of oxygen. Rather, the gas phase reactions will ultimately shift from oxidative dehydrogenation toward pyrolytic pathways 29 mm downstream via H (79%) and CH_3 (11%) radical attack on C_2H_6 leading to C_2H_4 via the subsequent thermal decomposition of C_2H_5. However, oxygen-assisted dehydrogenation leading to ethylene (14%) and oxidation of the vinyl radical (12%) remain major gas phase consumption channels for O_2. The reactions are important for thermal stability and for the propagation of the gas phase mechanism across the pore and also lead to oxygenated species.

8.3. Heterogeneous depletion of ethylene

Platinum has the potential to promote the formation of ethylene at the entrance of the pore, as discussed above, but also shows a subsequent propensity to consume ethylene leading to a third major catalytic mechanism. The dehydrogenation/rehydrogenation of ethylene over platinum has been the subject of extensive research. In addition to the di-σ and π forms of C_2H_4, $CH_2CH_3(s)$, $CHCH_3(s_2)$, $CCH_3(s_3)$, $CHCH_2(s)$ and $CCH_2(s_2)$ have been recurrent species used to characterize the mechanism. In the reformation of ethane from ethylene, ethylidyne has been identified by several groups [9,16–18] as a spectator. The Horiuti–Polanyi mechanism, featuring the sequential incorporation of H(s), passing via $CH_2CH_3(s)$, and leading to the direct (or indirect) release of ethane into the gas phase, has been proposed as a probable route [9,16, 96]. The current model incorporates the pathway and, as shown in Figs. 13 and 14, a large fraction of ethylene adsorbed on the surface in a π-bonded configuration is rehydrogenated to $CH_2CH_3(s)$. However, the latter species essentially dehydrogenates to di-σ ethylene, which is recycled back to the π-bonded configuration.

$$CH_2CH_3(s) + 2Pt(s) \rightleftarrows C_2H_4(s_2) + H(s), \quad \text{(R145)}$$

$$C_2H_4(s_2) \rightleftarrows C_2H_4(s) + Pt(s), \quad \text{(R167)}$$

$$C_2H_4(s) + H(s) \rightleftarrows CH_2CH_3(s) + Pt(s). \quad \text{(R149)}$$

The fast dehydrogenation/hydrogenation mechanism occurs throughout the catalyst and emphasizes the roles of both $C_2H_4(s)$ and $C_2H_4(s_2)$. The balance indicates that the catalyst may become a net producer of ethane. At a distance of 29 mm, ethane is rapidly converted homogeneously into ethylene in the proximity of the wall leading to significant adsorption on the surface. For O/C ratios higher than 0.7, sequential surface hydrogenation of ethylene passing via reactions (R149), (R126) leads to the release of ethane from the surface via associative (R10) or direct (R2) desorption.

$$CH_2CH_3(s) + H(s) + \rightleftarrows C_2H_6(s_2), \quad \text{(R126)}$$

$$CH_2CH_3(s) + H(s) \rightleftarrows C_2H_6 + 2Pt(s), \quad \text{(R10)}$$

$$C_2H_6(s_2) \rightleftarrows C_2H_6 + 2Pt(s). \quad \text{(R2)}$$

The subsequent decrease in ethylene yield is largely due to adsorption on the surface. As shown in Figs. 13 and 14, the adsorption of ethylene into ethylidene proceeds mainly via reaction (R21), which contributes up to 47%. However, toward the end of the catalyst an increasing fraction 21% leads to π-bonded $C_2H_4(s)$ via (R152).

$$C_2H_4 + 2Pt(s) \rightleftarrows CHCH_3(s_2), \quad \text{(R21)}$$

$$C_2H_4 + Pt(s) \rightleftarrows C_2H_4(s). \quad \text{(R152)}$$

The heterogeneous isomerization pathway (R21) is consistent with observations by Deng et al. [17] who, using RAIS on platinum at low temperature (around 280 K) and ultra high vacuum conditions (UHV), detected the formation of ethylidene from ethylene prior to the sequential hydrogenation into ethane. Most of the ethylidene produced on the surface will isomerize to π-bonded ethylene (30%) via reaction (R181) and to di-σ bonded ethylene (30%) via (R183), leading to the fast hydrogenation/dehydrogenation cycle mentioned above. Small amounts of $C_2H_4(s_2)$ also desorb via reactions (R165).

$$CHCH_3(s_2) \rightleftarrows C_2H_4(s) + Pt(s), \quad \text{(R181)}$$

$$CHCH_3(s_2) \rightleftarrows C_2H_4(s_2), \quad \text{(R183)}$$

$$C_2H_4(s_2) \rightleftarrows C_2H_4(s) + Pt(s), \quad \text{(R167)}$$

$$C_2H_4(s_2) \rightleftarrows C_2H_4 + 2Pt(s). \quad \text{(R165)}$$

Several dehydrogenation pathways for ethylene over platinum have been suggested whereby ethylidyne appears as an end-product prior to C–C bond scission. Windham et al. [87] proposed that ethylene first isomerizes to ethylidene, which transforms into ethylidyne via α-hydrogen elimination. The path is a major channel leading to C–C bond scission in the mechanism proposed by Zerkle et al. [26] and was further supported by Hwang et al. [113] in their reactive ion scattering experiments on a platinum crystal in UHV and temperatures ranging between 220 and 770 K. Zaera [114] proposed, based on a thermal programmed desorption on Pt(111) in UHV, the dehydrogenation of ethylene to vinyl followed by isomerization to ethylidyne. The channel was subsequently supported by Kua and Goddard [73] on the basis of the application of nonlocal density functional methods to study C_2H_x and CH_x chemisorption over Pt(111). Somorjai et al. [115] suggested, based on a study combining low-energy electron diffraction and high-resolution electron energy loss spectroscopy, that ethylene would first rehydrogenate into ethyl before dehydrogenating again into ethylidene and subsequently to ethylidyne. Kang and Anderson [116] proposed that two consecutive dehydrogenations lead to vinyl and vinylidene, which may rehydrogenate to ethylidyne.

The computed relative contributions made by the reactions steps discussed above are naturally affected by uncertainties in the determination of rate parameters, but it may be noted that for the current set of conditions the results are sensitive to all four mechanisms. The main pathways to $CHCH_2(s)$ pass via dehydrogenation of ethylene and ethylidene with (R157), (R169), (R191) contributing 19%, 55% and 19%, respectively. Adsorption from the gas phase (R196) makes a minor (5%) contribution.

$$C_2H_4 + 2Pt(s) \rightleftarrows H(s) + CHCH_2(s), \quad \text{(R196)}$$

$$C_2H_4(s) + Pt(s) \rightleftarrows H(s) + CHCH_2(s), \quad \text{(R157)}$$

$$C_2H_4(s_2) \rightleftarrows H(s) + CHCH_2(s), \quad \text{(R169)}$$

$$CHCH_3(s_2) \rightleftarrows H(s) + CHCH_2(s). \quad \text{(R191)}$$

The consecutive α-dehydrogenation steps starting with ethylene and proceeding to $CCH_2(s_2)$ via (R205) [116] contribute around 3% of the $CHCH_2(s)$ consumption. However, the major channel (81%) leads to $C_2H_2(s_3)$ via (R207) and is followed by isomerization (99%) to $CCH_2(s_2)$ via reaction (R273).

$$CHCH_2(s) + 2Pt(s) \rightleftarrows CCH_2(s_2) + H(s), \quad \text{(R205)}$$

$$CHCH_2(s) + 3Pt(s) \rightleftarrows C_2H_2(s_3) + H(s), \quad \text{(R207)}$$

$$C_2H_2(s_3) \rightleftarrows CCH_2(s_2) + Pt(s). \quad \text{(R273)}$$

The dehydrogenation of ethylidene (24%) via reaction (R189) and the recombination of vinylidene with H(s) (60%) via (R239) constitute the major channels leading to ethylidyne on the surface.

$$CHCH_3(s_2) + 2Pt(s) \rightleftarrows H(s) + CCH_3(s_3), \quad \text{(R189)}$$

$$CCH_2(s_2) + H(s) \rightleftarrows CCH_3(s_3). \quad \text{(R239)}$$

The above highlights the mechanisms proposed by Windham et al. [87] and Kang and Anderson [116]. This is partially due to the adsorption of ethylene via reaction (R21), discussed above, and the net balance indicates that 13% of $CHCH_3(s_2)$ is effectively rehydrogenated into $CH_2CH_3(s)$ via reaction (R179). However, it may be noted that the lower limit values of 29.3 and 46 kJ/mol for the heats of adsorption of π and di-σ bonded ethylene, promote the isomerization of ethylidene to ethylene and reduces the contribution of (R179) from 13% to 2%. Hence, variations in heats of adsorptions for ethylene will effect the contribution of the mechanism suggested by Somorjai et al. [115].

$$H(s) + CHCH_3(s_2) \rightleftarrows CH_2CH_3(s) + 2Pt(s). \quad \text{(R179)}$$

The implementation of the lower energy barriers, also shown in Table 5, shifts the balance toward the dehydrogenation route suggested by Zaera [114] via reactions (R21), (R191), (R194). With the alternative reaction rates, 18% of the consumption of gas phase C_2H_4 proceeds via adsorption to $C_2H_4(s)$ and 49% to $CHCH_3(s)$, before transforming to π or di-σ bonded ethylene, leading to the same fast hydrogenation/dehydrogenation cycle discussed above. A relatively small fraction of $CHCH_3(s_2)$ dehydrogenates to $CCH_3(s_3)$ via (R189) following the suggestion by Windham et al. [87]. However, up to 5% of the vinyl radicals formed via dehydrogenation of $C_2H_4(s, s_2)$ and $CHCH_3(s)$, isomerize to $CCH_3(s_3)$ via (R194), in agreement with suggestions by Zaera [114], followed partially (30%) by dehydrogenation via (R240).

$$CHCH_3(s_2) + 2Pt(s) \rightleftarrows CCH_3(s_3) + H(s), \quad \text{(R189)}$$

$$CHCH_3(s_2) \rightleftarrows CHCH_2(s) + H(s), \quad \text{(R191)}$$

$$CHCH_2(s) + 2Pt(s) \rightleftarrows CCH_3(s_3), \quad \text{(R194)}$$

$$CCH_3(s_3) \rightleftarrows CCH_2(s_2) + H(s). \quad \text{(R240)}$$

Computations using the isomerization barriers proposed by Anghel et al. [98], see above, essentially close the reverse pathway. However, the final ethylene yield remains unchanged due to the increased hydrogenation of ethylidene leading to ethyl and the fast dehydrogenation/hydrogenation sequences featuring the ethyl radical and ethylene. Anghel et al. [98,135] also suggested a barrier of 31.8 kJ/mol for the dehydrogenation of ethyl to ethylidene and a barrier of 27.9 kJ/mol for the hydrogen abstraction to ethylene. The corresponding barriers used here (113.4 kJ/mol for $CHCH_3$, 29.3 kJ/mol for $C_2H_4(s_2)$ and 37.2 kJ/mol for $C_2H_4(s)$ formation), derived using bridge configurations, yield a higher selectivity to ethylene and reduced formation of ethylidene from ethyl. The differences in the energetics partly come from the observation that the most stable adsorbates correspond to geometries which tend to open double or triple C–C bonds and complete the tetravalency of each carbon atom by involving the maximum number of platinum atoms [98,135]. Higher barriers for the dehydrogenation of ethylene impact the importance of vinyl radicals and the subsequent decomposition channels. Variations in the barriers of the hydrogen abstractions from vinyl to acetylene and vinylidene radicals do not have a large impact due to the fast isomerization of acetylene.

The above sequences define the preliminary balancing between $CCH_3(s_3)$, $CHCH_2(s)$ and $CCH_2(s_2)$ that ultimately leads to the formation of carbon on the catalyst. The breakage of the C–C bond for these precursors provides the dominant channels as shown in Fig. 14. More than 99% of $CCH_3(s_3)$ and 16% of $CHCH_2(s)$ leads to $C(s_3)$ and $CH_3(s)$ via reactions (R197), (R233), (R235). Throughout the catalyst, more than 97% of $CCH_2(s_2)$ leads to carbon via H(s) radical attack (R243). The methyl radical subsequently leads to methane via $CH_3(s)$ + H(s) recombination.

$$CHCH_2(s) + 3Pt(s) \rightleftarrows C(s_3) + CH_3(s), \quad \text{(R197)}$$

$$CCH_3(s_3) + Pt(s) \rightleftarrows C(s_3) + CH_3(s), \quad \text{(R233)}$$

$$CCH_3(s_3) + H(s) \rightleftarrows C(s_3) + CH_4 + Pt(s), \quad \text{(R235)}$$

$$CCH_2(s_2) + H(s) + Pt(s) \rightleftarrows C(s_3) + CH_3(s). \quad \text{(R243)}$$

As shown in Figs. 13 and 14, a number of reaction paths contribute to the formation of carbonaceous species on the surface. The sequential gas phase dehydrogenation of ethylene to acetylene and the subsequent dissociative adsorption, or isomerization,

of C_2H_2 on the surface, further supplements the overall production of carbon. The calculations indicate that acetylene consumption is mainly (80%) via reactions leading to $CCH_2(s_2)$ (R37) and (5%) to CCH(s) (R284). The latter species then essentially (88%) rehydrogenates to $C_2H_2(s_3)$ via (R285). A small fraction ~10% of C_2H_2 is also adsorbed on the surface via (R39) leading to $CCH_2(s_3)$, which predominantly yields $CCH_2(s_2)$ via (R261).

$$C_2H_2 + 2Pt(s) \rightleftarrows CCH_2(s_2), \quad (R37)$$

$$C_2H_2 + 2Pt(s) \rightleftarrows CCH(s) + H(s), \quad (R284)$$

$$CCH(s) + H(s) + Pt(s) \rightleftarrows C_2H_2(s_3), \quad (R285)$$

$$C_2H_2 + 3Pt(s) \rightleftarrows CCH_2(s_3), \quad (R39)$$

$$CCH_2(s_3) \rightleftarrows CCH_2(s_2) + Pt(s). \quad (R261)$$

The lower alternative energy barriers shown in Table 5 introduce acetylene as an intermediate in the isomerization of $CCH_2(s_3)$ leading to $CCH_2(s_2)$. However, the overall product yields are only marginally affected.

8.4. Heterogeneous oxidative mechanisms

Mechanisms of varying complexity describing the catalytic formation and oxidation of carbon monoxide on platinum form part of many studies (e.g., [22–24,26,32,39,93,117–121]). Results obtained here are in agreement with the work of Mhadeshwar and Vlachos [93] in that $C(s_3)$ is oxidized predominantly (99%) by OH(s) via reactions (R367), (R369). The finding is in contrast to the studies by Zerkle et al. [26] and Aghalayam et al. [22] where it was proposed that the reaction with O(s) (R363) is the major channel. The current work suggests that, when combined with the corresponding associative desorption (R361) reaction, the channel contributes less than 1% to the oxidation of surface carbon.

$$C(s_3) + O(s) \rightleftarrows CO + 4Pt(s), \quad (R361)$$

$$C(s_3) + O(s) \rightleftarrows CO(s_2) + 2Pt(s), \quad (R363)$$

$$C(s_3) + OH(s) \rightleftarrows CO + H(s) + 3Pt(s), \quad (R367)$$

$$C(s_3) + OH(s) \rightleftarrows CO(s_2) + H(s) + Pt(s). \quad (R369)$$

Overall, the catalytic oxidative channels are limited upstream due to the preferential oxidation of hydrogen. At a distance of 5 mm from the entrance of the pore, almost all OH(s) (99%) will associate with H(s) leading to $H_2O(s)$ and subsequent desorption. However, further downstream, up to 17% of OH(s), is consistently used to oxidize surface carbon ((R367), (R369)) with $CO(s_2)$ predominantly (95%) undergoing direct desorption (R377). The mechanism partially explains the rise in the catalytic production of CO. The oxidation of hydrogen is the major source of OH(s) throughout the first half of the catalytic section of the pore. However, further downstream OH(s) also originates (~42%) from dissociation reactions on the surface ((R503), (R551)). Consequently, it appears probable that high concentrations of steam close to the wall will limit the formation of carbon on the catalyst [132–134].

$$H_2O + H(s) + Pt(s) \rightleftarrows H_2(s) + OH(s), \quad (R503)$$

$$H_2O(s) + H(s) \rightleftarrows H_2(s) + OH(s). \quad (R551)$$

Carbon monoxide not only originates from the oxidation of carbon atoms. The formation of oxygenated species (e.g., methanol, formaldehyde and formyl radicals) in the gas phase also contributes further downstream. Toward the exit of the catalyst, around 24% of ethylene consumption leads to C_2H_3 following H and OH radical attack. Although a small fraction (5%) is rehydrogenated, vinyl radicals are predominantly oxidized to CH_2O (32%), CH_2CHO (50%) and CH_3CO (4%) and, subsequently, through multiple channels to CH_3 and CO in the gas phase. Apart from attacking ethane, as mentioned previously, methyl radicals (65%) are also oxidized to CH_3O, which leads either to formaldehyde or, via H radical recombination, to methanol. Once produced in the gas-phase, CH_3OH consumption passes predominantly (91%) via molecular adsorption leading to C–O bond scission via H attack. Sequential dehydrogenation provide complimentary pathways. Kua and Goddard [39] and Ishikawa et al. [117] proposed that dehydrogenation proceeds via hydroxymethyl ($CH_2OH(s)$) and hydroxymethylidene ($CHOH(s_2)$) before leading to the formyl radical (CHO(s)) and finally $CO(s_2)$. Kandoi et al. [118] suggested that $CHOH(s_2)$ decomposes directly into adsorbed $CO(s_2)$ via the simultaneous removal of the two hydrogen atoms. The latter channel is not included as a global step in the current mechanism. However, the sequential pathway is present. Alternatively, Mhadeshwar and Vlachos [93] and Desai et al. [119] suggested that $CH_2O(s)$ is formed by thermal decomposition of $CH_2OH(s)$ leading subsequently to $CO(s_2)$ via CHO(s). The pathway is directly analogous to the gas phase reaction channels and is included in the catalytic chemistry of formaldehyde.

Hydroxymethyl reforms methanol (52%) and decomposes (19%) to $CH_3(s)$ + OH(s) as well as leading (11%) to CHOH(s). A fraction (14%) desorbs to CH_2O or (3%) forms $CH_2O(s)$ via H(s) attack. However, the reactions are minor compared to the gas-phase oxidation of vinyl radicals and the thermal decomposition of the methoxy radical, which contribute 30% and 62% of CH_2O formation. The latter species initiates a significant CO formation channel. The adsorption of CH_2O leads (19%) to CHO(s) via (R83) and (66%) to $CH_2O(s)$ via (R442), with $CH_2O(s)$ dehydrogenating predominantly into CHO(s) (82%) via thermal decomposition (R443) and (27%) via H(s) attack with reaction (R445).

$$CH_2O + 2Pt(s) = H(s) + CHO(s), \quad (R83)$$

$$CH_2O + Pt(s) = CH_2O(s), \quad (R442)$$

$$CH_2O(s) + Pt(s) = CHO(s) + H(s), \quad (R443)$$

$$CH_2O(s) + H(s) = CHO(s) + H_2(s). \quad (R445)$$

Formyl radicals terminate the sequence by dehydrogenating (91%) via reaction (R461) or (8%) reacting with H(s) via reaction (R465).

$$CHO(s) + 2Pt(s) = CO(s_2) + H(s), \quad (R461)$$

$$CHO(s) + H(s) = CO(s_2) + H_2(s). \quad (R465)$$

The reaction of CO(s) with O(s), leading to $CO_2(s_2)$, is often considered the final pathway for the oxidative channel. This is the case in several studies of the catalytic oxidation of methane and ethane (e.g., [26,28,93,121]) over noble metals and CO oxidation on platinum. However, along with several recent studies (e.g., [24,39,117]) the current work has identified the carboxyl radical as a key intermediate prior to the formation of carbon dioxide. In the current simulations, up to 4% of $CO(s_2)$ will combine with OH(s) to form COOH(s) via reaction (R389). The latter then turns directly into carbon dioxide $CO_2(s)$ via reaction (R475) and subsequently desorbs via (R393).

$$CO(s_2) + OH(s) \rightleftarrows COOH(s) + 2Pt(s), \quad (R389)$$

$$COOH(s) + 2Pt(s) \rightleftarrows CO_2(s_2) + H(s), \quad (R475)$$

$$CO_2(s_2) \rightleftarrows CO_2 + 2Pt(s). \quad (R393)$$

The current work does not suggest a strong sensitivity to the direct oxidation of $CO(s_2)$ with O(s) via (R379). However, the recombination with OH(s) via reaction (R383) does contribute 7% to the production of $CO_2(s_2)$ and further emphasizes the importance of OH(s).

$$CO(s_2) + O(s) \rightleftarrows CO_2(s_2) + Pt(s), \quad (R379)$$

$$CO(s_2) + OH(s) \rightleftarrows CO_2(s_2) + H(s). \quad (R383)$$

9. Conclusions

The conversion of ethane in short contact time reactors with a platinum washcoated catalyst has been studied experimentally and computationally. Comprehensive detailed chemical kinetics was applied for the gas phase and the heterogeneous chemistry was derived on the basis of four reaction classes providing an extensive set of (quasi-)elementary heterogeneous reactions. The properties of individual reaction steps were estimated using collision theory, a transition state approach, the UBI–QEP method and data derived from DFT and experimental studies. The current reaction class based approach for the generation of the chemistry is naturally subject to uncertainties in input parameters such as heats of adsorption and pre-exponential factors. The impact of temperature on micro-pore diffusion limitations may also alter the balance of reaction pathways. However, a relatively good agreement between experimental data and computational predictions has been shown. It was found that the major pathways on the surface under the current conditions lead to rehydrogenation/dehydrogenation sequences via $C_2H_6(s_2)$, $CH_2CH_3(s)$, $C_2H_4(s)$ and $C_2H_4(s_2)$ and that the whole process is made possible by the rapid catalytic consumption of oxygen from the very entrance of the pore leading to the preferential oxidation of hydrogen and the release of heat in the proximity of the surface. The released heat is the key driver in the initiation of gas phase reactions, which start in the vicinity of the wall and then propagate toward the center of the pore. As the inlet velocity is increased, the consumption of oxygen still starts at the pore entrance whereas C_2H_6 penetrates deeper in the pore before the homogeneous processes ignite. Some of the ethylene produced in the gas phase after ignition will tend to be adsorbed back onto the surface and a fraction will undergo C–C bond scission releasing methane back in the gas phase while depositing carbon atoms on the surface. The consumption of ethylene on the surface is of sufficient importance to influence selectivities at higher platinum loading and longer residence times. A sensitivity analysis has also shown that results are affected by the heats of absorption of selected CH_xCH_y species with higher values tending to reduce the selectivity to ethylene. The oxidation of carbon on the surface was shown to predominantly lead to $CO(s_2)$, via reaction with the OH(s) radical, and with CO_2 formation passing via COOH(s). Interactions of gas phase molecules with adsorbates occur throughout the catalytic section. However, the reaction class contributes to a smaller extent than the main pathways. Nevertheless, the simulations indicate, for example, that at the entrance of the pore around 14% of the consumed molecular oxygen interacts with H(s) leading to O(s) and OH(s). It has also been shown that the derived model has the ability to reproduce reaction dynamics with reasonable quantitative accuracy. Several catalytic pathways have been identified as candidates for more detailed investigations. These include energy barriers for isomerization reactions, such as $C_2H_4(s_2)$ leading to $CHCH_3(s_2)$. While the impact of uncertainties on product selectivities is not large under the current conditions, changes in energy barriers impact the preferred reaction routes on the surface. Despite such uncertainties it is evident that the current approach, combined with the UBI–QEP method, can capture all experimentally observed qualitative trends with reasonable quantitative accuracy for a comparatively wide range of experimental conditions. It is also evident that more accurate determinations of heats of adsorption have the potential to improve the quantitative agreement with experimental data, as shown by the application of a hybrid UBI–QEP–DFT based model.

Acknowledgments

R.P. Lindstedt, R.S. Vincent and N.A. Malik wish to thank Ineos Technologies Ltd for financial support. The Gaussian 03 calculations were performed by R.K. Robinson and the authors wish express their gratitude for making the results available.

Appendix A. The surface chemistry

Table 7
Major heterogeneous reactions involved in the partial oxidation of ethane over platinum (the indices f. and r. stand for forward and reverse rate, respectively).

No.	Reaction		Rate coefficients in the form $k_m = AT^\beta \exp(-\Delta E/RT)$		
			A[a]	β	ΔE[b]
1	$C_2H_6 + 2Pt(s) \Leftrightarrow C_2H_6(s_2)$	f.	9.02E+02	0.5	0
		r.	2.08E+10	1	36.1
3	$C_2H_6 + O(s) + Pt(s) \Leftrightarrow CH_2CH_3(s) + OH(s)$	f.	3.66E+03	0.5	0
		r.	1.39E+11[c]	0.5	70.4
5	$C_2H_6 + OH(s) + Pt(s) \Leftrightarrow CH_2CH_3(s) + H_2O(s)$	f.	4.35E+03	0.5	13.8
		r.	1.40E+11[c]	0.5	53.8
7	$C_2H_6 + 2Pt(s) \Leftrightarrow CH_3(s) + CH_3(s)$	f.	9.02E+02	0.5	50.2
		r.	1.65E+11[c]	0.5	19.1
9	$C_2H_6 + 2Pt(s) \Leftrightarrow CH_2CH_3(s) + H(s)$	f.	9.02E+02	0.5	27.7
		r.	4.19E+11[c]	0.5	35.6
11	$C_2H_5 + Pt(s) \Leftrightarrow CH_2CH_3(s)$	f.	2.45E+05	0.5	0
		r.	2.08E+10	1	162.8
13	$C_2H_5 + 2Pt(s) \Leftrightarrow C_2H_4(s) + H(s)$	f.	6.12E+04	0.5	0
		r.	4.12E+11[c]	0.5	164.3
15	$C_2H_5 + 3Pt(s) \Leftrightarrow C_2H_4(s_2) + H(s)$	f.	9.07E+03	0.5	0
		r.	4.12E+11[c]	0.5	195.3
17	$C_2H_5 + 3Pt(s) \Leftrightarrow CH_2(s_2) + CH_3(s)$	f.	9.07E+03	0.5	0
		r.	1.66E+11[c]	0.5	22.3
19	$C_2H_5 + H(s) + 2Pt(s) \Leftrightarrow CHCH_3(s_2) + H_2(s)$	f.	4.34E+04	0.5	0
		r.	3.03E+11[c]	0.5	19.7
21	$C_2H_4 + 2Pt(s) \Leftrightarrow CHCH_3(s_2)$	f.	9.35E+02	0.5	0
		r.	2.08E+10	1	294.4
23	$C_2H_3 + 3Pt(s) \Leftrightarrow CCH_3(s_3)$	f.	9.42E+03	0.5	0
		r.	2.08E+10	1	404.4
25	$C_2H_3 + Pt(s) \Leftrightarrow CHCH_2(s)$	f.	2.54E+05	0.5	0
		r.	2.08E+10	1	183.9
27	$C_2H_3 + 3Pt(s) \Leftrightarrow CHCH_2(s_3)$	f.	9.42E+03	0.5	0
		r.	2.08E+10	1	129

(*continued on next page*)

Table 7 (*continued*)

No.	Reaction		Rate coefficients in the form $k_m = AT^{\beta}\exp(-\Delta E/RT)$		
			A[a]	β	ΔE[b]
29	$C_2H_3 + 3Pt(s) \Leftrightarrow CCH_2(s_2) + H(s)$	f.	9.42E+03	0.5	0
		r.	4.04E+11[c]	0.5	224.5
31	$C_2H_3 + 4Pt(s) \Leftrightarrow C_2H_2(s_3) + H(s)$	f.	9.93E+02	0.5	0
		r.	4.00E+11[c]	0.5	243.8
33	$C_2H_3 + 4Pt(s) \Leftrightarrow C(s_3) + CH_3(s)$	f.	9.93E+02	0.5	0
		r.	1.69E+11[c]	0.5	227
35	$C_2H_3 + 5Pt(s) \Leftrightarrow CH(s_3) + CH_2(s_2)$	f.	8.14E+01	0.5	0
		r.	1.69E+11[c]	0.5	36
37	$C_2H_2 + 2Pt(s) \Leftrightarrow CCH_2(s_2)$	f.	3.24E+03	0.5	0
		r.	2.08E+10	1	299
39	$C_2H_2 + 3Pt(s) \Leftrightarrow CCH_2(s_3)$	f.	4.81E+02	0.5	0
		r.	2.08E+10	1	149
41	$CH_3 + Pt(s) \Leftrightarrow CH_3(s)$	f.	3.40E+05	0.5	0
		r.	2.08E+10	1	159.1
43	$CH_3 + 3Pt(s) \Leftrightarrow CH_2(s_2) + H(s)$	f.	1.26E+04	0.5	0
		r.	3.76E+11[c]	0.5	74.1
45	$CH_2(T) + 2Pt(s) \Leftrightarrow CH_2(s_2)$	f.	8.82E+04	0.5	0
		r.	2.08E+10	1	283.4
47	$CH_2(T) + 4Pt(s) \Leftrightarrow CH(s_3) + H(s)$	f.	1.38E+03	0.5	0
		r.	3.70E+11[c]	0.5	240.3
49	$CH + 3Pt(s) \Leftrightarrow CH(s_3)$	f.	1.36E+04	0.5	0
		r.	2.08E+10	1	407.8
51	$CH + 4Pt(s) \Leftrightarrow C(s_3) + H(s)$	f.	1.43E+03	0.5	0
		r.	3.65E+11[c]	0.5	544.3
53	$C_1 + 3Pt(s) \Leftrightarrow C(s_3)$	f.	1.42E+04	0.5	0
		r.	2.08E+10	1	628
55	$CO + O(s) + Pt(s) \Leftrightarrow CO_2(s_2)$	f.	2.14E+05	0.5	97.3
		r.	2.08E+10	1	288.2
57	$CO + OH(s) + 2Pt(s) \Leftrightarrow CO_2(s_2) + H(s)$	f.	6.35E+04	0.5	86.8
		r.	3.80E+11[c]	0.5	215.2
59	$CO + CH_2O(s) + Pt(s) \Leftrightarrow CHO(s) + CHO(s)$	f.	4.34E+05	0.5	5.6
		r.	1.22E+11[c]	0.5	20
61	$CO + CH_2O(s) + 3Pt(s) \Leftrightarrow CH_2(s_2) + CO_2(s_2)$	f.	1.61E+04	0.5	0
		r.	1.40E+11[c]	0.5	34.1
63	$C_2H_6(s_2) + CO \Leftrightarrow CH_2CH_3(s) + CHO(s)$	f.	5.89E+05	0.5	45.4
		r.	1.32E+11[c]	0.5	19.8
65	$CO + H_2O(s) + Pt(s) \Leftrightarrow CHO(s) + OH(s)$	f.	2.94E+05	0.5	49.3
		r.	1.27E+11[c]	0.5	23.9
67	$CH_2CH_3(s) + CO + 2Pt(s) \Leftrightarrow C_2H_4(s_2) + CHO(s)$	f.	1.39E+05	0.5	0
		r.	1.31E+11[c]	0.5	15.4
69	$CHCH_3(s_2) + CO + 2Pt(s) \Leftrightarrow CCH_3(s_3) + CHO(s)$	f.	1.37E+05	0.5	16.9
		r.	1.32E+11[c]	0.5	28.4
71	$CO + CH_3OH(s) + Pt(s) \Leftrightarrow CHO(s) + CH_2OH(s)$	f.	4.95E+05	0.5	47.8
		r.	1.24E+11[c]	0.5	19.6
73	$CH_2CH_3(s) + CO + Pt(s) \Leftrightarrow C_2H_4(s) + CHO(s)$	f.	5.57E+05	0.5	15.6
		r.	1.31E+11[c]	0.5	11.6
75	$CO + OH(s) + Pt(s) \Leftrightarrow CHO(s) + O(s)$	f.	2.54E+05	0.5	79.7
		r.	1.25E+11[c]	0.5	27.3
77	$CO_2 + C(s_3) + Pt(s) \Leftrightarrow CO(s_2) + CO(s_2)$	f.	1.59E+03	0.5	0
		r.	1.21E+11[c]	0.5	183.9
79	$CH_2O + O(s) + Pt(s) \Leftrightarrow CHO(s) + OH(s)$	f.	2.41E+04	0.5	0
		r.	1.27E+11[c]	0.5	120.7
81	$CH_2O + OH(s) + Pt(s) \Leftrightarrow CHO(s) + H_2O(s)$	f.	2.86E+04	0.5	0
		r.	1.29E+11[c]	0.5	90.3
83	$CH_2O + 2Pt(s) \Leftrightarrow CHO(s) + H(s)$	f.	5.94E+03	0.5	0
		r.	3.78E+11[c]	0.5	58.2
85	$CHO + Pt(s) \Leftrightarrow CHO(s)$	f.	2.46E+05	0.5	0
		r.	2.08E+10	1	167.1
87	$CHO + 3Pt(s) \Leftrightarrow CO(s_2) + H(s)$	f.	9.12E+03	0.5	0
		r.	3.74E+11[c]	0.5	318
89	$CHO + H(s) + 2Pt(s) \Leftrightarrow CO(s_2) + H_2(s)$	f.	4.37E+04	0.5	1.5
		r.	2.73E+11[c]	0.5	266.5
91	$CH_3OH + Pt(s) \Leftrightarrow CH_3OH(s)$	f.	2.34E+05	0.5	0
		r.	2.08E+10	1	44.1
93	$CH_3OH + O(s) + Pt(s) \Leftrightarrow CH_2OH(s) + OH(s)$	f.	2.37E+05	0.5	3.7
		r.	1.30E+11[c]	0.5	79.6
95	$CH_3OH + O(s) + Pt(s) \Leftrightarrow CH_3O(s) + OH(s)$	f.	2.37E+05	0.5	1.1
		r.	1.29E+11[c]	0.5	56.4
97	$CH_3O + Pt(s) \Leftrightarrow CH_3O(s)$	f.	2.38E+05	0.5	0
		r.	2.08E+10	1	172.8
99	$CH_3O + 2Pt(s) \Leftrightarrow CH_3(s) + O(s)$	f.	5.94E+04	0.5	0
		r.	1.42E+11[c]	0.5	138.2
101	$CH_3O + 2Pt(s) \Leftrightarrow CH_2O(s) + H(s)$	f.	5.94E+04	0.5	0
		r.	3.87E+11[c]	0.5	210

Table 7 (*continued*)

No.	Reaction		Rate coefficients in the form $k_m = AT^{\beta}\exp(-\Delta E/RT)$		
			A[a]	β	ΔE[b]
103	$CH_3O + CO(s_2) \Leftrightarrow CHO(s) + CH_2O(s)$	f.	4.37E+05	0.5	0
		r.	1.23E+11[c]	0.5	59
105	$CH_3O + H(s) \Leftrightarrow CH_3OH(s)$	f.	1.69E+05	0.5	25.9
		r.	2.08E+10	1	250
107	$C_2H + Pt(s) \Leftrightarrow CCH(s)$	f.	2.65E+05	0.5	0
		r.	2.08E+10	1	287.2
109	$C_2 + 6Pt(s) \Leftrightarrow C(s_3) + C(s_3)$	f.	5.81E+00	0.5	0
		r.	1.72E+11[c]	0.5	644.8
111	$C_2H_6(s_2) \Leftrightarrow CH_3(s) + CH_3(s)$	f.	2.08E+10	1	86.4
		r.	1.65E+11[c]	0.5	19.1
113	$C_2H_6(s_2) + H(s) \Leftrightarrow CH_2CH_3(s) + H_2(s) + Pt(s)$	f.	4.27E+11[c]	0.5	81.3
		r.	3.04E+11[c]	0.5	5.5
115	$C_2H_6(s_2) + H(s) \Leftrightarrow CH_4 + CH_3(s) + 2Pt(s)$	f.	4.27E+11[c]	0.5	61.3
		r.	3.03E+04	0.5	0
117	$C_2H_6(s_2) + O(s) \Leftrightarrow C_2H_5 + OH(s) + 2Pt(s)$	f.	1.39E+11[c]	0.5	128.5
		r.	7.38E+04	0.5	0
119	$C_2H_6(s_2) + O(s) \Leftrightarrow CH_2CH_3(s) + OH(s) + Pt(s)$	f.	1.39E+11[c]	0.5	7.9
		r.	1.39E+11[c]	0.5	34.2
121	$C_2H_6(s_2) + OH(s) \Leftrightarrow CH_2CH_3(s) + H_2O(s) + Pt(s)$	f.	1.40E+11[c]	0.5	11.6
		r.	1.40E+11[c]	0.5	14.6
123	$C_2H_6(s_2) + CH_3(s) \Leftrightarrow CH_2CH_3(s) + CH_4 + 2Pt(s)$	f.	1.59E+11[c]	0.5	5.9
		r.	4.34E+04	0.5	0.6
125	$C_2H_6(s_2) \Leftrightarrow CH_2CH_3(s) + H(s)$	f.	2.08E+10	1	63.8
		r.	4.19E+11[c]	0.5	35.6
127	$C_2H_6(s_2) + O(s) \Leftrightarrow CH_3(s) + CH_3O(s) + Pt(s)$	f.	1.39E+11[c]	0.5	51.7
		r.	1.48E+11[c]	0.5	19.9
129	$C_2H_6(s_2) + OH(s) \Leftrightarrow CH_2CH_3(s) + H_2O + 2Pt(s)$	f.	1.40E+11[c]	0.5	36.4
		r.	1.54E+05	0.5	0
131	$CH_2CH_3(s) \Leftrightarrow C_2H_4 + H(s)$	f.	2.08E+10	1	118.4
		r.	2.65E+03	0.5	51.9
133	$CH_2CH_3(s) + H(s) \Leftrightarrow CH_3(s) + CH_3(s)$	f.	4.19E+11[c]	0.5	78.8
		r.	1.65E+11[c]	0.5	20.7
135	$CH_2CH_3(s) + O(s) \Leftrightarrow C_2H_4 + OH(s) + Pt(s)$	f.	1.37E+11[c]	0.5	22.4
		r.	4.51E+03	0.5	4.4
137	$CH_2CH_3(s) + O(s) \Leftrightarrow C_2H_4(s) + OH(s)$	f.	1.37E+11[c]	0.5	25.4
		r.	1.38E+11[c]	0.5	87.9
139	$CH_2CH_3(s) + O(s) + Pt(s) \Leftrightarrow C_2H_4(s_2) + OH(s)$	f.	1.37E+11[c]	0.5	22.4
		r.	1.38E+11[c]	0.5	103.4
141	$CH_2CH_3(s) + O(s) \Leftrightarrow CH_3(s) + CH_2O(s)$	f.	1.37E+11[c]	0.5	49
		r.	1.47E+11[c]	0.5	62.7
143	$CH_2CH_3(s) + OH(s) + Pt(s) \Leftrightarrow C_2H_4(s_2) + H_2O(s)$	f.	1.39E+11[c]	0.5	20.7
		r.	1.39E+11[c]	0.5	81.4
145	$CH_2CH_3(s) + 2Pt(s) \Leftrightarrow C_2H_4(s_2) + H(s)$	f.	8.92E+10[c]	0.5	19.5
		r.	4.12E+11[c]	0.5	51.9
147	$CH_2CH_3(s) + H(s) + Pt(s) \Leftrightarrow C_2H_4(s_2) + H_2(s)$	f.	4.19E+11[c]	0.5	59.9
		r.	3.00E+11[c]	0.5	39.5
149	$C_2H_4(s) + H(s) \Leftrightarrow CH_2CH_3(s) + Pt(s)$	f.	4.12E+11[c]	0.5	22.9
		r.	8.92E+10[c]	0.5	26.1
151	$C_2H_4(s) \Leftrightarrow C_2H_4 + Pt(s)$	f.	2.08E+10	1	68
		r.	3.74E+03	0.5	0
153	$C_2H_4(s) + O(s) + Pt(s) \Leftrightarrow CH_2(s_2) + CH_2O(s)$	f.	1.36E+11[c]	0.5	72.8
		r.	1.49E+11[c]	0.5	9.6
155	$C_2H_4(s) + OH(s) \Leftrightarrow CH_3(s) + CH_2O(s)$	f.	1.38E+11[c]	0.5	51.8
		r.	1.47E+11[c]	0.5	7.6
157	$C_2H_4(s) + Pt(s) \Leftrightarrow CHCH_2(s) + H(s)$	f.	8.95E+10[c]	0.5	100.6
		r.	4.08E+11[c]	0.5	21.8
159	$C_2H_4(s) + 3Pt(s) \Leftrightarrow CHCH_2(s_3) + H(s)$	f.	8.95E+10[c]	0.5	149.2
		r.	4.08E+11[c]	0.5	20.6
161	$C_2H_4(s) + OH(s) \Leftrightarrow CHCH_2(s) + H_2O(s)$	f.	1.38E+11[c]	0.5	62.2
		r.	1.39E+11[c]	0.5	7.9
163	$C_2H_4(s_2) + H_2O \Leftrightarrow CH_2CH_3(s) + OH(s)$	f.	5.84E+05	0.5	41.2
		r.	1.39E+11[c]	0.5	20.7
165	$C_2H_4(s_2) \Leftrightarrow C_2H_4 + 2Pt(s)$	f.	2.08E+10	1	99
		r.	9.35E+02	0.5	0
167	$C_2H_4(s_2) \Leftrightarrow C_2H_4(s) + Pt(s)$	f.	2.08E+10	1	31
		r.	8.95E+10[c]	0.5	0
169	$C_2H_4(s_2) \Leftrightarrow CHCH_2(s) + H(s)$	f.	2.08E+10	1	125.3
		r.	4.08E+11[c]	0.5	25.7
171	$C_2H_4(s_2) + O(s) \Leftrightarrow CH_2(s_2) + CH_2O(s)$	f.	1.36E+11[c]	0.5	103.8
		r.	1.49E+11[c]	0.5	9.6
173	$C_2H_4(s_2) + OH(s) \Leftrightarrow CH_3(s) + CH_2O(s) + Pt(s)$	f.	1.38E+11[c]	0.5	81.4
		r.	1.47E+11[c]	0.5	8.7
175	$C_2H_4(s_2) + 2Pt(s) \Leftrightarrow CHCH_2(s_3) + H(s)$	f.	8.95E+10[c]	0.5	180.2
		r.	4.08E+11[c]	0.5	20.6

(*continued on next page*)

Table 7 (*continued*)

No.	Reaction		Rate coefficients in the form $k_m = AT^{\beta}\exp(-\Delta E/RT)$		
			A[a]	β	ΔE[b]
177	$CHCH_3(s_2) + H(s) \Leftrightarrow C_2H_5 + 3Pt(s)$	f.	4.17E+11[c]	0.5	72.7
		r.	9.07E+03	0.5	0
179	$CHCH_3(s_2) + H(s) \Leftrightarrow CH_2CH_3(s) + 2Pt(s)$	f.	4.17E+11[c]	0.5	28.9
		r.	8.92E+10[c]	0.5	113.4
181	$CHCH_3(s_2) \Leftrightarrow C_2H_4(s) + Pt(s)$	f.	2.08E+10	1	53
		r.	8.95E+10[c]	0.5	144.9
183	$CHCH_3(s_2) \Leftrightarrow C_2H_4(s_2)$	f.	2.08E+10	1	53.2
		r.	2.08E+10	1	176.2
185	$CHCH_3(s_2) + 2Pt(s) \Leftrightarrow CHCH_2(s_3) + H(s)$	f.	9.04E+10[c]	0.5	71.7
		r.	4.08E+11[c]	0.5	17.9
187	$CHCH_3(s_2) + H(s) + Pt(s) \Leftrightarrow CCH_3(s_3) + H_2(s)$	f.	4.17E+11[c]	0.5	94.7
		r.	3.00E+11[c]	0.5	37.5
189	$CHCH_3(s_2) + 2Pt(s) \Leftrightarrow CCH_3(s_3) + H(s)$	f.	9.04E+10[c]	0.5	78.1
		r.	4.12E+11[c]	0.5	78.4
191	$CHCH_3(s_2) \Leftrightarrow CHCH_2(s) + H(s)$	f.	2.08E+10	1	54.8
		r.	4.08E+11[c]	0.5	52.1
193	$CCH_3(s_3) \Leftrightarrow CHCH_2(s) + 2Pt(s)$	f.	2.08E+10	1	119.2
		r.	9.05E+10[c]	0.5	116.8
195	$CHCH_2(s) + H(s) \Leftrightarrow C_2H_4 + 2Pt(s)$	f.	4.08E+11[c]	0.5	25.7
		r.	9.35E+02	0.5	26.3
197	$CHCH_2(s) + 3Pt(s) \Leftrightarrow C(s_3) + CH_3(s)$	f.	9.05E+10[c]	0.5	41.9
		r.	1.69E+11[c]	0.5	85
199	$CHCH_2(s) + H(s) + Pt(s) \Leftrightarrow CCH_2(s_2) + H_2(s)$	f.	4.08E+11[c]	0.5	59.6
		r.	2.95E+11[c]	0.5	47.3
201	$CHCH_2(s) + O(s) \Leftrightarrow C_2H_2 + OH(s) + Pt(s)$	f.	1.35E+11[c]	0.5	24.1
		r.	1.56E+04	0.5	0
203	$CHCH_2(s) + OH(s) \Leftrightarrow C_2H_2 + H_2O(s) + Pt(s)$	f.	1.37E+11[c]	0.5	42
		r.	1.81E+04	0.5	0
205	$CHCH_2(s) + 2Pt(s) \Leftrightarrow CCH_2(s_2) + H(s)$	f.	9.05E+10[c]	0.5	48.6
		r.	4.04E+11[c]	0.5	89.2
207	$CHCH_2(s) + 3Pt(s) \Leftrightarrow C_2H_2(s_3) + H(s)$	f.	9.05E+10[c]	0.5	18.9
		r.	4.00E+11[c]	0.5	73.9
209	$CHCH_2(s) + H(s) \Leftrightarrow C_2H_2 + H_2(s) + Pt(s)$	f.	4.08E+11[c]	0.5	127.1
		r.	1.17E+04	0.5	0
211	$CHCH_2(s) + 3Pt(s) \Leftrightarrow CCH_2(s_3) + H(s)$	f.	9.05E+10[c]	0.5	109.4
		r.	4.04E+11[c]	0.5	22.6
213	$CHCH_2(s_3) + H(s) \Leftrightarrow C_2H_4 + 4Pt(s)$	f.	4.08E+11[c]	0.5	20.6
		r.	1.46E+01	0.5	81.2
215	$CHCH_2(s_3) \Leftrightarrow CHCH_2(s) + 2Pt(s)$	f.	2.08E+10	1	0
		r.	9.05E+10[c]	0.5	54.9
217	$CHCH_2(s_3) \Leftrightarrow CCH_3(s_3)$	f.	2.08E+10	1	21
		r.	2.08E+10	1	78
219	$CHCH_2(s_3) \Leftrightarrow CCH_2(s_2) + H(s)$	f.	2.08E+10	1	21.1
		r.	4.04E+11[c]	0.5	116.6
221	$CHCH_2(s_3) + Pt(s) \Leftrightarrow C(s_3) + CH_3(s)$	f.	9.05E+10[c]	0.5	15
		r.	1.69E+11[c]	0.5	112.5
223	$CHCH_2(s_3) + H(s) \Leftrightarrow C_2H_2 + H_2(s) + 3Pt(s)$	f.	4.08E+11[c]	0.5	72.2
		r.	4.33E+02	0.5	0
225	$CHCH_2(s_3) + H(s) \Leftrightarrow C_2H_2(s_3) + H_2(s)$	f.	4.08E+11[c]	0.5	17.4
		r.	2.92E+11[c]	0.5	73.7
227	$CHCH_2(s_3) + H(s) \Leftrightarrow CCH_2(s_2) + H_2(s) + Pt(s)$	f.	4.08E+11[c]	0.5	21.1
		r.	2.95E+11[c]	0.5	64.1
229	$CHCH_2(s_3) + H(s) \Leftrightarrow CCH_2(s_2) + H_2 + 2Pt(s)$	f.	4.08E+11[c]	0.5	21.1
		r.	2.45E+04	0.5	37.3
231	$CHCH_2(s_3) + H(s) \Leftrightarrow C_2H_2(s_3) + H_2 + Pt(s)$	f.	4.08E+11[c]	0.5	17.4
		r.	9.44E+04	0.5	46.9
233	$CCH_3(s_3) + Pt(s) \Leftrightarrow C(s_3) + CH_3(s)$	f.	9.12E+10[c]	0.5	46.1
		r.	1.69E+11[c]	0.5	83.5
235	$CCH_3(s_3) + H(s) \Leftrightarrow CH_4 + C(s_3) + Pt(s)$	f.	4.12E+11[c]	0.5	35.5
		r.	1.04E+05	0.5	98.3
237	$CCH_3(s_3) + H(s) \Leftrightarrow CCH_2(s_2) + H_2(s) + Pt(s)$	f.	4.12E+11[c]	0.5	85.9
		r.	2.95E+11[c]	0.5	70.6
239	$CCH_2(s_2) + H(s) \Leftrightarrow CCH_3(s_3)$	f.	4.04E+11[c]	0.5	87.7
		r.	2.08E+10	1	50
241	$CCH_2(s_2) \Leftrightarrow CCH(s) + H(s)$	f.	2.08E+10	1	132.1
		r.	3.96E+11[c]	0.5	29.9
243	$CCH_2(s_2) + H(s) + Pt(s) \Leftrightarrow C(s_3) + CH_3(s)$	f.	4.04E+11[c]	0.5	62.2
		r.	1.69E+11[c]	0.5	53.7
245	$CCH_2(s_2) + O(s) + Pt(s) \Leftrightarrow CH_2(s_2) + CO(s_2)$	f.	1.35E+11[c]	0.5	33.2
		r.	1.47E+11[c]	0.5	152.9
247	$CCH_2(s_2) + O(s) \Leftrightarrow CCH(s) + OH(s) + Pt(s)$	f.	1.35E+11[c]	0.5	114.5
		r.	1.36E+11[c]	0.5	48
249	$CCH_2(s_2) + O(s) + Pt(s) \Leftrightarrow C(s_3) + CH_2O(s)$	f.	1.35E+11[c]	0.5	44.1
		r.	1.54E+11[c]	0.5	118.4

Table 7 (*continued*)

No.	Reaction		Rate coefficients in the form $k_m = AT^{\beta}\exp(-\Delta E/RT)$		
			A[a]	β	ΔE[b]
251	$CCH_2(s_2) + O(s) \Leftrightarrow CO + CH_2(s_2) + Pt(s)$	f.	1.35E+11[c]	0.5	33.2
		r.	3.74E+05	0.5	19.1
253	$CCH_2(s_2) + O(s) \Leftrightarrow CH_2O + C(s_3)$	f.	1.35E+11[c]	0.5	44.1
		r.	3.77E+04	0.5	71.7
255	$CCH_2(s_2) + OH(s) + Pt(s) \Leftrightarrow C(s_3) + CH_2OH(s)$	f.	1.37E+11[c]	0.5	66.1
		r.	1.56E+11[c]	0.5	51.1
257	$CCH_2(s_2) + 3Pt(s) \Leftrightarrow C(s_3) + CH_2(s_2)$	f.	9.15E+10[c]	0.5	138.9
		r.	1.70E+11[c]	0.5	52.1
259	$CCH_2(s_3) + H(s) \Leftrightarrow C_2H_3 + 4Pt(s)$	f.	4.04E+11[c]	0.5	74.5
		r.	9.93E+02	0.5	0
261	$CCH_2(s_3) \Leftrightarrow CCH_2(s_2) + Pt(s)$	f.	2.08E+10	1	0
		r.	9.15E+10[c]	0.5	150
263	$CCH_2(s_3) + H(s) \Leftrightarrow CHCH_2(s_3) + Pt(s)$	f.	4.04E+11[c]	0.5	21.3
		r.	9.05E+10[c]	0.5	74.3
265	$CCH_2(s_3) + H(s) \Leftrightarrow CCH_3(s_3) + Pt(s)$	f.	4.04E+11[c]	0.5	22.6
		r.	9.12E+10[c]	0.5	112.3
267	$CCH_2(s_3) + H(s) \Leftrightarrow CCH(s) + H_2 + 3Pt(s)$	f.	4.04E+11[c]	0.5	63.1
		r.	3.39E+03	0.5	4.3
269	$CCH_2(s_3) + H(s) \Leftrightarrow C(s_3) + CH_3(s)$	f.	4.04E+11[c]	0.5	22.6
		r.	1.69E+11[c]	0.5	152.4
271	$C_2H_2(s_3) + H(s) \Leftrightarrow CHCH_2(s_3) + Pt(s)$	f.	4.00E+11[c]	0.5	114.8
		r.	9.05E+10[c]	0.5	15.5
273	$C_2H_2(s_3) \Leftrightarrow CCH_2(s_2) + Pt(s)$	f.	2.08E+10	1	95.2
		r.	9.15E+10[c]	0.5	76.7
275	$C_2H_2(s_3) \Leftrightarrow C_2H_2 + 3Pt(s)$	f.	2.08E+10	1	134
		r.	4.81E+02	0.5	0
277	$CCH(s) + H(s) + Pt(s) \Leftrightarrow CCH_2(s_3)$	f.	3.96E+11[c]	0.5	78.1
		r.	2.08E+10	1	57.1
279	$CCH(s) + H_2O(s) + 2Pt(s) \Leftrightarrow C_2H_2(s_3) + OH(s)$	f.	3.44E+10[c]	0.5	8.5
		r.	1.36E+11[c]	0.5	116.1
281	$CCH(s) + H_2O(s) \Leftrightarrow C_2H_2 + OH(s) + Pt(s)$	f.	1.38E+11[c]	0.5	17.9
		r.	1.56E+04	0.5	0
283	$CCH(s) + H(s) \Leftrightarrow C_2H_2 + 2Pt(s)$	f.	3.96E+11[c]	0.5	32.4
		r.	3.24E+03	0.5	14.2
285	$CCH(s) + H(s) + Pt(s) \Leftrightarrow C_2H_2(s_3)$	f.	3.96E+11[c]	0.5	32.4
		r.	2.08E+10	1	148.2
287	$CCH(s) + O(s) + Pt(s) \Leftrightarrow CO + CH(s_3)$	f.	1.34E+11[c]	0.5	38.1
		r.	3.53E+05	0.5	95.5
289	$CCH(s) + O(s) + Pt(s) \Leftrightarrow CHO + C(s_3)$	f.	1.34E+11[c]	0.5	38.1
		r.	3.91E+05	0.5	47.7
291	$CCH(s) + O(s) + 2Pt(s) \Leftrightarrow C(s_3) + CHO(s)$	f.	3.34E+10[c]	0.5	38.1
		r.	1.52E+11[c]	0.5	214.8
293	$CCH(s) + H_2O(s) + Pt(s) \Leftrightarrow CCH_2(s_2) + OH(s)$	f.	1.38E+11[c]	0.5	15.9
		r.	1.37E+11[c]	0.5	116
295	$CCH(s) + H_2(s) + Pt(s) \Leftrightarrow CCH_2(s_2) + H(s)$	f.	2.89E+11[c]	0.5	5.9
		r.	4.04E+11[c]	0.5	182
297	$CCH(s) + 5Pt(s) \Leftrightarrow C(s_3) + CH(s_3)$	f.	9.18E+10[c]	0.5	121.9
		r.	1.71E+11[c]	0.5	125.3
299	$CH_3(s) + OH(s) \Leftrightarrow CH_3OH + 2Pt(s)$	f.	1.45E+11[c]	0.5	36.6
		r.	5.84E+04	0.5	16
301	$CH_3(s) + H_2O(s) \Leftrightarrow CH_3OH + H(s) + Pt(s)$	f.	1.48E+11[c]	0.5	67.2
		r.	1.66E+05	0.5	14.5
303	$CH_3(s) + H(s) \Leftrightarrow CH_4 + 2Pt(s)$	f.	3.79E+11[c]	0.5	23.7
		r.	1.64E+04	0.5	49
305	$CH_3(s) + H(s) + Pt(s) \Leftrightarrow CH_2(s_2) + H_2(s)$	f.	3.79E+11[c]	0.5	138
		r.	2.79E+11[c]	0.5	5.9
307	$CH_3(s) + O(s) \Leftrightarrow CH_2O + H(s) + Pt(s)$	f.	1.42E+11[c]	0.5	23.3
		r.	1.69E+04	0.5	44.2
309	$CH_3(s) + O(s) \Leftrightarrow CH_2OH(s) + Pt(s)$	f.	1.42E+11[c]	0.5	26.9
		r.	8.24E+10[c]	0.5	82.6
311	$CH_3(s) + O(s) \Leftrightarrow CH_3O(s) + Pt(s)$	f.	1.42E+11[c]	0.5	33
		r.	8.18E+10[c]	0.5	72.3
313	$CH_3(s) + O(s) \Leftrightarrow CH_2O(s) + H(s)$	f.	1.42E+11[c]	0.5	23.3
		r.	3.87E+11[c]	0.5	90.9
315	$CH_3(s) + OH(s) \Leftrightarrow CH_4 + O(s) + Pt(s)$	f.	1.45E+11[c]	0.5	54.5
		r.	6.68E+04	0.5	17.1
317	$CH_3(s) + H_2O(s) \Leftrightarrow CH_4 + OH(s) + Pt(s)$	f.	1.48E+11[c]	0.5	27.5
		r.	7.93E+04	0.5	20.5
319	$CH_3(s) + OH(s) \Leftrightarrow CH_3OH(s) + Pt(s)$	f.	1.45E+11[c]	0.5	36.6
		r.	8.23E+10[c]	0.5	60.1
321	$CH_3(s) + H_2O + Pt(s) \Leftrightarrow CH_3OH(s) + H(s)$	f.	4.31E+05	0.5	0
		r.	4.03E+11[c]	0.5	31.5
323	$CH_3(s) + H_2O(s) \Leftrightarrow CH_3OH(s) + H(s)$	f.	1.48E+11[c]	0.5	23.1
		r.	4.03E+11[c]	0.5	12.4

(*continued on next page*)

Table 7 (*continued*)

No.	Reaction		Rate coefficients in the form $k_m = AT^{\beta}\exp(-\Delta E/RT)$		
			A[a]	β	ΔE[b]
325	$CH_2(s_2) + H_2O(s) \Leftrightarrow CH_3(s) + OH(s) + Pt(s)$	f.	1.49E+11[c]	0.5	18.2
		r.	1.45E+11[c]	0.5	74.8
327	$CH_2(s_2) + OH(s) \Leftrightarrow CH_2OH + 3Pt(s)$	f.	1.46E+11[c]	0.5	82.2
		r.	8.80E+03	0.5	0
329	$CH_2(s_2) + H(s) \Leftrightarrow CH_3(s) + 2Pt(s)$	f.	3.76E+11[c]	0.5	29
		r.	1.12E+11[c]	0.5	109.7
331	$CH_2(s_2) + O(s) \Leftrightarrow CHO + H(s) + 2Pt(s)$	f.	1.43E+11[c]	0.5	37.9
		r.	4.37E+04	0.5	1.3
333	$CH_2(s_2) + OH(s) \Leftrightarrow CH_2O + H(s) + 2Pt(s)$	f.	1.46E+11[c]	0.5	26.9
		r.	4.21E+03	0.5	66.4
335	$CH_2(s_2) + H_2O(s) \Leftrightarrow CH_3OH(s) + 2Pt(s)$	f.	1.49E+11[c]	0.5	8.4
		r.	8.23E+10[c]	0.5	76.3
337	$CH_2(s_2) + OH(s) \Leftrightarrow CH_2O(s) + H(s) + Pt(s)$	f.	1.46E+11[c]	0.5	26.9
		r.	3.87E+11[c]	0.5	113.1
339	$CH_2(s_2) + H(s) + Pt(s) \Leftrightarrow CH(s_3) + H_2(s)$	f.	3.76E+11[c]	0.5	115.2
		r.	2.76E+11[c]	0.5	16
341	$CH_2(s_2) + OH(s) \Leftrightarrow CH_2OH(s) + 2Pt(s)$	f.	1.46E+11[c]	0.5	29.5
		r.	8.24E+10[c]	0.5	104.8
343	$CH_2(s_2) + H_2O(s) \Leftrightarrow CH_2OH(s) + H(s) + Pt(s)$	f.	1.49E+11[c]	0.5	22
		r.	3.95E+11[c]	0.5	72
345	$CH(s_3) + H(s) \Leftrightarrow CH_2(s_2) + 2Pt(s)$	f.	3.70E+11[c]	0.5	57
		r.	1.15E+11[c]	0.5	100.1
347	$CH(s_3) + H(s) \Leftrightarrow C(s_3) + H_2(s)$	f.	3.70E+11[c]	0.5	37.2
		r.	2.74E+11[c]	0.5	120.3
349	$CH(s_3) + H(s) \Leftrightarrow C(s_3) + H_2 + Pt(s)$	f.	3.70E+11[c]	0.5	37.2
		r.	6.60E+04	0.5	93.5
351	$CH(s_3) + O(s) \Leftrightarrow CHO + 4Pt(s)$	f.	1.44E+11[c]	0.5	45.6
		r.	9.62E+02	0.5	44.4
353	$CH(s_3) + OH(s) \Leftrightarrow CHO + H(s) + 3Pt(s)$	f.	1.47E+11[c]	0.5	30.7
		r.	6.47E+03	0.5	0
355	$CH(s_3) + OH(s) \Leftrightarrow CHO(s) + H(s) + 2Pt(s)$	f.	1.47E+11[c]	0.5	34.8
		r.	9.45E+10[c]	0.5	151.3
357	$C(s_3) + OH(s) \Leftrightarrow CHO + 4Pt(s)$	f.	1.49E+11[c]	0.5	154.6
		r.	9.62E+02	0.5	0
359	$C(s_3) + H(s) \Leftrightarrow CH(s_3) + Pt(s)$	f.	3.65E+11[c]	0.5	159
		r.	1.18E+11[c]	0.5	40.6
361	$C(s_3) + O(s) \Leftrightarrow CO + 4Pt(s)$	f.	1.45E+11[c]	0.5	53.9
		r.	8.23E+02	0.5	92.7
363	$C(s_3) + O(s) \Leftrightarrow CO(s_2) + 2Pt(s)$	f.	1.45E+11[c]	0.5	53.9
		r.	8.29E+10[c]	0.5	226.5
365	$C(s_3) + OH(s) \Leftrightarrow CHO(s) + 3Pt(s)$	f.	1.49E+11[c]	0.5	82.4
		r.	8.22E+10[c]	0.5	94.8
367	$C(s_3) + OH(s) \Leftrightarrow CO + H(s) + 3Pt(s)$	f.	1.49E+11[c]	0.5	37.6
		r.	5.54E+03	0.5	36.5
369	$C(s_3) + OH(s) \Leftrightarrow CO(s_2) + H(s) + Pt(s)$	f.	1.49E+11[c]	0.5	37.6
		r.	3.74E+11[c]	0.5	170.3
371	$C(s_3) + O_2 \Leftrightarrow CO(s_2) + O(s)$	f.	5.59E+06	−0.5	0
		r.	1.24E+11[c]	0.5	439.5
373	$C(s_3) + H_2O(s) \Leftrightarrow CH(s_3) + OH(s)$	f.	1.52E+11[c]	0.5	168.6
		r.	1.47E+11[c]	0.5	36.9
375	$C(s_3) + CH_2O(s) \Leftrightarrow CH_2(s_2) + CO(s_2)$	f.	1.54E+11[c]	0.5	10.4
		r.	1.47E+11[c]	0.5	69.1
377	$CO(s_2) \Leftrightarrow CO + 2Pt(s)$	f.	1.04E+12	1	133.8
		r.	5.27E+04	0.5	0
379	$CO(s_2) + O(s) \Leftrightarrow CO_2(s_2) + Pt(s)$	f.	1.24E+11[c]	0.5	97.3
		r.	6.75E+10[c]	0.5	154.3
381	$CO(s_2) + O(s) \Leftrightarrow CO_2 + 3Pt(s)$	f.	1.24E+11[c]	0.5	97.3
		r.	3.71E+01	0.5	139.3
383	$CO(s_2) + OH(s) \Leftrightarrow CO_2(s_2) + H(s)$	f.	1.26E+11[c]	0.5	86.8
		r.	3.80E+11[c]	0.5	81.3
385	$CO(s_2) + O_2 + Pt(s) \Leftrightarrow CO_2(s_2) + O(s)$	f.	6.47E+06	−0.5	33.3
		r.	1.18E+11[c]	0.5	304
387	$CO(s_2) + CH_3O(s) \Leftrightarrow CH_3(s) + CO_2(s_2)$	f.	1.23E+11[c]	0.5	26.5
		r.	1.38E+11[c]	0.5	48.9
389	$CO(s_2) + OH(s) \Leftrightarrow COOH(s) + 2Pt(s)$	f.	1.26E+11[c]	0.5	55.6
		r.	6.71E+10[c]	0.5	31.1
391	$CO(s_2) + H_2(s) + Pt(s) \Leftrightarrow COH(s_3) + H(s)$	f.	2.73E+11[c]	0.5	129.2
		r.	3.78E+11[c]	0.5	29
393	$CO_2(s_2) \Leftrightarrow CO_2 + 2Pt(s)$	f.	2.08E+10	1	15.1
		r.	2.50E+02	0.5	0
395	$CH_3OH(s) + H(s) \Leftrightarrow CH_4 + OH(s) + Pt(s)$	f.	4.03E+11[c]	0.5	7.7
		r.	7.93E+04	0.5	7.1
397	$CH_3OH(s) + H(s) \Leftrightarrow CH_2OH(s) + H_2(s)$	f.	4.03E+11[c]	0.5	83.6
		r.	2.88E+11[c]	0.5	5.5

Table 7 (*continued*)

No.	Reaction		Rate coefficients in the form $k_m = AT^{\beta}\exp(-\Delta E/RT)$		
			A[a]	β	ΔE[b]
399	$CH_3OH(s) + O(s) \Leftrightarrow CH_2OH(s) + OH(s)$	f.	1.30E+11[c]	0.5	7.8
		r.	1.30E+11[c]	0.5	35.5
401	$CH_3O(s) + H(s) \Leftrightarrow CH_3OH + 2Pt(s)$	f.	3.92E+11[c]	0.5	25.3
		r.	5.84E+04	0.5	33.1
403	$CH_3O(s) + H(s) \Leftrightarrow CH_3(s) + OH(s)$	f.	3.92E+11[c]	0.5	37.6
		r.	1.45E+11[c]	0.5	65.5
405	$CH_3O(s) + H_2O(s) \Leftrightarrow CH_3OH(s) + OH(s)$	f.	1.31E+11[c]	0.5	8.5
		r.	1.32E+11[c]	0.5	23.6
407	$CH_3O(s) + H(s) \Leftrightarrow CH_4 + O(s) + Pt(s)$	f.	3.92E+11[c]	0.5	43.8
		r.	6.68E+04	0.5	34.2
409	$CH_3O(s) + H(s) \Leftrightarrow CH_3OH(s) + Pt(s)$	f.	3.92E+11[c]	0.5	25.3
		r.	8.23E+10[c]	0.5	77.2
411	$CH_3O(s) \Leftrightarrow CH_2O + H(s)$	f.	2.08E+10	1	47.8
		r.	1.69E+04	0.5	38.3
413	$CH_3O(s) + H(s) \Leftrightarrow CH_2O(s) + H_2(s)$	f.	3.92E+11[c]	0.5	59.5
		r.	2.82E+11[c]	0.5	43.6
415	$CH_3O(s) + Pt(s) \Leftrightarrow CH_2O(s) + H(s)$	f.	8.18E+10[c]	0.5	19.7
		r.	3.87E+11[c]	0.5	38.3
417	$CH_2OH(s) + H(s) \Leftrightarrow CH_3OH + 2Pt(s)$	f.	3.95E+11[c]	0.5	33.9
		r.	5.84E+04	0.5	20.4
419	$CH_2OH(s) \Leftrightarrow CH_2OH + Pt(s)$	f.	2.08E+10	1	160
		r.	2.38E+05	0.5	0
421	$CH_2OH(s) + H(s) \Leftrightarrow CH_3(s) + OH(s)$	f.	3.95E+11[c]	0.5	45.6
		r.	1.45E+11[c]	0.5	52.8
423	$CH_2OH(s) + H_2O(s) \Leftrightarrow CH_3OH(s) + OH(s)$	f.	1.32E+11[c]	0.5	19.4
		r.	1.32E+11[c]	0.5	15
425	$CH_2OH(s) + H(s) \Leftrightarrow CH_3OH(s) + Pt(s)$	f.	3.95E+11[c]	0.5	33.9
		r.	8.23E+10[c]	0.5	64.5
427	$CH_2OH(s) \Leftrightarrow CH_2O + H(s)$	f.	2.08E+10	1	58.2
		r.	1.69E+04	0.5	28
429	$CH_2OH(s) + H(s) \Leftrightarrow CH_2O(s) + H_2(s)$	f.	3.95E+11[c]	0.5	67.4
		r.	2.82E+11[c]	0.5	30.9
431	$CH_2OH(s) + O(s) \Leftrightarrow CH_2O + OH(s) + Pt(s)$	f.	1.29E+11[c]	0.5	22.5
		r.	2.86E+04	0.5	48
433	$CH_2OH(s) + 2Pt(s) \Leftrightarrow CHOH(s_2) + H(s)$	f.	8.24E+10[c]	0.5	74.6
		r.	3.87E+11[c]	0.5	37.8
435	$CH_2OH(s) + H(s) + Pt(s) \Leftrightarrow CHOH(s_2) + H_2(s)$	f.	3.95E+11[c]	0.5	94.1
		r.	2.82E+11[c]	0.5	5.1
437	$CH_2OH(s) + Pt(s) \Leftrightarrow CH_2O(s) + H(s)$	f.	8.24E+10[c]	0.5	16.3
		r.	3.87E+11[c]	0.5	23.3
439	$CH_2O(s) + H(s) \Leftrightarrow CH_2OH + 2Pt(s)$	f.	3.87E+11[c]	0.5	176.5
		r.	5.94E+04	0.5	0
441	$CH_2O(s) \Leftrightarrow CH_2O + Pt(s)$	f.	2.08E+10	1	46.7
		r.	2.38E+04	0.5	0
443	$CH_2O(s) + Pt(s) \Leftrightarrow CHO(s) + H(s)$	f.	8.23E+10[c]	0.5	44.7
		r.	3.78E+11[c]	0.5	56.3
445	$CH_2O(s) + H(s) \Leftrightarrow CHO(s) + H_2(s)$	f.	3.87E+11[c]	0.5	41.5
		r.	2.76E+11[c]	0.5	5.5
447	$CH_2O(s) + O(s) \Leftrightarrow CHO(s) + OH(s)$	f.	1.27E+11[c]	0.5	9.9
		r.	1.27E+11[c]	0.5	74
449	$CH_2O(s) + OH(s) \Leftrightarrow CHO(s) + H_2O(s)$	f.	1.29E+11[c]	0.5	9.4
		r.	1.29E+11[c]	0.5	43.6
451	$CH_2O(s) + OH(s) \Leftrightarrow CHO(s) + H_2O + Pt(s)$	f.	1.29E+11[c]	0.5	9.4
		r.	4.47E+05	0.5	3.4
453	$CHOH(s_2) + 2Pt(s) \Leftrightarrow COH(s_3) + H(s)$	f.	8.23E+10[c]	0.5	47.7
		r.	3.78E+11[c]	0.5	97.6
455	$CHOH(s_2) \Leftrightarrow CHO(s) + H(s)$	f.	2.08E+10	1	18
		r.	3.78E+11[c]	0.5	83
457	$CHOH(s_2) + H(s) + Pt(s) \Leftrightarrow COH(s_3) + H_2(s)$	f.	3.87E+11[c]	0.5	57.7
		r.	2.76E+11[c]	0.5	54.7
459	$CHOH(s_2) + H(s) \Leftrightarrow CHO(s) + H_2(s) + Pt(s)$	f.	3.87E+11[c]	0.5	50.2
		r.	2.76E+11[c]	0.5	62.2
461	$CHO(s) + 2Pt(s) \Leftrightarrow CO(s_2) + H(s)$	f.	8.22E+10[c]	0.5	20
		r.	3.74E+11[c]	0.5	151
463	$CHO(s) + H(s) \Leftrightarrow CO + H_2(s) + Pt(s)$	f.	3.78E+11[c]	0.5	35.8
		r.	1.90E+05	0.5	0
465	$CHO(s) + H(s) + Pt(s) \Leftrightarrow CO(s_2) + H_2(s)$	f.	3.78E+11[c]	0.5	22.9
		r.	2.73E+11[c]	0.5	99.5
467	$CHO(s) + H(s) \Leftrightarrow CO(s_2) + H_2$	f.	3.78E+11[c]	0.5	22.9
		r.	7.64E+04	0.5	72.7
469	$CHO(s) + O(s) + Pt(s) \Leftrightarrow CO(s_2) + OH(s)$	f.	1.25E+11[c]	0.5	27.3
		r.	1.26E+11[c]	0.5	213.5
471	$CHO(s) + OH(s) + Pt(s) \Leftrightarrow CO(s_2) + H_2O(s)$	f.	1.27E+11[c]	0.5	23.9
		r.	1.28E+11[c]	0.5	183.1

(*continued on next page*)

Table 7 (*continued*)

No.	Reaction		Rate coefficients in the form $k_m = AT^{\beta}\exp(-\Delta E/RT)$		
			A[a]	β	ΔE[b]
473	$COH(s_3) \Leftrightarrow CO(s_2) + H(s)$	f.	2.08E+10	1	0
		r.	3.74E+11[c]	0.5	166
475	$COOH(s) + 2Pt(s) \Leftrightarrow CO_2(s_2) + H(s)$	f.	6.71E+10[c]	0.5	25.6
		r.	3.80E+11[c]	0.5	19.1
477	$COOH(s) + H(s) + Pt(s) \Leftrightarrow CO(s_2) + H_2O(s)$	f.	3.83E+11[c]	0.5	28.9
		r.	1.28E+11[c]	0.5	86.4
479	$COOH(s) + O(s) + Pt(s) \Leftrightarrow CO_2(s_2) + OH(s)$	f.	1.19E+11[c]	0.5	29.2
		r.	1.20E+11[c]	0.5	107.4
481	$COOH(s) + OH(s) + Pt(s) \Leftrightarrow CO_2(s_2) + H_2O(s)$	f.	1.20E+11[c]	0.5	31.6
		r.	1.21E+11[c]	0.5	82.8
483	$H_2 + Pt(s) \Leftrightarrow H_2(s)$	f.	4.16E+04	0.5	0
		r.	2.08E+10	1	26.8
485	$H_2 + O(s) + Pt(s) \Leftrightarrow H(s) + OH(s)$	f.	4.22E+04	0.5	0
		r.	3.33E+11[c]	0.5	142.3
487	$H_2 + O_2(s_2) \Leftrightarrow H(s) + OOH(s)$	f.	5.93E+04	0.5	0
		r.	3.62E+11[c]	0.5	192.7
489	$O_2 + 2Pt(s) \Leftrightarrow O_2(s_2)$	f.	8.80E+05	−0.5	0
		r.	2.08E+10	1	44.3
491	$O_2 + H(s) + Pt(s) \Leftrightarrow O(s) + OH(s)$	f.	2.50E+06	−0.5	0
		r.	1.23E+11[c]	0.5	276
493	$O_2 + 2Pt(s) \Leftrightarrow O(s) + O(s)$	f.	8.80E+05	−0.5	0
		r.	1.19E+11[c]	0.5	213.5
495	$O_2 + H(s) \Leftrightarrow OOH(s)$	f.	2.50E+06	−0.5	0
		r.	2.08E+10	1	157.2
497	$OH + Pt(s) \Leftrightarrow OH(s)$	f.	3.21E+05	0.5	0
		r.	2.08E+10	1	246.7
499	$O + Pt(s) \Leftrightarrow O(s)$	f.	3.32E+05	0.5	0
		r.	2.08E+10	1	355.9
501	$H_2O + O(s) + Pt(s) \Leftrightarrow OH(s) + OH(s)$	f.	2.37E+05	0.5	6.3
		r.	1.26E+11[c]	0.5	76.9
503	$H_2O + H(s) + Pt(s) \Leftrightarrow H_2(s) + OH(s)$	f.	1.66E+05	0.5	44.9
		r.	2.48E+11[c]	0.5	5.8
505	$HO_2 + Pt(s) \Leftrightarrow OOH(s)$	f.	2.31E+05	0.5	0
		r.	2.08E+10	1	204.1
507	$HO_2 + 2Pt(s) \Leftrightarrow O(s) + OH(s)$	f.	5.77E+04	0.5	0
		r.	1.23E+11[c]	0.5	573.3
509	$HO_2 + 3Pt(s) \Leftrightarrow O_2(s_2) + H(s)$	f.	8.55E+03	0.5	0
		r.	3.45E+11[c]	0.5	341.6
511	$H_2O_2 + 2Pt(s) \Leftrightarrow H_2O_2(s_2)$	f.	4.26E+04	0.5	0
		r.	2.08E+10	1	27.1
513	$H_2O_2 + H(s) + Pt(s) \Leftrightarrow OH(s) + H_2O(s)$	f.	1.21E+05	0.5	0
		r.	1.29E+11[c]	0.5	309.1
515	$H_2O_2 + 2Pt(s) \Leftrightarrow OH(s) + OH(s)$	f.	4.26E+04	0.5	0
		r.	1.26E+11[c]	0.5	277
517	$H_2O_2 + 2Pt(s) \Leftrightarrow O(s) + H_2O(s)$	f.	4.26E+04	0.5	0
		r.	1.26E+11[c]	0.5	246.6
519	$H_2O_2 + H(s) + Pt(s) \Leftrightarrow H_2(s) + OOH(s)$	f.	1.21E+05	0.5	4.5
		r.	2.64E+11[c]	0.5	47.1
521	$H_2(s) + O(s) \Leftrightarrow H(s) + OH(s)$	f.	2.38E+11[c]	0.5	5.5
		r.	3.33E+11[c]	0.5	120.5
523	$H_2(s) + Pt(s) \Leftrightarrow H(s) + H(s)$	f.	2.52E+11[c]	0.5	37.4
		r.	3.98E+11[c]	0.5	90.3
525	$O_2(s_2) + H(s) \Leftrightarrow O(s) + OH(s) + Pt(s)$	f.	3.45E+11[c]	0.5	9.1
		r.	1.23E+11[c]	0.5	231.7
527	$O_2(s_2) \Leftrightarrow O(s) + O(s)$	f.	2.08E+10	1	4.4
		r.	1.19E+11[c]	0.5	173.6
529	$O_2(s_2) + H(s) \Leftrightarrow OOH(s) + 2Pt(s)$	f.	3.45E+11[c]	0.5	9.1
		r.	7.45E+10[c]	0.5	112.9
531	$H(s) + O(s) \Leftrightarrow OH + 2Pt(s)$	f.	3.19E+11[c]	0.5	184.2
		r.	8.03E+04	0.5	0
533	$O(s) + H_2O(s) \Leftrightarrow OH(s) + OH(s)$	f.	1.26E+11[c]	0.5	46.5
		r.	1.26E+11[c]	0.5	76.9
535	$H(s) + O(s) \Leftrightarrow OH(s) + Pt(s)$	f.	3.19E+11[c]	0.5	43.1
		r.	9.57E+10[c]	0.5	105.6
537	$H(s) + OH(s) \Leftrightarrow H_2O(s) + Pt(s)$	f.	3.33E+11[c]	0.5	46.7
		r.	9.60E+10[c]	0.5	78.8
539	$H(s) + OH(s) \Leftrightarrow H_2O + 2Pt(s)$	f.	3.33E+11[c]	0.5	46.7
		r.	5.84E+04	0.5	38.6
541	$H(s) + H(s) \Leftrightarrow H_2 + 2Pt(s)$	f.	3.98E+11[c]	0.5	90.3
		r.	1.04E+04	0.5	10.6
543	$H(s) \Leftrightarrow H + Pt(s)$	f.	2.08E+10	1	255.4
		r.	1.32E+06	0.5	0
545	$H(s) + H_2O_2(s_2) \Leftrightarrow H_2O + OH(s) + 2Pt(s)$	f.	3.73E+11[c]	0.5	5.9
		r.	7.05E+04	0.5	241.8

Table 7 (*continued*)

No.	Reaction		Rate coefficients in the form $k_m = AT^{\beta}\exp(-\Delta E/RT)$		
			A[a]	β	ΔE[b]
547	H(s) + OOH(s) ⇔ H_2O + O(s) + Pt(s)	f.	3.62E+11[c]	0.5	27.2
		r.	2.37E+05	0.5	110.7
549	H(s) + OOH(s) ⇔ H_2O_2 + 2Pt(s)	f.	3.62E+11[c]	0.5	95.7
		r.	4.26E+04	0.5	0
551	H(s) + H_2O(s) ⇔ H_2(s) + OH(s)	f.	3.47E+11[c]	0.5	85.1
		r.	2.48E+11[c]	0.5	5.8
553	H(s) + OOH(s) ⇔ O(s) + H_2O(s)	f.	3.62E+11[c]	0.5	27.2
		r.	1.26E+11[c]	0.5	150.9
555	H(s) + $H_2O_2(s_2)$ ⇔ OH(s) + H_2O(s) + Pt(s)	f.	3.73E+11[c]	0.5	5.9
		r.	1.29E+11[c]	0.5	282
557	H(s) + OOH(s) ⇔ OH(s) + OH(s)	f.	3.62E+11[c]	0.5	27.2
		r.	1.26E+11[c]	0.5	181.4
559	H(s) + OOH(s) ⇔ $H_2O_2(s_2)$	f.	3.62E+11[c]	0.5	91
		r.	2.08E+10	1	22.4
561	H_2O(s) ⇔ H_2O + Pt(s)	f.	2.08E+10	1	40.2
		r.	2.34E+05	0.5	0
563	OOH(s) + Pt(s) ⇔ O(s) + OH(s)	f.	7.45E+10[c]	0.5	20.6
		r.	1.23E+11[c]	0.5	132.3
565	$H_2O_2(s_2)$ ⇔ OH(s) + OH(s)	f.	2.08E+10	1	0
		r.	1.26E+11[c]	0.5	249.9

[a] Pre-exponential factor: s^{-1}.
[b] Activation energy: kJ mol^{-1}.
[c] Pre-exponential factor must be multiplied by $A(\mathrm{Pt})\mathcal{N}_A\Gamma$.

Supplementary material

The online version of this article contains additional supplementary material.

Please visit DOI: 10.1016/j.jcat.2008.08.014.

References

[1] R.A. Buyanov, N.A. Pakhonov, Kinet. Catal. 42 (2001) 64.
[2] M.M. Bahsin, J.H. McCain, B.V. Vora, T. Imai, P.R. Pujadó, Appl. Catal. A 221 (2001) 397.
[3] F. Zaera, Surf. Sci. 500 (2002) 947.
[4] M. Huff, L.D. Schmidt, J. Phys. Chem. 97 (1993) 11815.
[5] K. Venkataraman, J.M. Redenius, L.D. Schmidt, Chem. Eng. Sci. 57 (2002) 2335.
[6] A.S. Bodke, D.A. Henning, L.D. Schmidt, S.S. Bharadwaj, J.J. Maj, J. Siddall, J. Catal. 191 (2000) 62.
[7] D.A. Henning, L.D. Schmidt, Chem. Eng. Sci. 57 (2002) 2615.
[8] A. Loaiza, M. Xu, F. Zaera, J. Catal. 159 (1996) 127.
[9] F. Zaera, T.V.W. Janssens, H. Öfner, Surf. Sci. 368 (1996) 371.
[10] C. De La Cruz, N. Sheppard, Phys. Chem. Chem. Phys. 1 (1999) 329.
[11] H.E. Newell, M.R.S. McCoustra, M.A. Chesters, C. De La Cruz, J. Chem. Soc. Faraday Trans. 94 (1998) 3695.
[12] Y.Y. Yeo, A. Stuck, C.E. Wartnaby, D.A. King, Chem. Phys. Lett. 259 (1996) 28.
[13] R.D. Cortright, R.M. Watwe, B.E. Spiewak, J.A. Dumesic, Catal. Today 53 (1999) 395.
[14] R.M. Watwe, R.D. Cortright, J.K. Norsøskov, J.A. Dumesic, J. Phys. Chem. B 140 (2000) 2299.
[15] E.A. Carter, B.E. Koel, Surf. Sci. 226 (1990) 339.
[16] P.S. Cremer, X. Su, Y.R. Shen, G.A. Somorjai, J. Am. Chem. Soc. 118 (1996) 2942.
[17] R. Deng, E. Herceg, M. Trenary, Surf. Sci. 560 (2004) L195.
[18] J.E. Rekoske, R.D. Cortright, S.A. Goddard, S.B. Sharma, J.A. Dumesic, J. Phys. Chem. 96 (1992) 1880.
[19] J. Warnatz, Proc. Combust. Inst. 24 (1992) 553.
[20] D. Chatterjee, O. Deutschmann, J. Warnatz, Faraday Discuss. 119 (2001) 371.
[21] S. Tischer, C. Correa, O. Deutschmann, Catal. Today 69 (2001) 57.
[22] P. Aghalayam, Y.K. Park, N. Fernandez, V. Papavasiliou, A.B. Mhadeshwar, D.G. Vlachos, J. Catal. 213 (2003) 23.
[23] A.B. Mhadeshwar, D.G. Vlachos, J. Phys. Chem. 108 (2004) 15246.
[24] A.B. Mhadeshwar, D.G. Vlachos, Ind. Eng. Chem. Res. 46 (2007) 5310.
[25] R. Quiceno, J. Perez-Ramirez, J. Warnatz, O. Deutschmann, Appl. Catal. A 166 (2006) 303.
[26] D. Zerkle, M.D. Allendorf, M. Wolf, O. Deutschmann, J. Catal. 196 (2000) 18.
[27] M. Huff, I.P. Andoulakis, I.P. Sinfelt, S.C. Reyes, J. Catal. 191 (2000) 46.
[28] F. Donsí, K.A. William, L.D. Schmidt, Ind. Eng. Chem. Res. 44 (2005) 3453.
[29] A. Beretta, E. Ranzi, P. Forzatti, Chem. Eng. Sci. 56 (2001) 779.
[30] E. Shustorovich, A.T. Bell, Surf. Sci. 205 (1988) 492.
[31] E. Shustorovich, A.T. Bell, Surf. Sci. 289 (1993) 127.
[32] P. Parades-Olivera, E.M. Patrito, H.L. Sellers, Surf. Sci. 327 (1995) 330.
[33] P. Parades-Olivera, E.M. Patrito, H.L. Sellers, Surf. Sci. 313 (1994) 25.
[34] I.V. Kuz'min, A.V. Zeigarnik, Kinet. Catal. 45 (2004) 561.
[35] B. Shen, X. Chen, K. Fan, J. Deng, Surf. Sci. 408 (1998) 128.
[36] A.V. Zeigarnik, R.E. Valdés-Pérez, N.I. Egorova, Surf. Sci. 487 (2001) 146.
[37] Y.-Z. Lin, J. Sun, J. Lin, H.-B. Chen, D.-W. Liao, J. Mol. Struct. 587 (2003) 63.
[38] S.G. Podkolzin, R. Alcal, J.A. Dumesic, J. Mol. Catal. A 218 (2004) 217.
[39] J. Kua, W.A. Goddard III, J. Am. Chem. Soc. 121 (1999) 10928.
[40] J.A. Dumesic, D.F. Rudd, L.M. Aparicio, J.E. Rekoske, A.A. Treviño, The Microkinetics of Heterogeneous Catalysts, Am. Chem. Soc., 1993.
[41] L. Giani, G. Groppi, E. Tronconi, Ind. Eng. Chem. Res. 44 (2005) 9078.
[42] J.G. Fourie, J.P. Du Plessis, Chem. Eng. Sci. 57 (2002) 2781.
[43] A. Monzón, T.F. Garetto, A. Borgna, Appl. Catal. A 245 (2003) 279.
[44] A. Bhattacharya, V.V. Calmidi, R.L. Mahaja, Int. J. Heat Mass Transfer 45 (2002) 1017.
[45] K.M. Leung, R.P. Lindstedt, Combust. Flame 102 (1995) 123.
[46] R. Wanker, H. Raupenstrauch, G. Staidinger, Chem. Eng. Sci. 55 (2000) 4709.
[47] C. Morley, Gaseq: A Chemical Equilibrium Programme for Windows, http://www.arcl02.dsl.pipex.com/.
[48] M.E. Coltrin, R.J. Kee, F.M. Rupley, E. Meeks, SURFACE CHEMKIN-III: A Fortran Package for Analyzing Heterogeneous Chemical Kinetics at a Solid-Surface–Gas Phase Interfaces, Tech. Rep. SAND90-8003C, Sandia National Laboratories, 1992.
[49] W. Juchmann, H. Latzel, D.I. Shin, G. Peiter, T. Dreier, H.-R. Volpp, J. Wolfrum, R.P. Lindstedt, K.M. Leung, Proc. Combust. Inst. 27 (1998) 469.
[50] R.P. Lindstedt, G. Skevis, Proc. Combust. Inst. 28 (2000) 1801.
[51] R.P. Lindstedt, M.P. Meyer, Proc. Combust. Inst. 29 (2002) 1395.
[52] K.A. Rizos, Ph.D. thesis, Imperial College, London, 2003.
[53] H. Sun, S.I. Yang, G. Jomaas, C.K. Law, Proc. Combust. Inst. 31 (2007) 439.
[54] C.A. Naylor, R.V. Wheeler, J. Chem. Soc. II (1931) 2456.
[55] I.A.B. Reid, C. Robinson, D.B. Smith, Proc. Combust. Inst. 20 (1984) 1833.
[56] A. Burcat, K. Scheller, A. Lifshitz, Combust. Flame 16 (1971) 29.
[57] P. Dagaut, J.-C. Boettner, M. Cathonnet, Combust. Sci. Technol. 77 (1991) 127.
[58] P. Dagaut, J.-C. Boettner, M. Cathonnet, Int. J. Chem. Kinet. 22 (1990) 641.
[59] N.M. Marinov, P.C. Malte, Int. J. Chem. Kinet. 27 (1995) 957.
[60] J.B. Homer, G.B. Kistiakowsky, J. Chem. Phys. 47 (1967) 5290.
[61] E. Fridell, A. Rosen, B. Kasemo, Langmuir 10 (1994) 699.
[62] P. Aghalayam, Y.K. Park, D.G. Vlachos, AIChE J. 46 (2000) 2017.
[63] A.U. Nilekar, J. Greeley, M. Mavrikakis, Angew. Chem. Int. Ed. 12 (2006) 7046.
[64] J.B. Hudson, Surface Science: An Introduction, John Wiley & Sons, 1998.
[65] C. Panja, N. Saliba, B.E. Koel, Surf. Sci. 395 (1998) 2489.
[66] S. Ljungström, B. Kasemo, A. Rosen, T. Wahström, E. Fridell, Surf. Sci. 216 (1989) 63.
[67] K.W. Kolasinski, Surface Science Foundation of Catalysis and Nanoscience, John Wiley & Sons, 2002.
[68] R.I. Masel, Principle of Adsorption and Reaction on Solid Surfaces, John Wiley & Sons, 1996.
[69] A. Clark, The Theory of Adsorption and Catalysis, Academic Press, New York, 1970.
[70] D. Velic, R.J. Levis, J. Chem. Phys. 104 (1996) 9629.
[71] E. Shustorovich, H. Sellers, Surf. Sci. Rep. 31 (1998) 1.
[72] E. Shustorovich, A.V. Zeigarnik, Surf. Sci. 527 (2003) 137.
[73] J. Kua, W.A. Goddard, J. Phys. Chem. 102 (1998) 9492.

[74] J. Kua, F. Faglioni, W.A. Goddard, J. Am. Chem. Soc. 122 (2000) 2309.
[75] R.M. Watwe, B.E. Spiewak, R.D. Cortright, J.A. Dumesic, J. Catal. 180 (1998) 184.
[76] B.E. Spiewak, R.D. Cortright, J.A. Dumesic, J. Catal. 176 (1998) 405.
[77] E. Shustorovich, Metal-Surface Reactions Energetics: Theory and Applications to Heterogeneous Catalysis, Chemisorption and Surface Diffusion, VHC Publishers, 1991.
[78] J.L. Gland, B.A. Sexton, G.B. Fisher, Surf. Sci. 95 (1980) 587.
[79] G.T. Fujimoto, G.S. Selwyn, J.T. Kelser, M.C. Lin, J. Phys. Chem. 87 (1983) 1906.
[80] A.B. Anton, D.C. Cadogan, Surf. Sci. 229 (1990) L538.
[81] E. Shustorovich, Adv. Catal. 37 (1990) 101.
[82] S.G. Brass, G. Ehrlich, Surf. Sci. 187 (1987) 21.
[83] C.T. Campbell, G. Ertl, H. Kuipers, J. Segner, Surf. Sci. 107 (1981) 207.
[84] B.A. Sexton, A.E. Hughes, Surf. Sci. 140 (1984) 227.
[85] X.L. Zhou, X.-Y. Zhu, J.M. White, Surf. Sci. 193 (1988) 387.
[86] J. Kubota, S. Ichihara, J.N. Kondo, K. Domen, C. Hie, Surf. Sci. 357 (1996) 634.
[87] R.G. Windham, M.E. Bartram, B.E. Koel, J. Phys. Chem. 92 (1988) 2862.
[88] P. Sautet, J.-F. Paul, Catal. Lett. 9 (1991) 245.
[89] G. Szulczewski, R.J. Levis, J. Am. Chem. Soc. 118 (1996) 3521.
[90] J. Shen, J.M. Hill, R.M. Watwe, B.E. Spiewak, J.A. Dumesic, J. Phys. Chem. B 103 (1999) 3923.
[91] D.R. Lide, et al., CRC Handbook of Chemistry and Physics, 87th ed., CRC Press, 2006–2007, http://www.hbcpnetbase.com.
[92] A. Michaelides, Z.-P. Liu, C.J. Zhang, A. Alavi, D.A. King, P. Hu, J. Am. Chem. Soc. 125 (2003) 3704.
[93] A.B. Mhadeshwar, D.G. Vlachos, Combust. Flame 142 (2005) 289.
[94] A. Bourane, D. Bianchi, J. Catal. 220 (2003) 3.
[95] C.T. Campbell, G. Ertl, H. Kuipers, J. Segner, J. Chem. Phys. 73 (1980) 5863.
[96] T.V.W. Janssens, F. Zaera, J. Phys. Chem. 100 (1996) 14118.
[97] M. Wolf, O. Deutchmann, F. Behrendt, J. Warnatz, Catal. Lett. 61 (1999) 15.
[98] A.T. Anghel, D.J. Wales, S.J. Jenkins, D.A. King, J. Chem. Phys. 126 (2007) 44710.
[99] M.J. Frisch, G.W. Trucks, H.B. Schlegel, G.E. Scuseria, M.A. Robb, J.R. Cheeseman, J.A. Montgomery Jr., T. Vreven, K.N. Kudin, J.C. Burant, J.M. Millam, S.S. Iyengar, J. Tomasi, V. Barone, B. Mennucci, M. Cossi, G. Scalmani, N. Rega, G.A. Petersson, H. Nakatsuji, M. Hada, M. Ehara, K. Toyota, R. Fukuda, J. Hasegawa, M. Ishida, T. Nakajima, Y. Honda, O. Kitao, H. Nakai, M. Klene, X. Li, J.E. Knox, H.P. Hratchian, J.B. Cross, V. Bakken, C. Adamo, J. Jaramillo, R. Gomperts, R.E. Stratmann, O. Yazyev, A.J. Austin, R. Cammi, C. Pomelli, J.W. Ochterski, P.Y. Ayala, K. Morokuma, G.A. Voth, P. Salvador, J.J. Dannenberg, V.G. Zakrzewski, S. Dapprich, A.D. Daniels, M.C. Strain, O. Farkas, D.K. Malick, A.D. Rabuck, K. Raghavachari, J.B. Foresman, J.V. Ortiz, Q. Cui, A.G. Baboul, S. Clifford, J. Cioslowski, B.B. Stefanov, G. Liu, A. Liashenko, P. Piskorz, I. Komaromi, R.L. Martin, D.J. Fox, T. Keith, M.A. Al-Laham, C.Y. Peng, A. Nanayakkara, M. Challacombe, P.M.W. Gill, B. Johnson, W. Chen, M.W. Wong, C. Gonzalez, J.A. Pople, Gaussian 03, Revision C.02, Gaussian Inc., Wallingford, CT, 2004.
[100] A.G. Baboul, L.A. Curtiss, P.C. Redfern, K. Raghavachari, J. Chem. Phys. 110 (1999) 7650–7657.
[101] A.D. Becke, J. Chem. Phys. 98 (1993) 5648.
[102] J.V. Barth, Surf. Sci. Rep. 40 (2000) 75.
[103] R.G. Susnow, A.M. Dean, W.H. Green, P.K. Peczak, L.J. Broadbelt, J. Phys. Chem. A 101 (1997) 3731.
[104] O. Deutschmann, L.I. Maiera, U. Riedela, A.H. Stroemmanb, R.W. Dibble, Catal. Today 59 (2000) 141.
[105] O. Deutschmann, F. Behrendt, J. Warnatz, Catal. Today 21 (1994) 461.
[106] Y.-K. Sun, W.H. Weinberg, J. Vac. Sci. Technol. A 8 (1990) 2445.
[107] S. Raimondeau, P. Aghalayam, A.B. Mhadeshwar, Ind. Eng. Chem. Res. 42 (2003) 1174.
[108] V.P. Zhdanov, Surf. Sci. Rep. 12 (1991) 185.
[109] F. Gudmundson, J.L. Persson, M. Försth, F. Behrendt, B. Kasemo, A. Rosén, J. Catal. 179 (1998) 420.
[110] C. Appel, J. Mantzaras, R. Schaeren, R. Bombach, A. Inauen, B. Kaeppeli, B. Hemmerling, A. Stampanoni, Combust. Flame 128 (2002) 340.
[111] F. Zaera, Acc. Chem. Res. (1992) 260.
[112] M. Salmerón, G.A. Somorjai, J. Phys. Chem. 86 (1992) 341.
[113] C.-H. Hwang, C.-W. Lee, H. Kang, C.M. Kim, Surf. Sci. 490 (2001) 144.
[114] F. Zaera, J. Phys. Chem. 94 (1990) 5090.
[115] G.A. Somorjai, M.A. Van Hove, B.E. Bent, J. Phys. Chem. 92 (1988) 973.
[116] D.B. Kang, A.B. Anderson, Surf. Sci. 155 (1985) 639.
[117] Y. Ishikawa, M.-S. Liao, C.R. Cabrera, Surf. Sci. 463 (2000) 66.
[118] S. Kandoi, J. Greeley, M.A. Sanchez-Castillo, S.T. Evans, A.A. Gokhale, J.A. Dumesic, M. Mavrikakis, Top. Catal. 37 (2006) 17.
[119] S.K. Desai, M. Neurock, K. Kourtakis, J. Phys. Chem. 106 (2002) 2559.
[120] J. Narayanasamy, A.B. Anderson, J. Elect. Chem. 504 (2003) 35.
[121] O. Deutschmann, R. Schmidt, F. Behrendt, J. Warnatz, Proc. Combust. Inst. (1996) 1747.
[122] C.T. Campbell, G. Ertl, H. Kuipers, J. Segner, Surf. Sci. 107 (1981) 220.
[123] T. Jacob, R.P. Muller, W.A. Goddard III, J. Phys. Chem. B 107 (2003) 9465.
[124] A.C. Luntz, J. Grimblot, D.E. Fowler, Phys. Rev. B 39 (1989) 39.
[125] A. Michaelides, P. Hu, J. Chem. Phys. 114 (2001) 513.
[126] A. Michaelides, P. Hu, J. Chem. Phys. 114 (2001) 5792.
[127] J. Greeley, M. Mavrikakis, J. Am. Chem. Soc. 126 (2004) 3910.
[128] A. Gil, A. Clotet, J.M. Ricart, G. Kresse, M. Garcia-Hernandez, N. Rosch, P. Sautet, Surf. Sci. 530 (2003) 71.
[129] S. Kandoi, A.A. Gokhale, L.C. Grabow, J.A. Dumesic, M. Mavrikakis, Catal. Lett. 93 (2004) 93.
[130] X.-Q. Gong, P. Hu, R. Raval, J. Chem. Phys. 119 (2003) 6324.
[131] S.K. Desai, M. Neurock, K. Kourtakis, J. Phys. Chem. B 106 (2002) 2559.
[132] D.L. Trimm, Catal. Today 37 (1997) 233.
[133] J.R. Rostrup-Nielsen, Catal. Today 37 (1997) 225.
[134] T.E. McMinn, F.C. Moates, J.T. Richardson, Appl. Catal. B 31 (2001) 93.
[135] A.T. Anghel, S.J. Jenkins, D.J. Wales, D.A. King, J. Phys. Chem. B 110 (2006) 4147.